

A Strontium Atom Interferometer For Advanced Large Momentum Transfer

By

Sam Hedges

A thesis submitted to the
University of Birmingham
for the degree of
DOCTOR OF PHILOSOPHY

Quantum Sensing Group
School of Physics and Astronomy
College of Engineering and Physical Sciences
University of Birmingham
September 2023

UNIVERSITY OF
BIRMINGHAM

University of Birmingham Research Archive

e-theses repository

This unpublished thesis/dissertation is copyright of the author and/or third parties. The intellectual property rights of the author or third parties in respect of this work are as defined by The Copyright Designs and Patents Act 1988 or as modified by any successor legislation.

Any use made of information contained in this thesis/dissertation must be in accordance with that legislation and must be properly acknowledged. Further distribution or reproduction in any format is prohibited without the permission of the copyright holder.

Abstract

Optical atomic clock atoms are finding applications in atomic physics beyond frequency standards. A new generation of atom interferometers based on the alkaline-Earth species strontium promises unrivalled sensitivity for fundamental physics searches. In this thesis, a new strontium atom interferometry experiment is developed and demonstrated. Strontium-88 atoms are cooled using a 2D magneto-optical trap followed by a two-stage cooling process. Samples of 8×10^6 atoms are prepared in this way and used to perform Mach-Zehnder configuration atom interferometry sequences on the intercombination transition. A laser system is presented, capable of generating 30 ns pulses in alternating directions at a repetition rate of 30 MHz. The experiment will be used as a test bed to develop techniques for enhancing contrast for large momentum transfer to achieve state-of-the-art sensitivity. Such techniques will feed into the Atom Interferometry Observatory and Network (AION) collaboration and have wider-reaching implications in the field of quantum technology.

"Speak what you think now in hard words, and to-morrow speak what to-morrow thinks in hard words again, though it contradict every thing you said to-day."

– Ralph Waldo Emerson

Contents

1 Introduction **1**

1.1 Atom interferometry and its applications 1

1.1.1 Gravitational wave astronomy 4

1.1.2 Sensitivity enhancement 5

1.1.3 Single-photon atom interferometry 7

1.2 AION: Atom Interferometer Observatory and Network 10

1.3 Research overview 12

1.3.1 Thesis overview 15

1.3.2 Publications 16

2 Theory **18**

2.1 Atom interferometry 19

2.1.1 Atom-light interaction 19

2.1.2 Single-photon atom interferometry 23

2.1.3 Phase shift 26

2.1.4 Sensitivity 30

2.1.5 Large momentum transfer 31

2.1.6 Gradiometry 34

2.1.7 Contrast and fidelity . . . 36
2.1.8 Velocity selection . . . 38
2.1.9 Atom interferometry in AION . . . 41
2.2 Strontium . . . 42
2.2.1 Level structure . . . 43
2.2.2 Cooling and trapping strontium . . . 45
2.2.3 Strontium in atom interferometry . . . 49

3 Experiment **52**
3.1 Vacuum system . . . 55
3.1.1 Free-fall region . . . 56
3.1.2 Atomic beam . . . 59
3.1.3 Optical access . . . 62
3.1.4 Vacuum pumping and performance . . . 64
3.2 Magnetic fields . . . 65
3.2.1 Chamber One . . . 65
3.2.2 Chamber Two . . . 67
3.3 Cooling laser system . . . 69
3.3.1 First-stage cooling . . . 70
3.3.2 Second-stage cooling . . . 73
3.3.3 Optical delivery . . . 76
3.4 Frequency stabilisation . . . 78
3.4.1 Reference cavity . . . 81
3.4.2 Locking scheme . . . 82
3.5 Detection . . . 84

3.5.1 Camera imaging . . . 85
3.5.2 Detection sequence . . . 86
3.5.3 Photodiode . . . 89
3.6 Timing, control and data acquisition . . . 90
3.6.1 ARTIQ . . . 90
3.6.2 ndscan . . . 91

4 Laser systems for strontium atom interferometry 92
4.1 Pulse shaping . . . 96
4.1.1 Techniques for pulse shaping . . . 97
4.1.2 Implementation . . . 98
4.1.3 Performance . . . 102
4.2 Atom interferometry laser . . . 104
4.2.1 Design . . . 105
4.2.2 Performance . . . 107
4.2.3 Alignment . . . 110
4.3 Pulses for long-baseline atom interferometry . . . 111
4.4 Summary . . . 114

5 Strontium atom interferometry 116
5.1 Cold atoms . . . 116
5.1.1 Blue MOT . . . 117
5.1.2 Red MOT . . . 118
5.1.3 Magnetic trap . . . 124
5.2 Detection . . . 126
5.3 Atom optics . . . 129

5.3.1 Rabi scan 129
5.4 Atom interferometry 133
5.4.1 Initial atom interferometry 133
5.5 Summary 134

6 Conclusion **136**

Chapter 1

Introduction

1.1 Atom interferometry and its applications

Atom interferometry [1], the wave-particle duality-analogue to optical interferometry, was first demonstrated in 1991 [2]. Several different atom interferometry implementations have been realised [3–5] but this thesis concerns itself with the most prevalent approach, light-pulse atom interferometry (LPAI) [6]. LPAI employs precisely timed light pulses that place atomic wave packets into quantum superposition states, which are later recombined, producing interference. These states travel distinct paths, accruing a relative phase shift that offers information about the fields in which they evolved. One can consider the atoms as perfect test masses and the laser light a precise ruler against which their position is measured. Rotation [7], accelerations [8] and gravity [9] can all be measured in this way.

Perhaps the simplest of light-pulse atom interferometry geometries is the so-called Mach-Zehnder (MZ), or Kasevich-Chu geometry [2], illustrated in figure 1.1. The atom interferometer is analogous to its classical counterpart, the MZ inter-

ferometer, but with the roles of light and matter interchanged. In atom (optical) interferometry, precisely timed light pulses (beam splitters and mirrors) are used to split, redirect and recombine coherent matter waves (light). The atomic wave packet is split spatially along two paths, by the momentum kicks which the light pulses impart. The relative phase between the two paths can be measured through the atom state populations (intensity fringe) on the output ports.

The interfered matter wave is a cloud of a million or so laser-cooled neutral atoms, which act as perfect, independent test particles. Atoms are prepared in a single atomic state, and the MZ-configuration sequence begins with an initial resonant light pulse. This pulse interacts with each atom, splitting its wave function into two superposition states of energy and momentum with 50% probability. The two states travel apart on distinct paths as a result of the photon momentum imparted to one. The atoms are allowed to evolve until, at time T, a second pulse is applied. This pulse interacts with both states of the atom with 100% probability, inverting the population of the two states and giving the wave packets a kick towards one another. After another time T, the wave functions are spatially overlapped, and a final pulse closes the interferometer. The first, second and third pulses can be likened to the first beam splitter, mirror and final beam splitter of a classical interferometer, respectively. At the close of the interferometer, the phase is inferred from the relative population of the two states.

Since its first demonstration in 1991, atom interferometry has become a burgeoning field with experiments around the world targeting both explorations of fundamental physics as well as applied use cases. Lab-based atom interferometers have been used to measure the Newtonian gravitational constant [10] and the fine structure constant [11], as well as to test the equivalence principle [12] and grav-

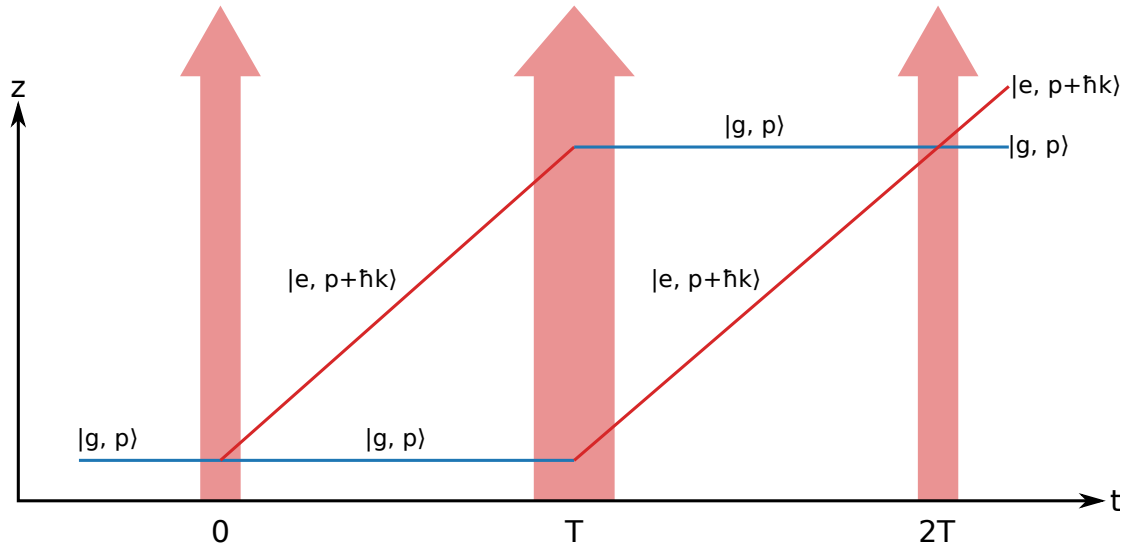


Figure 1.1: Space-time diagram for a three-pulse atom interferometer with Mach-Zehnder geometry. Blue lines represent the ground state of the atom, $|g, p\rangle$, whereas red lines represent the excited state of the atom, $|e, p + \hbar\mathbf{k}\rangle$ having additional momentum $\hbar\mathbf{k}$, where $\mathbf{k}$ is the wave vector of the interacting light. Red arrows show the direction and timing of the atom optics light pulses. An initial pulse at $T = 0$ splits the wavefunction of the atoms, giving a kick to the excited state wave packet in the positive z direction. After time T, a second pulse of twice the duration of the first redirects the two paths towards one another. At time $2T$ the wave packets are spatially overlapped and a third pulse closes the interferometer.

itational Aharonov-Bohm effect [13]. Meanwhile, much effort has been focused on making these instruments portable. Atom interferometers have been deployed, for example, at sea [14], in the air [15, 16], in civil engineering applications [17] and in remote locations [18], for a host of applications [19, 20]. The past five years have also seen the emergence of commercial quantum sensors based on atom interferometry [18, 21].

1.1.1 Gravitational wave astronomy

The first direct detection of a gravitational wave in 2015 marked one of the most significant discoveries in physics in recent history [22]. Atom interferometry has also been proposed as a promising technique for gravitational wave detection [23, 24]. Indeed such atom interferometers stand to complement current gravitational wave detectors by operating in a frequency band where LIGO and VIRGO are relatively insensitive [25].

To measure gravitational waves using atom interferometry, two atom interferometers are separated along an axis by some baseline distance and are interrogated by common light pulses. This configuration is known as a gradiometer. Gravitational wave-induced phase shifts on the light, as it propagates across the gradiometer baseline, are read out in the phase difference between the two interferometers.

Atom interferometry-based gravitational wave detectors have the potential to extend this new realm of astronomy into a largely unexplored frequency band, known as the mid-band [25–28]. This band approximately spans 0.01 Hz to 1 Hz, a band of relative insensitivity for LIGO, VIRGO and LISA experiments. This could open gravitational wave astronomy to sources such as intermediate-mass black hole

mergers and neutron star binaries [25]. Moreover, an atom interferometry based detector in this region could provide predictive information about events for the aforementioned experiments, and vice versa. Measuring gravitational waves using atom interferometry, however, will require sensitivity beyond the current state-of-the-art and baselines much longer than those of existing experiments [25].

1.1.2 Sensitivity enhancement

The phase sensitivity of an atom interferometer is proportional to the space-time area enclosed by the two paths and $\sqrt{N}$, where N is the number of participating atoms. In figure 1.1, the space-time area is the area enclosed by the parallelogram, and can be enhanced by either increasing T, the time between pulses, or by increasing the momentum separation between the two paths.

Sensitivity can therefore be improved through several different approaches. To increase T, some experiments utilise a long vertical drop distance in an atomic fountain [29, 30] whereas others have been designed such that the whole experiment may be dropped [31], or launched on a sounding rocket [32]. Increasing T beyond a certain point becomes impractical as a result of the free-fall distances required but also because of the finite temperature expansion of the atom cloud. The spatial extent of the atom ensemble can lead to a loss of fidelity and sensitivity, as atoms sample varying light intensities or are lost radially from the laser beams. An alternative to long drop distances has been demonstrated wherein atoms are loaded into lattice sites after the opening of the interferometer and held for up to a minute [33, 34]. This solves the free-fall distance and cloud expansion issues associated with long T times but places stringent constraints on the lattice laser,

whose intensity must be well controlled to avoid systematic effects. Arbitrarily increasing atom number N is not practical due to the dynamics of the way atoms are trapped [35]. Moreover, there is typically a trade-off between atom number and temperature, and a colder ensemble temperature is desirable to minimise the effects of Doppler dispersion. It is also possible to surpass the atom shot noise limit, or standard quantum limit, by using a technique known as spin-squeezing [36, 37]. Entanglement-enhanced phase noise is an active area of research and has already been demonstrated in the context of atom interferometry [38–42].

One approach with the potential to afford the greatest increases in sensitivity is large momentum transfer (LMT). This technique increases the momentum with which the atom interferometer paths move apart in space-time, and is inherently more scalable than increasing T or N. The augmentation of the interferometer sequence in large momentum transfer is typically achieved either by applying additional sequential pulses or by employing pulses that couple the atoms into higher-order momentum states. The first demonstration of large momentum transfer relied on Bragg scattering to achieve a momentum separation of 6 $\hbar k$ [43]. The Bragg method uses near-resonant standing waves of light, which interact with the atomic wave packets, causing them to scatter into different momentum state orders. Careful control of the intensity of light, detuning from resonance and interaction duration, sets the proportion of atoms scattering into a given order. This makes it possible to construct the beam splitter and mirror atom optics required for an atom interferometry sequence. More significant momentum separations have been realised through the application of sequential Bragg pulses. Wave packet separations on the half-metre scale, and momentum splittings of up to 200 $\hbar k$ have been achieved in this way [29, 44–46]. The extent to which this technique

can be scaled is somewhat limited since a large detuning is required to minimise single-photon losses, but this, in turn, requires a high laser intensity. Efficient pulse transfer also requires a very narrow velocity class of atoms [47]. For high momentum orders or multiple pulses, these constraints can become prohibitive. An alternative approach uses Bloch oscillations, or accelerating optical lattices [48, 49]. This avoids the power scaling issues associated with sequential Bragg pulses, enabling large momentum transfer of up to 600 $\hbar k$ [50–53]. The approach is, however, susceptible to phase noise introduced by the lattice potential.

Some of the LMT papers discussed demonstrate impressive momentum separations of up to several 100 $\hbar$k but without fringe visibility at the close of the interferometer. One of the greatest technical challenges in furthering the limits of sensitivity and LMT will be in pushing the contrast, requiring novel techniques and approaches.

1.1.3 Single-photon atom interferometry

Until recently, atom interferometers have typically operated using two-photon Raman or Bragg transitions in elements such as rubidium or caesium. This section will show why two-photon counter-propagating transitions are unsuitable for long-baseline atom interferometry. First demonstrated in strontium, the advent of single-photon atom interferometry has opened up new possibilities within the field [54, 55], and particularly in large momentum transfer [56, 57].

Strontium is proving to be an element of great interest in the wider atomic physics community as a result of its exceptionally narrow linewidth clock transition. It has become the most widely used atom in the field of optical atomic

clocks, enabling fractional uncertainties in the low 10^{-18}, an error of less than a second in ten billion years [58]. The stability and uncertainty achieved by atomic clocks using strontium have made it a strong contender for the redefinition of the SI second [59]. Widespread interest in this area of research has greatly furthered the knowledge, techniques and technologies related to strontium cold atoms experiments.

Atom interferometry with strontium was first achieved utilising the 461 nm $^1S_0 - {}^1P_1$ transition, initially using Bragg pulses, and then Bragg pulses combined with Bloch oscillations [60, 61]. Single-photon interferometry was subsequently demonstrated using the 698 mn $^1S_0 - {}^3P_0$ clock transition [54]. The more strongly coupled $^1S_0 - {}^3P_1$ intercombination transition was used to demonstrate a Bragg scheme with improved contrast compared to the preceding $^1S_0 - {}^1P_1$ transition work [62]. More recently, the intercombination line has enabled the realisation of single-photon large momentum transfer. In single-photon LMT, successive π-pulses from alternating directions impart additional momentum kicks to the interferometer arms via absorption and stimulated emission. In this way, momentum separations of 445 $\hbar k$ have been achieved and 141 $\hbar k$ before that [56, 57].

Single-photon transitions have an advantage compared to two-photon counter-propagating transitions in the context of long-baseline experiments such as the gravitational wave proposals listed previously. To illustrate this advantage, consider two atom interferometers in a gradiometer configuration, that is, separated by a baseline but interrogated by the same lasers, as in figure 1.2. In the case of two-photon counterpropagating Raman transitions, light propagating from both sides of the baseline must overlap at the position of the atoms to drive atom optics pulses. With reference to figure 1.2, a so-called control laser (solid black lines)

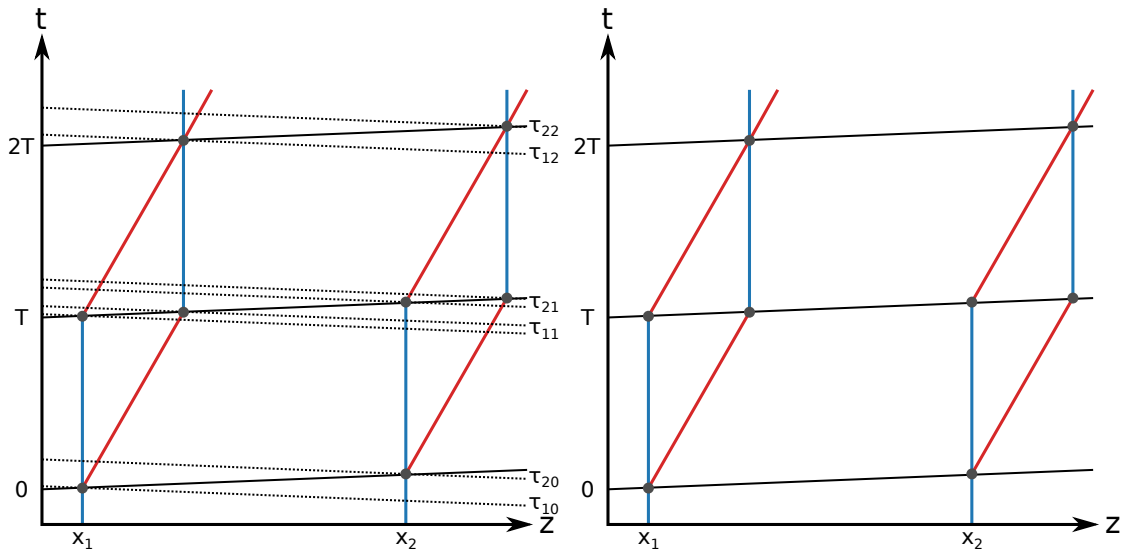


Figure 1.2: Space-time diagrams for atom interferometers in gradiometer configuration, separated by some long baseline $L = x_2 - x_1$. The gradiometer in the left hand diagram uses two-photon, counterpropagating Raman transitions where light from both lasers must overlap at the position of the atoms to drive a transition. In the right hand diagram, single-photon transitions drive the gradiometer. Blue and red lines denote the ground or excited state of the atoms, respectively. The solid black lines indicate a light pulse travelling from left to right, and the dashed black lines indicate light travelling from right to left. The light takes time $\tau_{2n} - \tau_{1n}$ to propagate across the baseline. Grey dots indicate the interaction points between light and atoms. The space-time area of each interferometer is exaggerated for clarity. The space and time axes are switched compared to the other space-time atom interferometer diagrams appearing in this thesis. Adapted from [63].

propagates from left to right and pulses to control the atom optics interactions. A passive laser (dashed black lines) propagates from right to left and runs continuously. When the baseline, or distance between atom interferometers, L is large, the propagation time $\Delta T = L/c$ for a given pulse to travel the baseline becomes consequential. A single pulse from the control laser interacts with both interferometers, but the light from the passive laser, which interacts with the two interferometers, is emitted at a different time by an amount $\tau_{2n} - \tau_{1n} = \Delta T$. Laser phase noise on this timescale will couple into the interferometer phase readout, and for increasing baselines, this becomes the dominant error source [63]. In the single-photon case, however, a single pulse drives interactions in both interferometers. This means the phase of the light is the same for both interferometers, less the propagation phase. Laser phase noise between pulses cancels as common mode by virtue of the differential measurement, mitigating the long baseline issue [63].

1.2 AION: Atom Interferometer Observatory and Network

The research presented in this thesis forms part of the AION project. AION is a UK-based initiative and consortium aiming to measure gravitational waves and test physics beyond the standard model using atom interferometry [25]. The project roadmap details a series of atom interferometers of increasing baseline, starting at 10 m, then 100 m and 1 km terrestrial experiments, followed by a satellite-based experiment with a baseline of many km.

To meet the science goals of the proposed stages of AION, all aspects of the

atom interferometer will have to be optimised. In addition to the high-fidelity LMT specifications, an atom interferometer capable of measuring gravitational waves will require a high flux of ultracold atoms, advanced cooling techniques, long baselines, long T times and detection noise below the standard quantum limit. There are seven member institutions within AION, each responsible for different aspects of the project:

- **University of Birmingham*:** Strategies and techniques in order to push large momentum transfer beyond the state-of-the-art.
- **University of Cambridge*:** High-flux atom source capable of generating, transporting and launching ultracold atoms.
- **Imperial College*:** Laser stabilisation and metrologically useful entanglement for atom interferometry.
- **King's College London:** Modelling of projected scientifically interesting signals.
- **University of Liverpool:** Phase shear detection and associated optics.
- **University of Oxford*:** Site of the initial AION-10 detector.
- **Rutherford Appleton Laboratory and Daresbury Laboratory*:** Design and construction of the sidearms and design of future longer baseline AION experiments.

Institutions with an asterisk are commissioning local strontium experiments, termed 'sidearms', in the initial phase of AION. Technologies and techniques will

be developed locally within these five institutions, and wider collaboration. These efforts will be combined in creating an initial 10 m baseline gradiometer, AION-10, to be located at the University of Oxford, with engineering design work currently underway. Feasibility studies have also begun into potential sites for AION-100 and AION-1000. The AION project has many synergies with MAGIS in the United States [26], and networked operation between AION-100 and MAGIS-100 has been proposed. Engineering work is already being carried out in preparation for the 100 m detector, which will be located at Fermilab.

To reach the proposed sensitivity targets for the later phases of the AION and MAGIS experiments, the required LMT is of the order 10^4 $\hbar k$ momentum separation [25, 26]. This is two orders of magnitude greater than the current state-of-the-art [57]. Scaling LMT to this level will be very challenging experimentally, and loss of contrast is one of the predominant limitations. Existing research into optimised pulse schemes for contrast has focused on atom interferometry using two-photon Raman transitions and often requires effective pulse durations of several times that of a generic π-pulse [64–68]. Developing strategies suitable for single-photon transitions is an emerging research area [57, 69]. Phase noise and systematic effects are also generally compounded for an increasing number of pulses. Efforts must therefore be made to minimise wavefront aberrations, AC stark and Zeeman shifts, pointing instability, Coriolis effect and more [12, 26, 70, 71].

1.3 Research overview

The purpose of the work presented in this thesis is to realise a test bed strontium atom interferometer. The experiment will be used to enable high-fidelity pulses in

large momentum transfer demonstrations beyond the current state-of-the-art. To this end, a strontium cold atoms lab is designed and realised as part of the AION collaboration. Initial work focuses on performing atom interferometry with the intercombination line in ^{88}Sr. Future work will extend to measurements using the clock transition with ^{87}Sr atoms.

Towards these goals, in this thesis, a laser system is designed and constructed for the two-stage cooling of strontium from a thermal atomic beam. The design of an ultra-high vacuum system is informed by specifications to enable future record-beating momentum separations in atom interferometry. This vacuum system is installed, and the pressure in the science region of the main chamber is inferred to be in the low 10^{-10} mbar, more than adequate for the planned stages of the experiment. Atom numbers of 2×10^7 atoms are produced by the first-stage cooling process wherein a 2D magneto-optical trap (MOT) cools the thermal atomic beam and loads a 3D MOT. A Ti:Sapph laser at 689 nm, used in second-stage cooling and atom interferometry, is locked to a high-finesse optical cavity in order to meet the performance requirements of the experiment. Through beat note measurements, the short-term linewidth of this laser is found to be better than 100 Hz. The performance of the laser is further validated in the generation of red MOT samples of 8×10^6 atoms at a temperature of 30 μK. Experiment control is performed using ARTIQ, an open-source timing system for quantum experiments. The system as a whole is demonstrated in attaining Mach-Zehnnder atom interferometry fringes, addressing the intercombination line with ^{88}Sr atoms. Pulse shaping is shown to produce 30 ns pulses at a repetition rate of 30 MHz from continuous-wave Ti:Sapph light, and the design allows for efficient and dynamic optical power allocation between laser cooling and atom interferometry.

In future, the system will be used to develop and test techniques and pulse schemes to reduce systematic effects and improve fidelity and contrast in order to achieve beyond state-of-the-art large momentum transfer. Polychromatic and composite pulse schemes will be developed and tested to improve pulse fidelity [72]. Techniques for active wavefront correction using Shack-Hartmann sensors and deformable mirrors to reduce systematic phase shifts will be required [70, 73–75]. Hybrid pulse schemes can be implemented using both the clock and intercombination transitions in strontium in the same sequence. Resonant mode geometries can be trialled, proposed in the literature for increasing sensitivity at target frequencies [76].

Proposed atom interferometry based gravitational wave detectors will use these techniques, achieving unparalleled sensitivities to mid-band gravitational waves. The AION experiment also aims to probe the parameter space of ultra-light dark matter and test physics beyond the standard model [25]. Whilst the LMT and techniques presented here target fundamental physics searches, practical applications also stand to benefit from the enhanced sensitivity afforded. Large momentum transfer could, in principle, be implemented in a new generation of more compact sensors with improved sensitivity or measurement rate, lending itself to applications requiring portability. Techniques for improving the contrast and fidelity of atom interferometers will have a wide-reaching impact beyond strontium single-photon atom interferometry.

1.3.1 Thesis overview

The overall structure of this thesis is as follows: Chapter 2 presents the theory underpinning the operation of an atom interferometer, beginning with the atom-light interaction and the pulses that form the building blocks of atom interferometry sequences. The atom interferometer phase shift from accelerations is derived, and so too is the sensitivity at the atom shot noise limit, before showing how sensitivity can be scaled through large momentum transfer. Gradiometry, the differential measurement technique, is introduced, as well as the concept of contrast and fidelity, and the importance of cold sample temperatures in velocity selection. The section on atom interferometry concludes with a high-level overview of how atom interferometry serves the physics goals of AION. The second part of Chapter 2 introduces the level structure of strontium, highlighting the features that make the element interesting from the point of view of cold atoms, and especially atom interferometry experiments.

The experimental setup is detailed in Chapter 3. Simulations are presented, which inform the geometry of the vacuum system for LMT atom interferometry, where the dynamics can be very different to normal geometries dominated by free fall. Characterisation of the magnetic field gradients for the 2D MOT and 3D MOT regions are given. The design of the laser system for both the first-stage and second-stage cooling is presented, as well as the design of the reference optical cavity setup. The chapter concludes by discussing the detection scheme and setup and then the ARTIQ timing system.

In Chapter 4, the design and characterisation of the atom interferometry laser is given. Pulse shaping of 30 ns pulses at a repetition rate of 30 MHz is demonstrated,

towards future large momentum transfer goals. A proposal is discussed for a future long baseline atom interferometer, addressing the challenging optical powers required in future large momentum transfer on the clock transition in strontium.

Chapter 5 presents the commissioning of the strontium experiment. The parameters in the two-stage cooling sequence are optimised, and the vacuum pressure is verified through magnetic trap lifetime measurements. The first atom interferometry fringes are presented, validating the performance of the experiment subsystems and laying the foundations for future development.

Concluding remarks are given in Chapter 6, summarising the work in this thesis and looking ahead to the future of the project.

All figures, data and simulations presented in this thesis are the author's own unless otherwise stated.

1.3.2 Publications

The author co-authored the following publications in the pursuit of the research presented in this thesis:

- B. Stray, O. Ennis, S. Hedges, S. Dey, M. Langlois, K. Bongs, S. Lellouch, M. Holynski, B. Bostwick, J. Chen, et al. Centralised design and production of the ultra-high vacuum and laser-stabilisation systems for the aion ultra-cold strontium laboratories. *arXiv preprint* arXiv:2305.20060, 2023.

- R. Nourshargh, S. Hedges, M. Langlois, K. Bongs, and M. Holynski. Doppler compensation for cavity-based atom interferometry. *Optics Express*, 30(17):30001–30011, 2022.

- R. Nourshargh, S. Lellouch, S. Hedges, M. Langlois, K. Bongs, and M. Holynski. Circulating pulse cavity enhancement as a method for extreme momentum transfer atom interferometry. *Communications Physics*, 4(1):257, 2021.

- L. Badurina, E. Bentine, D. Blas, K. Bongs, D. Bortoletto, T. Bowcock, K. Bridges, W. Bowden, O. Buchmueller, C. Burrage, et al. Aion: an atom interferometer observatory and network. *Journal of Cosmology and Astroparticle Physics*, 2020(05):011, 2020.

The following paper was also published during the author's PhD but is related to practical application rather than fundamental physics:

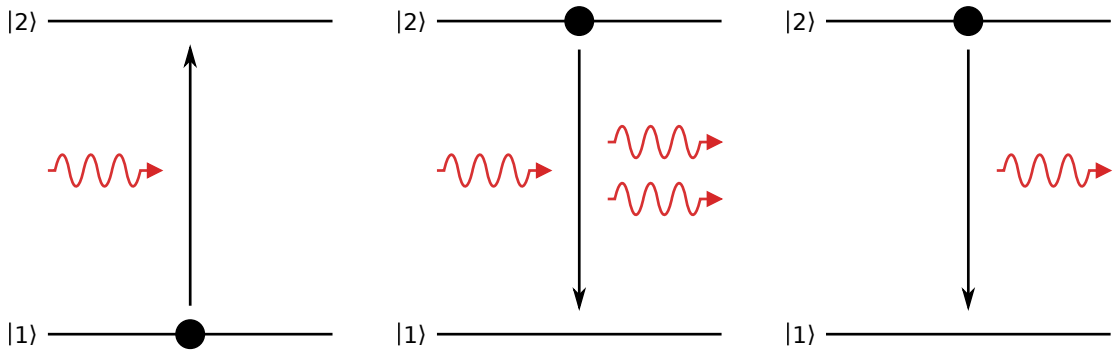
- J. Vovrosh, K. Wilkinson, S. Hedges, K. McGovern, F. Hayati, C. Carson, A. Selyem, J. Winch, B. Stray, L. Earl, et al. Magneto-optical trapping in a near-surface borehole. *PLoS ONE*, 18(7):e0288353, 2023.

Chapter 2

Theory

This chapter begins by covering the atom-light interaction and atom optics which form the basis for atom interferometry. The phase shift and sensitivity of the interferometer are derived before addressing the technique of large momentum transfer through which sensitivity can be enhanced. Gradiometry is introduced, the differential measurement in which two atom interferometers are interrogated by the same lasers. Contrast and fidelity are discussed, two important metrics in the context of large momentum transfer and maximising sensitivity.

Strontium is different in a few key ways from the alkali metals with which atom interferometry was typically performed previously. The second half of the chapter discusses the properties of strontium that make it well-suited to cold atoms experiments and atom interferometry specifically.



(a) Absorption (b) Stimulated emission (c) Spontaneous emission

Figure 2.1: The three processes by which an atom can be excited, or de-excited between two states, $|1\rangle$ and $|2\rangle$. In each figure, a red arrow on the left-hand side represents an incoming photon and on the right-hand side an outgoing photon.

2.1 Atom interferometry

2.1.1 Atom-light interaction

Fundamental to the atom interferometer is the interaction between light and atoms. An atom illuminated by light exchanges energy with the electromagnetic field via the processes of absorption and stimulated (as well as spontaneous) emission, as illustrated in figure 2.1. A two-level atom in its ground state can absorb a photon exciting the atom from ground to excited state, receiving a momentum kick $\hbar\mathbf{k}$ in the direction of the incident photon, where $\hbar$ is the reduced Planck's constant and $\mathbf{k}$ is the wave vector. Conversely, an atom in the excited state can undergo stimulated emission, interacting with a photon, which causes it to decay to the ground state. In this case, the atom emits a photon identical in direction, phase and polarisation to the one which caused it, receiving a kick $-\hbar\mathbf{k}$ satisfying conservation of momentum. For completeness, an atom in its excited state can also undergo spontaneous emission, decaying to the ground state and emitting a

photon in a random direction. This last process serves only to diminish coherence between the two states in an atom interferometer.

This section examines the light-matter interaction through the optics of quantum mechanics by solving the Schrödinger equation for a two-level atom, closely following Foot [77]. Consider a two-level atom, with wave functions Ψ_1 and Ψ_2 corresponding to the energy levels E_1 and E_2 respectively

$$\Psi_1(\mathbf{r}, t) = \psi_1(\mathbf{r}) e^{-iE_1 t/\hbar}, \tag{2.1}$$

$$\Psi_2(\mathbf{r}, t) = \psi_2(\mathbf{r}) e^{-iE_2 t/\hbar}. \tag{2.2}$$

The full wave function of the atom is the product of the individual eigenstates with their time-varying coefficients

$$\Psi(\mathbf{r}, t) = c_1 \left|1\right\rangle e^{-i\omega_1 t} + c_2 \left|2\right\rangle e^{-i\omega_2 t} \tag{2.3}$$

where $c_n = c_n(t)$ and $\omega_n = E_n/\hbar$. Since the atom must be in one of the two states, normalisation requires that $|c_1|^2 + |c_2|^2 = 1$.

The Hamiltonian of the system, $\hat{H}$, comprises two parts, $\hat{H} = \hat{H}_0 + \hat{H}_I$. The first part H_0 is the unperturbed, time-independent Hamiltonian with eigenstates $|1\rangle$ and $|2\rangle$, and eigenvalues E_1 and E_2, corresponding to the energy levels of the atom. $\hat{H}_I$ is the interaction Hamiltonian describing the mixing between the two states caused by the electromagnetic field $\hat{H}_I(t) = e\mathbf{r} \cdot \mathbf{E}_0 \cos(wt)$, where $-e\mathbf{r}\cdot$ is the dipole operator of the atom with an electron at position $\mathbf{r}$ relative to the centre of mass of the atom. $\mathbf{E} = \mathbf{E}_0 \cos(\omega t)$ is the electric field.

Now, through substituting the wave function in equation 2.3 into the time-

dependent Schrödinger equation

$$i\hbar\frac{\partial\Psi}{\partial t} = \hat{H}\Psi \tag{2.4}$$

then by multiplying on the left by $\langle 1|$ and $\langle 2|$ respectively and rewriting $\cos(\omega t)$ in exponential form using Euler's formula, one arrives at the coupled differential equations

$$i\dot{c}_1 = c_2[e^{i(\omega-\omega_0)t} + e^{-i(\omega+\omega_0)t}]\frac{\Omega}{2}, \tag{2.5}$$

$$i\dot{c}_2 = c_1[e^{i(\omega+\omega_0)t} + e^{-i(\omega-\omega_0)t}]\frac{\Omega^*}{2} \tag{2.6}$$

where $\omega_0 = \omega_2 - \omega_1$, the angular frequency of the light that couples the two states, and Ω is the Rabi frequency

$$\Omega = \frac{\langle 1|\, e\mathbf{r}\cdot\mathbf{E}_0\,|2\rangle}{\hbar} \tag{2.7}$$

which is the frequency at which the atom oscillates between the two states, in the presence of the electric field. This is a quantity of great significance in the context of atom interferometry, as will become evident.

Some approximations must be made in order to solve the Schrödinger equation. Firstly, since the wavelength of the light is very large compared to the scale of an atom, it can be assumed that the electric field has constant amplitude for the purpose of the integral in equation 2.7. Secondly, the rotating-wave approximation says that for a light field with small detuning from atomic resonance, $|\Delta| \ll \omega_0$ where $\Delta = \omega - \omega_0$, terms in equations 2.5 and 2.6 in $\omega + \omega_0$ oscillate so quickly

that they time average to zero for reasonable interaction times. Then

$$i\dot{c}_1 = c_2 e^{i(\omega-\omega_0)t}\frac{\Omega}{2}, \tag{2.8}$$

$$i\dot{c}_2 = c_1 e^{-i(\omega-\omega_0)t}\frac{\Omega^*}{2} \tag{2.9}$$

which can be combined into a second-order differential equation for c_2 whose solution is

$$P_2(t) = |c_2|^2 = \frac{\Omega^2}{\Omega^2+\Delta^2}\sin^2\left(\frac{\sqrt{\Omega^2+\Delta^2}}{2}t\right) \tag{2.10}$$

provided the atom started in state $|1\rangle$. Given the atom is initially in state $|1\rangle$ ($c_1(0) = 1$), this is the probability of observing the atom in state $|2\rangle$ after time t, $P_2(t)$. When the light is resonant with the transition $\omega = \omega_0$, $\Delta = 0$ and this reduces to

$$P_2(t) = \sin^2\left(\frac{\Omega t}{2}\right). \tag{2.11}$$

The graph in figure 2.2 demonstrates how the state $|2\rangle$ population oscillates with time for different detuning values. Efficient transfer between states requires that $\Delta \ll \Omega$. It also shows that for non-zero detunings, the frequency of oscillation increases. This frequency, $\Omega_{\text{eff}} = \sqrt{\Omega^2+\Delta^2}$, is known as the effective Rabi frequency.

Applying a resonant ($\Delta = 0$) light pulse of duration $\tau_\pi = \frac{\pi}{\Omega}$ to an atom initially in state $|1\rangle$ will transfer it to state $|2\rangle$ and vice versa. If instead a pulse of duration $\tau_{\pi/2} = \frac{\pi}{2\Omega}$ is applied, the atom is placed into a superposition of states $|1\rangle$ and $|2\rangle$ with equal probability. These pulses are known as a π-pulse and $\pi/2$-pulse, respectively. Together, they make up the so-called atom optics required for a light-pulse atom interferometer. When considering single-photon or two-photon Raman

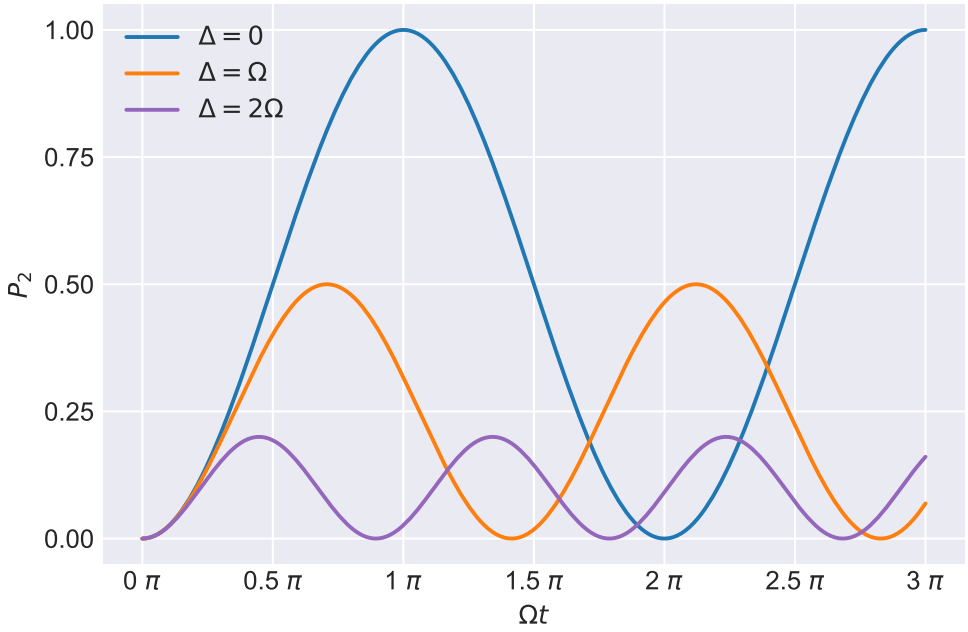


Figure 2.2: Probability of finding an atom in state $|2\rangle$ P_2 after Ωt, for an atom in a monochromatic light field of detuning Δ given the atom was initially in state $|1\rangle$ ($P_2(t = 0) = 0$).

transitions, the atom optics couple the internal and external degrees of freedom, because the processes that change the internal state also impart momentum via photon recoils.

2.1.2 Single-photon atom interferometry

To specify 'single-photon' might seem like an odd distinction at first since it is perhaps the most simple case. However, the majority of preceding work relied on two-photon transitions, predominantly Raman, which optically couple two hyperfine states via an intermediate virtual state [2, 78]. The long-lived hyperfine states allow for long coherence times, but to eliminate off-resonant coupling to nearby

excited states requires that the virtual state be sufficiently far detuned. An effective Rabi frequency describes the two-photon process, $\Omega_{\text{eff}} = \frac{\Omega_1 \Omega_2}{2\Delta}$ where $\Omega_{1,2}$ are the Rabi frequencies of the two transitions and Δ is the detuning of the virtual state [77]. Said detuning therefore limits the effective Rabi frequency, requiring longer π-times, which in turn leads to decoherence and decreased velocity acceptance, as detailed in section 2.1.8. A new generation of experiments using 'clock atoms', having optical clock transitions, has enabled the evolution of two-photon to single-photon transitions in light-pulse atom interferometers [54, 56, 57].

An atom interferometer in MZ configuration is shown in figure 2.3. An initial $\pi/2$-pulse 'beam splitter' splits the wave function of the atoms into an equal superposition of energy and momentum states $|1, p\rangle$ and $|2, p + \hbar k\rangle$. The excited state wave packet has additional momentum $hbark$ from the photon recoil and so the two wave packets move apart spatially for a time T. Next, a π-pulse or 'mirror' imparts a photon-recoil kick to both wave packets, redirecting them towards one another and inverting the state populations. The momentum kicks for the two wave packets are in opposing directions since the excited state wave packet undergoes stimulated emission whereas the ground state wave packet receives momentum from photon absorption. After a further time T has elapsed, the wave packets are overlapped spatially, and a final $\pi/2$-pulse completes the sequence. The difference in phase accrued by the two arms is then inferred at the output through the relative populations of the two states, as shown later. In the case where the atoms are accelerating, the first-order phase shift comes from the changing position of the atoms relative to the laser.

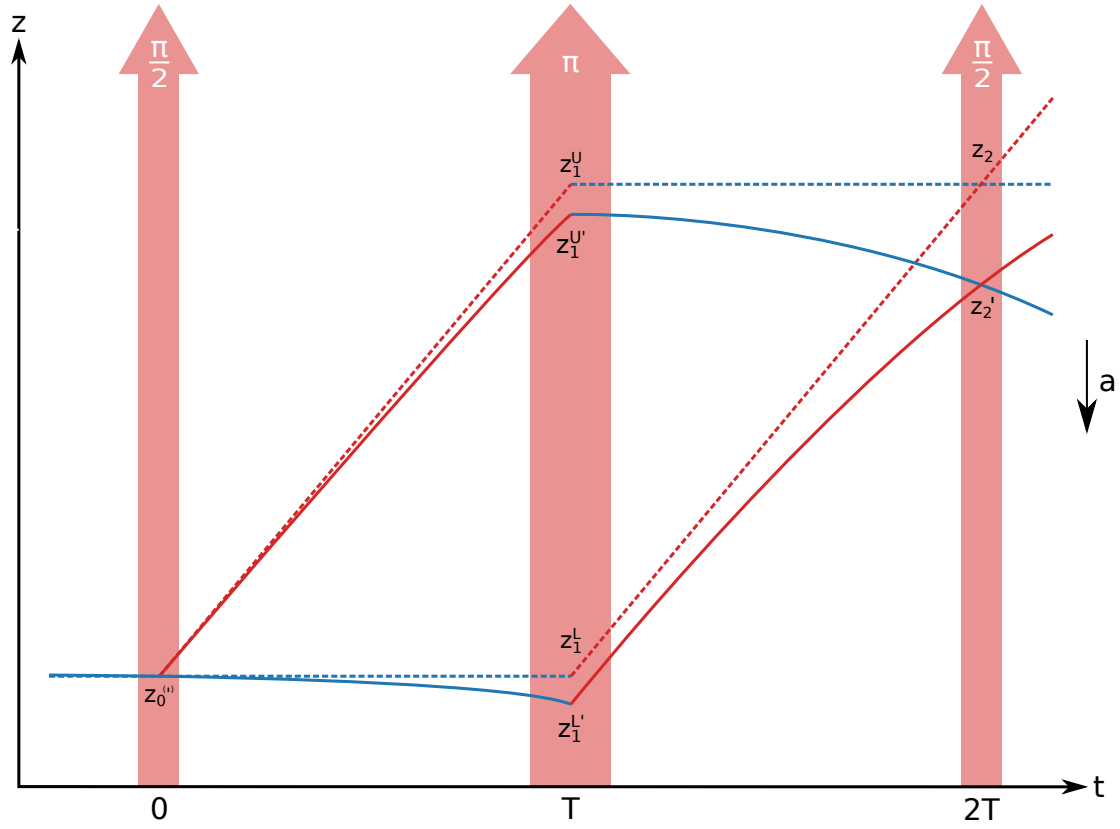


Figure 2.3: Space-time diagram of the Mach-Zehnder atom interferometer sequence. The blue and red lines show the trajectory of the two paths for an atom in state $|1\rangle$ and $|2\rangle$, respectively. The dashed lines show the trajectory in the initial reference frame of the atoms, with positions denoted by un-primed z_t. z_1^U and z_1^L give the position of the atom at time T for the upper and lower path respectively. The solid line shows the trajectory of the atom due to some acceleration a, in the $-z$ direction in the lab frame. These positions, denoted with a prime z_t', are related to their position in the rest frame by $z_t' = z_t - at^2/2$. Red arrows show the times and directions of the light pulses, with exaggerated pulse widths for illustration purposes.

2.1.3 Phase shift

This section aims to provide an intuition for the sources of phase shifts in the interferometer as well as a derivation of the first-order phase shift arising from the acceleration of the atoms. The subsequent discussion is based on the comprehensive treatment of the phase shift in the literature [6, 79, 80].

The interferometer phase can be separated into three distinct parts

$$\Phi = \Delta\phi_{laser} + \Delta\phi_{propagation} + \Delta\phi_{separation}. \tag{2.12}$$

The propagation phase $\Delta\phi_{propagation}$ arises from the quantum propagator, which gives the amplitude for a particle to travel from one point in space-time to another. This phase is a function of the classical action along the segments of both arms of the interferometer but also accounts for the internal energy of the atom. The contribution due to the internal evolution of the wave function is however zero provided that the energy levels are not subject to temporally-varying perturbations. Whenever the paths of the interferometer form a closed loop, it can be shown that $\Delta\phi_{propagation} = 0$ [6, 79].

It is not necessarily the case that the wave functions will overlap at the close of the interferometer. Gravity gradients, for example, can introduce an asymmetry and hence position offset. This leads to the phase shift term $\Delta\phi_{separation}$.

The final contribution to the interferometer phase in equation 2.12 is the term arising from the laser interactions

$$\Delta\phi_{laser} = \left(\sum_n \pm\phi_L(t_n, \mathbf{z}(t_n))\right)_U - \left(\sum_n \pm\phi_L(t_n, \mathbf{z}(t_n))\right)_L \tag{2.13}$$

which sums over the laser phase contributions ϕ_L at each of the interaction points. t_n is the time at which a given pulse occurs and $z(t_n)$ is the corresponding position, relative to the position at $t = 0$. U and L denote the upper and lower paths, respectively. The sign of each contribution $\pm\phi_L$ is positive when the atom absorbs a photon and negative in the case of stimulated emission. Since the separation term is generally small compared to the laser term, the contribution $\Delta\phi_{separation}$ can also be assumed to be zero, with the interferometer phase coming exclusively from the laser term $\Delta\phi_{laser}$.

So, what is the phase shift from the interferometry sequence? The phase difference between the two paths is independent of the output port, as required by the conservation of probability. To calculate it, one can just consider the contributions from the paths of atoms ending up in state $|2\rangle$ after the final $\pi/2$-pulse:

$$|1\rangle \rightarrow |2\rangle \rightarrow |1\rangle \rightarrow |2\rangle\,, \tag{2.14}$$

$$|1\rangle \rightarrow |1\rangle \rightarrow |2\rangle \rightarrow |2\rangle \tag{2.15}$$

corresponding to the upper and lower paths, respectively. The phase of each interaction with the light is given by

$$\phi_L(t_n, \mathbf{z}(t_n)) = \mathbf{k} \cdot \mathbf{z}(t_n) - \omega t_n - \phi_n \tag{2.16}$$

where the wave vector $k = 2\pi/\lambda$ and ω is the angular frequency of the light. ϕ_0 is the initial phase of the light and ϕ_n of subsequent pulses describes any additional offset relative to ϕ_0. If the atoms are in free fall with some acceleration $\mathbf{a}$, where $\mathbf{a} \cdot \hat{\mathbf{z}} = |a|$, then their positions are related to their position in the rest frame by

$z(t)' = z(t) - at^2/2$. Figure 2.3 illustrates the three-pulse sequence in the lab frame and the rest frame of the atoms.

The phase shift imparted to the upper path has three terms owing to the three atom-light interaction points

$$\Delta\phi^U_{laser} = [kz'_0 - \phi_0] - [kz_1^{U\prime} - \omega T - \phi_1] + [kz'_2 - 2\omega T - \phi_2] \tag{2.17}$$

$$= [kz_0 - \phi_0] - [k\left(z_1^U - \frac{1}{2}aT^2\right) - \omega T - \phi_1] + [k(z_2 - 2T^2) - 2\omega T - \phi_2] \tag{2.18}$$

$$= k\left(z_0 - z_1^U + z_2 - \frac{3}{2}aT^2\right) - \omega T - \phi_0 + \phi_1 - \phi_2. \tag{2.19}$$

The lower path only interacts with the π-pulse and so the phase shift is given by

$$\Delta\phi^L_{laser} = kz_1^{L\prime} - \omega T - \phi_1 \tag{2.20}$$

$$= k\left(z_1^L - \frac{1}{2}aT^2\right) - \omega T - \phi_1. \tag{2.21}$$

The relative phase shift of the two paths due to the laser, and thus the overall interferometer phase, is then the difference between equation 2.19 and 2.21

$$\Phi = \Delta\phi_{laser} = \Delta\phi^L_{laser} - \Delta\phi^U_{laser} \tag{2.22}$$

$$= k\left[z_1^L - (z_0 - z_1^U + z_2) + aT^2\right] + \phi_0 - 2\phi_1 + \phi_2 \tag{2.23}$$

$$= kaT^2 + \phi_0 - 2\phi_1 + \phi_2 \tag{2.24}$$

where the position terms cancelled since $z_1^L = z_0$ and $z_1^U = z_2$ as is clear from inspection of figure 2.3. In the absence of applied phase shifts between pulses, and

neglecting phase noise, $\phi_2 = \phi_1 = \phi_0$, so these terms also cancel to leave

$$\Phi = kaT^2 \tag{2.25}$$

or more generally

$$\Phi = \mathbf{k} \cdot \mathbf{a}T^2. \tag{2.26}$$

That is to say, the phase of the interferometer is a sensitive probe of acceleration in the direction of the laser beam.

The interferometer phase is not directly observable, and in practice, it is read out by measuring the ratio of atoms in the two states, $|1\rangle$ and $|2\rangle$,

$$P_2 = \frac{N_2}{N_1 + N_2} = \frac{1}{2}(1 - \cos\Phi) \tag{2.27}$$

$$= \frac{1}{2}[1 - \cos(\mathbf{k} \cdot \mathbf{a}T^2)] \tag{2.28}$$

where P_2 is the probability of observing a given atom in state $|2\rangle$ at the close of the interferometer and $N_{1,2}$ is the number of atoms in states 1 and 2 respectively. Conversely $P_1 = \frac{1}{2}(1 + \cos\Phi)$.

It is possible to map out an interference fringe by, for example, scanning the phase of the final light pulse ϕ_2 over $0 \to 2\pi$. If T and $\mathbf{a}$ are constant and provided that the frequency of the light tracks the Doppler shift of the accelerating atoms, the fringe can be fit to and a value for a extracted. Such a sensor aligned vertically will make precise measurements of gravity.

2.1.4 Sensitivity

Considering an atom interferometer with an ensemble of N uncorrelated atoms, the projection of the atoms into the two states at the output follows the binomial distribution. The probability of observing a given atom in the excited state is P_2 from equation 2.27 and the probability of measuring N_2 atoms in the excited state is $P(N_2)$. Since N is typically of order 10^5 or greater, the central limit theorem applies and says that $P(N_2)$ is well approximated by the normal distribution, with standard deviation

$$\sigma_P = \sqrt{\frac{P_2(1-P_2)}{N}}. \tag{2.29}$$

The uncertainty on the phase is then

$$\sigma_\Phi = \sigma_P \frac{d\Phi}{dP} \tag{2.30}$$

$$= \sqrt{\frac{\frac{1}{4}(1-\cos^2\Phi)}{N}} \frac{2}{\sin\Phi} \tag{2.31}$$

$$= \frac{1}{\sqrt{N}} \tag{2.32}$$

which is the atom shot noise limit [81, 82]. As a result, the per-shot phase sensitivity, and sensitivity to acceleration, of an interferometer at the atom shot noise limit is

$$\frac{\sigma_\Phi}{\Phi} = \frac{\sigma_a}{a} = \frac{1}{\mathbf{k}\cdot\mathbf{a}T^2\sqrt{N}}. \tag{2.33}$$

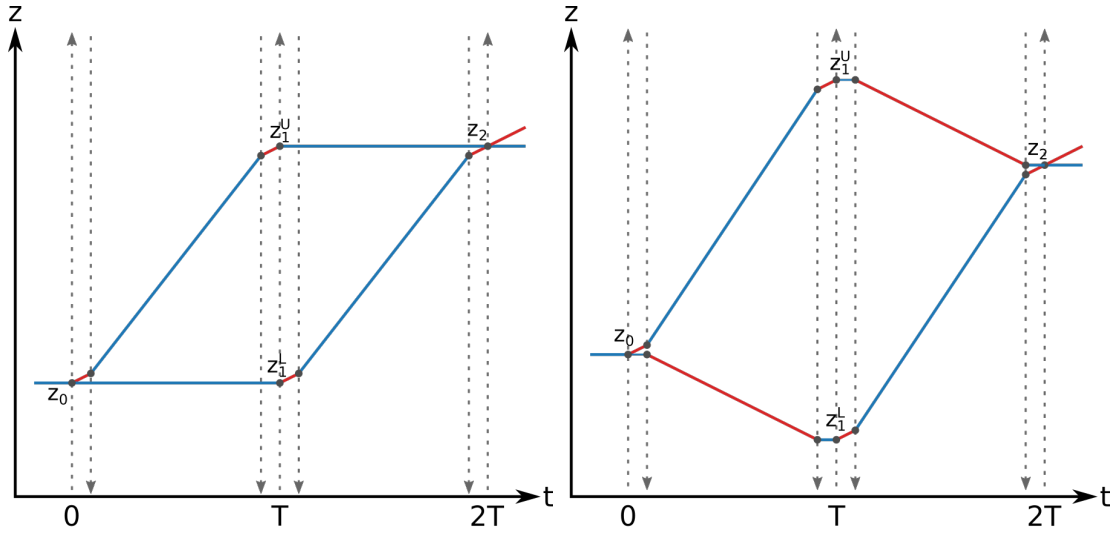
In experiments like these, one naturally asks the question "How might we improve the sensitivity?". From equation 2.33 it can be seen that the per-shot sensitivity scales with $1/\sqrt{N}$ and the space-time area enclosed by the two paths. As discussed in section 1.1, spin-squeezed detection can surpass the atom shot noise

limit, but scaling this up so that it can be used in conventional experiments is an area of ongoing research [38–42]. The dynamics of the way atoms are trapped means that it is difficult to increase the number of atoms N beyond a certain point [83], and the sensitivity scaling is weak anyway due to the square root. The squared scaling in T-time seems more promising but if the atoms are in free fall under gravity then the vertical distance required becomes challenging. It transpires that there is a third way to improve sensitivity through increasing the momentum separation between the paths of the interferometer. Large momentum transfer, the technique of increasing momentum separation, increases the sensitivity by a factor n, the number of photon recoils of momentum between paths, in $\hbar k$.

2.1.5 Large momentum transfer

Several approaches have been demonstrated for increasing the momentum separation between paths in an atom interferometer as detailed in section 1.1. The following discussion focuses on sequential single-photon large momentum transfer where following the opening pulse, sequential π-pulses are applied from alternating directions such that the momentum kicks from absorption and stimulated-emission add constructively [56, 57]. This is because if an atom receives a kick in the direction of a light pulse from absorption, a subsequent pulse from the opposite direction will increase the momentum of the atom, through stimulated emission.

After the opening of the atom interferometer, there are two velocity classes of atoms, separated in momentum by $\hbar k$. As a result, the interferometer can proceed in two distinct ways. The relative Doppler shift of the light between the two classes can cause the light to interact with only one path. Alternatively, the light



(a) 2 $\hbar k$-separation (b) 3 $\hbar k$-separation

Figure 2.4: Space-time diagrams for the two most simple single-photon LMT schemes, each comprising seven pulses. The dashed arrows denote the light pulses and direction of travel, the dots indicate the points at which the light interacts with the atoms and blue and red lines correspond to states $|1\rangle$ and $|2\rangle$ respectively. In both diagrams, all pulses are π-pulses except for the first and last pulse which are $\pi/2$ pulses. The time separating adjacent pulses is assumed to be much shorter than T. (a): In the non-degenerate case, only the middle π-pulse at time T interacts with both paths, for the other pulses the relative Doppler shift is used to selectively address either one path or the other. (b): The degenerate case. Each π-pulse addresses each path, conferring twice the momentum per π-pulse.

can interact with both paths. The difference affected in the interferometer schemes is illustrated in figure 2.4. The scheme in figure 2.4b where the pulses address both paths has an advantage in that each π-pulse causes twice the momentum splitting.

Which regime is relevant depends on the linewidth of the transition being addressed, the Rabi frequency or duration of the pulse and the order of momentum separation. In the case where only one interferometer arm is addressed, the light can be tuned to track the resonant frequency of the atoms after each recoil. In the degenerate case where the transition is driven in both arms, the frequency can be set such that the magnitude of the detuning is common for atoms in both paths. In this case, though the proportion of atoms transferred by a given π-pulse falls off with increasing momentum separation, and thus detuning, as can be seen from equation 2.10. Taken to the extreme, enough atoms will be lost cumulatively that the interferometer fringe is no longer visible at the output. Pulses from light fields of more than one frequency may make it possible to circumvent this limit though.

Following the same formalism as in section 2.1.3 one can extend the phase calculation to higher n, where n is the order of the momentum splitting in units of $\hbar k$. Making the simplifying assumption that the time between each pulse in a group of pulses $\tau \ll T$ (the propagation time between groups of pulses) such that $t_0 \approx t_1$ and so on, the phase difference at the output of the interferometer becomes

$$\Phi = nkaT^2. \tag{2.34}$$

The phase shift from the sequences in figures 2.4a and 2.4b are $2kaT^2$ and $3kaT^2$ respectively, illustrating how the additional momentum transferred in the degenerate scheme leads to increased sensitivity. Equation 2.33, the sensitivity equation,

becomes

$$\frac{\sigma_\Phi}{\Phi} = \frac{\sigma_a}{a} = \frac{1}{nkaT^2\sqrt{N}} \tag{2.35}$$

demonstrating how the sensitivity is enhanced by the additional momentum separation.

One drawback associated with large momentum transfer is that it also increases sensitivity to a variety of noise sources. In particular, laser phase noise is compounded with each additional pulse and quickly becomes the dominant source of phase noise [63, 84]. This phase noise can be mitigated via a differential measurement technique known as gradiometry.

2.1.6 Gradiometry

Atom interferometers are susceptible to laser phase noise on the timescale of T, the time between pulses. In the $\pi/2 - \pi - \pi/2$ sequence, this enters into the overall phase Φ via the ϕ_n and $kz(t)$ terms in equation 2.16. The ϕ_n term accounts for technical phase noise intrinsic to the laser whereas error from the $kz(t)$ term arises due to vibrations which cause a relative change in position between laser and atoms.

Common mode phase noise can be cancelled by using two atom interferometers separated by some baseline L, but interrogated by the same light pulses, as shown in figure 2.5. In the gradiometer approach it is the relative phase, as opposed to the absolute phase, which is measured and the common mode phase noise is cancelled in the subtraction of one phase from the other

$$\Delta\Phi = \Phi_1 - \Phi_2 \tag{2.36}$$

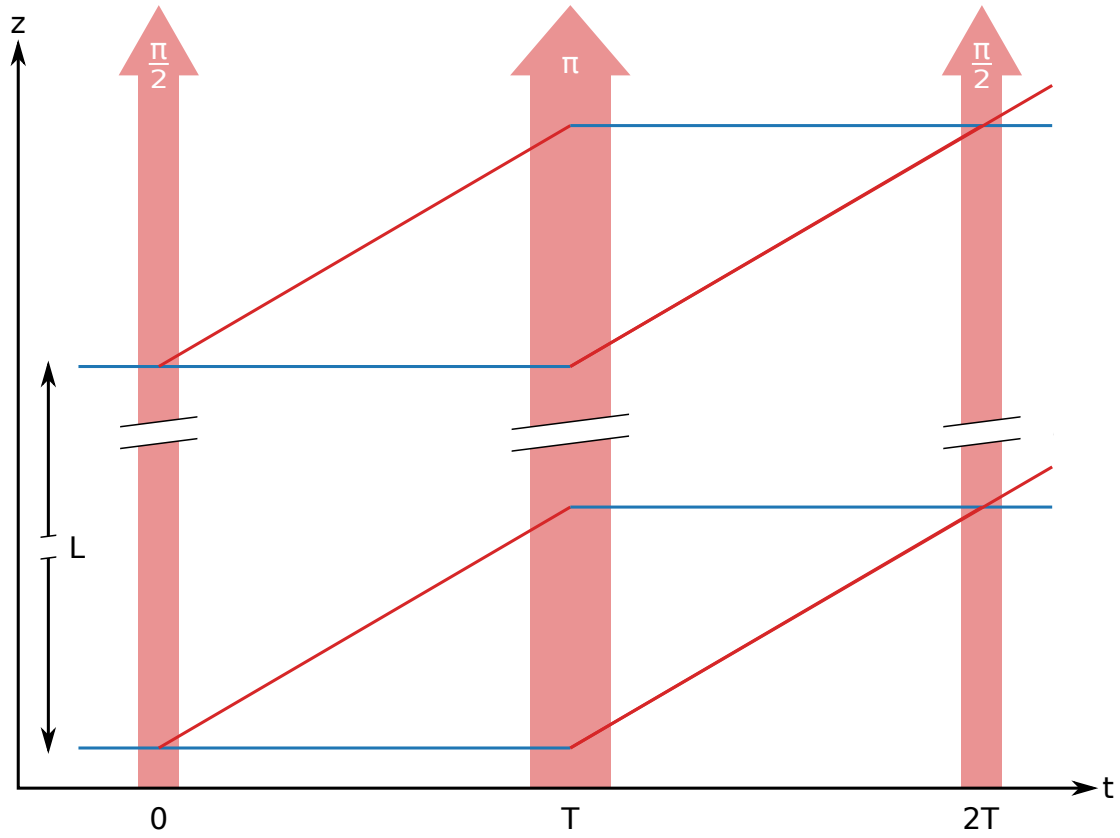


Figure 2.5: Space-time diagram for two Mach-Zehnder geometry atom interferometers in a gradiometer configuration. The atoms in both interferometers are initially separated by a baseline L. The blue and red lines show the trajectory of the two paths for an atom in state $|1\rangle$ and $|2\rangle$ respectively. The light pulses, shown by the red arrows, interact with both atom interferometers.

where $\Phi_{1,2}$ are the phases of the two interferometers. This relaxes the requirements for vibration isolation necessitated in non-differential measurements.

The relative phase is sensitive to effects such as a variation in the acceleration along the baseline or a change in the length of the baseline itself between pulses. A vertically aligned gradiometer configuration on Earth for example would be sensitive to the gravity gradient along the baseline [85].

2.1.7 Contrast and fidelity

The expression presented previously for excited state population as a function of phase, equation 2.27, is the ideal case. In reality, the oscillation will not have unity amplitude and it is necessary to introduce a scaling factor known as contrast C, such that $P = \frac{1}{2}(1 \pm C\cos\Phi)$ as illustrated in figure 2.6. This accounts for the fact that not all atoms at the beginning of the interferometer are still participating coherently at the end. Mechanisms which lead to loss of contrast include spontaneous emission, collisions with background atoms in vacuum and imperfect transfer of atoms between states.

The fraction of atoms transferred to the intended state by a given pulse is known as fidelity. A variety of effects act to limit pulse fidelity including dephasing and Doppler broadening due to finite cloud temperature. Atom optics in atom interferometry are typically produced by laser beams with Gaussian intensity profiles. Due to the non-zero spatial extent of the atom cloud, atoms will sample a variation in intensity, and hence Rabi frequency, as a function of their position. For a π-pulse this means that an atom off-centre in the beam will no longer have unity probability to undergo state inversion.

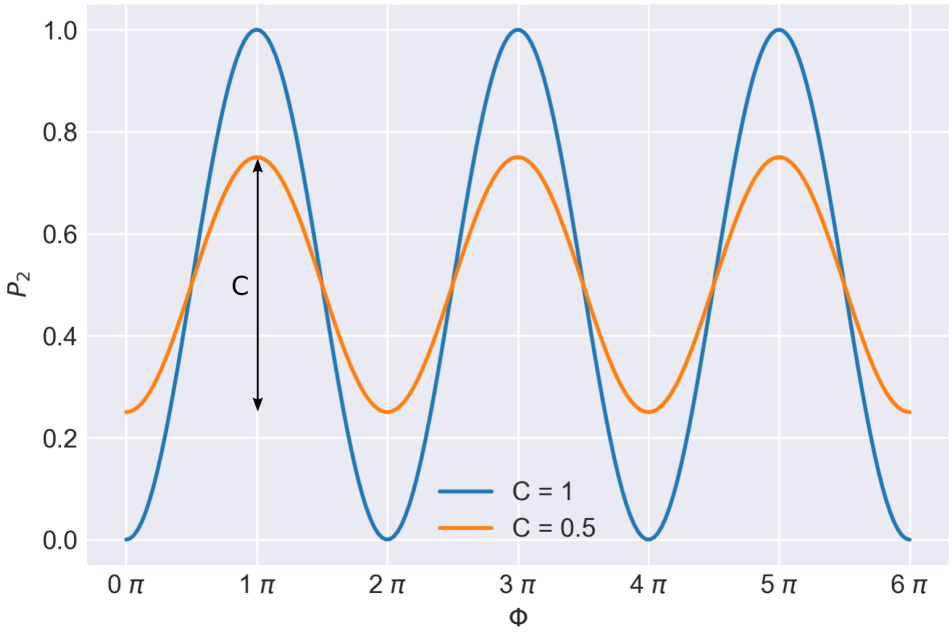


Figure 2.6: The excited state fraction for an atom interferometer with population initially in the ground state, as a function of interferometer phase. For contrasts $C < 1$ the fringe visibility is reduced.

The finite cloud temperature also results in dephasing. Atoms initially at the centre of the beam move radially outwards as a function of time and ensemble temperature. An additional effect of the temperature is that the atoms have a velocity distribution along the axis of the laser. Atoms with a non-zero velocity along this axis experience a detuning of the light due to the Doppler shift, changing the effective Rabi frequency and limiting the amplitude for population transfer. The effect of ensemble temperature on fidelity is expanded on in section 2.1.8.

Contrast loss affects the per-shot sensitivity of the atom interferometer and so efforts must be made to maximise fidelity and overall contrast. Loss of fidelity due to dephasing can be mitigated somewhat by using laser beam waists much larger than the atom cloud size, as well as low atom cloud temperatures. Achieving the best pulse fidelity therefore requires atom ensembles that are cold and dense. This motivates the use of techniques such as evaporative cooling or delta-kick cooling [86, 87]. Using shorter pulses also reduces the sensitivity to Doppler broadening since shorter pulses address a broader velocity class and vice versa.

2.1.8 Velocity selection

When considering a cloud of finite temperature, the atoms have a spread in velocity described by the Maxwell-Boltzmann distribution. Atoms of different velocities relative to the laser experience a Doppler shift of the light $-\mathbf{k} \cdot \mathbf{v}$. For light resonant with a given atom at rest, the relative motion Doppler shifts the light away from resonance and the dynamics of the Rabi oscillation are changed.

From equation 2.10 the probability of finding an atom in state $|2\rangle$, given it was

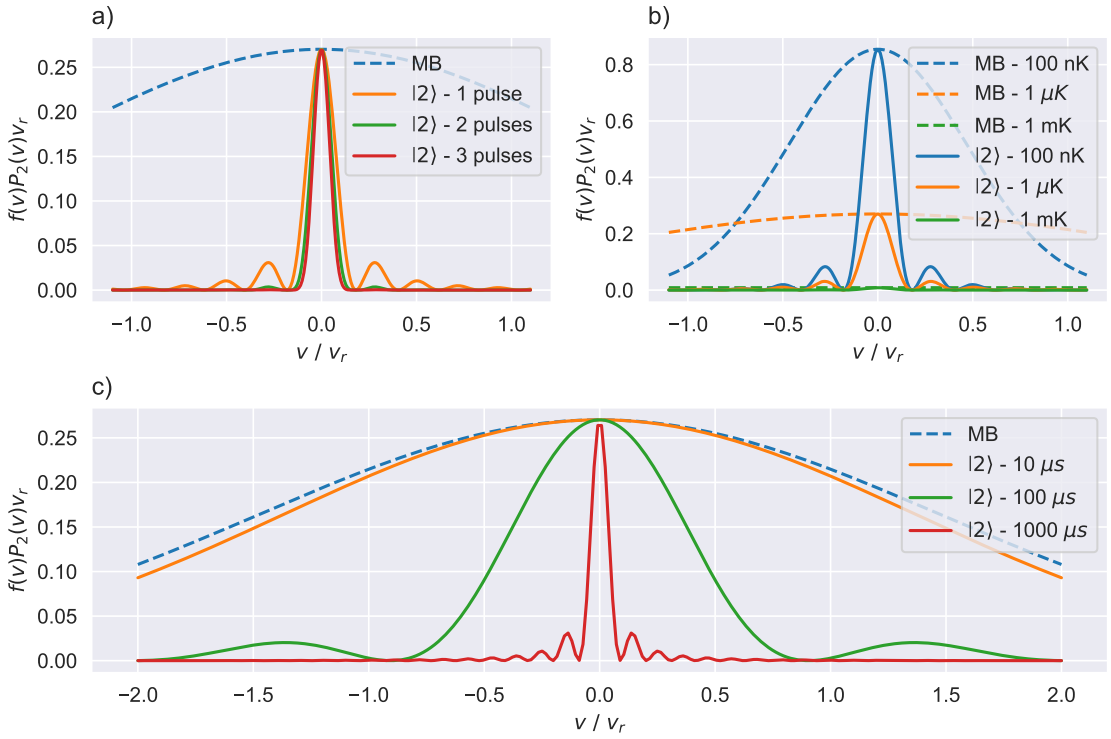


Figure 2.7: Velocity selective π-pulses for varying parameters. In each sub-plot dashed lines represent the normalised Maxwell-Boltzmann distribution and the solid lines show the normalised probability for an atom to be excited from the ground state as a function of velocity. a) Applying successive 500 μs pulses for a distribution of temperature 1 μK. Each successive pulse results in a narrower and smoother velocity distribution. b) The effect of temperature distribution on excited state transfer for a single 500 μs pulse. The colder the initial ensemble and hence the narrower the starting velocity distribution, the more efficient the population transfer. c) Different duration π-pulses for a distribution of temperature 1 μK. Longer pulse durations result in a narrower velocity class in the excited state but less efficient population transfer.

prepared in state $|1\rangle$ after the application of a π-pulse ($t = \pi/\Omega$) is

$$P_2 = \left(\frac{\pi}{2}\right)^2 \mathrm{sinc}^2 \left(\frac{\pi}{2}\sqrt{1 + \left(\frac{\Delta}{\Omega}\right)^2}\right). \tag{2.37}$$

If the the laser points along $\hat{\mathbf{z}}$ and the atom has a velocity component v_z, in the same direction, then $\Delta^2 = |\mathbf{k}v_z|^2$ and the equation becomes

$$P_2(v_z) = \left(\frac{\pi}{2}\right)^2 \mathrm{sinc}^2 \left(\frac{\pi}{2}\sqrt{1 + \left(\frac{|\mathbf{k}v_z|}{\Omega}\right)^2}\right). \tag{2.38}$$

The Maxwell-Boltzmann distribution says that for a gas of atoms with temperature T, the velocities are distributed according to

$$f(v) = \frac{1}{\sqrt{2\pi}\sigma_v} e^{-v^2/2\sigma_v^2} \tag{2.39}$$

with width $\sigma_v = \sqrt{k_B T/M}$ [88]. Neglecting any spatial variation in light intensity and hence Rabi frequency, the distribution of atoms that are excited to state $|2\rangle$ is the product of the two distributions from equations 2.38 and 2.39. The expected number of atoms in state $|2\rangle$ can be evaluated by integrating over the resulting distribution.

Figure 2.7 shows the velocity selective effect for different pulse durations and ensemble temperatures. It can be seen that shorter pulses and low temperatures are required to maximise transfer efficiency or fidelity. Longer pulses may be strategically deployed in order to isolate a narrow velocity class. For example, a long π-pulse could be applied followed by a blow-away pulse which removes the hotter atoms remaining in the original state. This process is known as velocity selection.

In any case, it is desirable to have the coldest possible starting distribution.

2.1.9 Atom interferometry in AION

The AION project aims to probe the parameter space of ultra-light scalar dark matter (ULSDM) candidates and detect mid-band gravitational waves (GWs). These manifest in different ways, and a detailed treatment can be found in the literature [89, 90]. A high-level intuitive explanation of the mechanisms for detection is provided here.

In section 2.1.3, the assertion is made that since the atoms spend equal periods of time in the two states, and the energy of the states is constant, the contribution due to the internal energy of the atom in $\Delta\phi_{propagation}$ is zero. The mechanisms by which GWs and ULSDM couple into the phase means that this assertion no longer holds true. Ultralight-scalar dark matter is predicted to cause a time-varying oscillation in the transition frequency between atomic states. In a gradiometer configuration, this would produce a differential phase shift between the two atom interferometers.

A gravitational wave passing through a gradiometer modulates the baseline, or distance between the two atom interferometers, at the frequency of the GW by an amount proportional to the baseline. This has two principal effects in the context of the interferometer phase. Since the baseline is modulated, so too is the time taken for the pulse to travel between interferometers, effectively changing T. As a result, the atoms no longer spend equal time in the two states, and the symmetry is broken. Secondly, the relationship between the phase of the laser at the different pulses is changed since the propagation distance is modulated and consequently

the ϕ_{laser} term in kz. However, if the time period of the gravitational wave is short compared to the T-time of the interferometer, the effect will be averaged out. So-called resonant-mode geometries have been proposed to effectively change the bandwidth of the measurement in order to be sensitive to different frequency bands [76].

In either case, technical laser phase noise cancels by virtue of the gradiometer configuration, leaving the signal of interest. In principle, this mitigates the requirement for the two perpendicular baselines employed by LIGO to control for laser noise. This is another advantage of performing atom interferometry with single-photon transitions, as discussed in section 1.1.3. Each atom optics pulse using two-photon Raman transitions requires two pulses of light, from opposite directions, to overlap at the atoms. For long baselines, if one pulse from a given direction interacts with both atom interferometers, the counter-propagating pulse from the other laser must be emitted at a different time to account for the propagation distance. The gradiometer would, therefore be susceptible to laser phase noise on this timescale.

2.2 Strontium

Strontium and its isotopes belong to a group of metals known as alkaline-earth metals. It sits between calcium and barium in group two of the periodic table, joined by beryllium, magnesium and radium. Other elements including ytterbium, cadmium and mercury are termed alkaline earth-like, since they also possess two outer shell electrons, and consequently share similar properties. The extra valence electron compared to group one metals such as rubidium and caesium gives rise

Table 2.1: Relative abundance and nuclear spin of the stable isotopes of strontium [94]. Only the fermionic isotope ^{87}Sr has nuclear spin.

Isotope	Abundance (%)	Spin
^{84}Sr	0.56	0
^{86}Sr	9.86	0
^{87}Sr	7.00	9/2
^{88}Sr	82.58	0

to richer, more complicated level structures. A more comprehensive treatment of the structure and intricacies of strontium can be found in the thesis of Martin Boyd [91]. That thesis and the theses of Andrew Ludlow and Simon Stellmer are invaluable in the context of working with strontium cold atoms experiments [92, 93].

2.2.1 Level structure

Table 2.1 shows the stable isotopes of strontium. Since strontium has atomic number 38, the even numbered isotopes have even neutron numbers. The protons and neutrons therefore arrange into anti-aligned spin pairs and consequently, the atoms have zero nuclear spin. As a result, it is only the fermionic isotope ^{87}Sr that has nuclear spin due to the last unpaired neutron. In this thesis, it is the most abundant isotope ^{88}Sr which is utilised, however, the experiment will transition to also using ^{87}Sr to take advantage of some of the benefits mentioned hereafter.

Figure 2.8 shows a reduced energy level diagram. The energy levels are described by the term symbol $^{2S+1}L_J$ where L is the total orbital angular momentum of the electrons, S is the total spin of the electrons, and J is the total angular momentum. Different configurations of the two outer-shell electrons lead to ^1L_J singlet states with $S = 0$ and ^3L_J triplet states with $S = 1$.

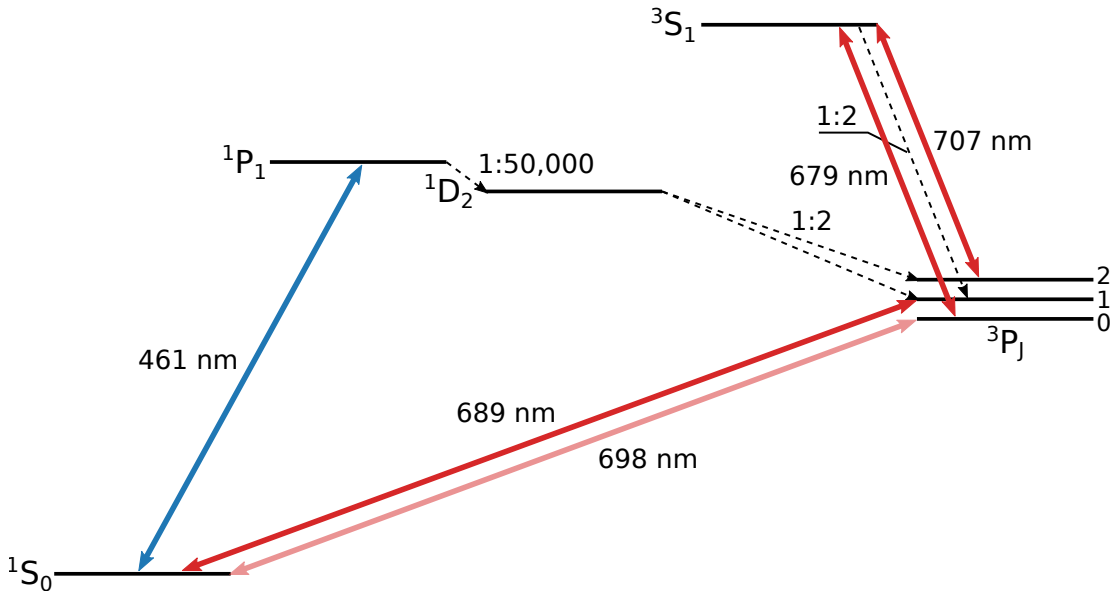


Figure 2.8: Simplified level structure for strontium showing the optical transitions and radiative decay paths relevant to this thesis. The radiative decay paths are shown with dashed arrows, and their approximate branching ratios are given. The $^1S_0 - {}^3P_0$ 698 nm transition is only innately present in the fermionic isotope ^{87}Sr.

The lowest energy excited manifold is the ^3P_J triplet state and the next lowest energy state is the $^1P_1$ singlet. The $^1S_0 - {}^1P_1$ transition is dipole-allowed and strongly coupled. Transitions between singlet and triplet states however are dipole-forbidden by the selection rule $\Delta S = 0$. As a result, the $^1S_0 - {}^3P_1$ transition in figure 2.8 should not be allowed but for the spin-orbit interaction which mixes a small amount of the $^1P_1$ state into the $^3P_1$ state, enabling a weak electric dipole transition [91]. This transition is known as the intercombination line. The $^1S_0 - {}^3P_0$ transition is doubly forbidden, but in the fermionic ^{87}Sr the nuclear spin gives rise to a magnetic dipole moment, and hyperfine coupling mixes in small amounts of the $^1P_1$ and $^3P_1$. Again this allows a weak electric dipole transition, but with an extraordinarily narrow linewidth and lifetime of 118 s [95]. This is the so-called clock transition.

Table 2.2: Relevant optical transitions in strontium [94, 95]. λ is the vacuum wavelength in nm, τ is the excited state lifetime Γ is the transition linewidth, I_s is the saturation parameter $I_s = \frac{\pi hc}{3\lambda^3\tau}$[88].

Transition	λ	τ	$\Gamma/2\pi$	I_s
$^1S_0 - {}^1P_1$	460.7	4.98 ns	32.0 MHz	43 mW cm^{-2}
$^3P_0 - {}^3S_1$	679.2	111 ns	1.43 MHz	0.60 mW cm^{-2}
$^1S_0 - {}^3P_1$	689.4	21.3 μs	7.46 kHz	3.0 μW cm^{-2}
$^1S_0 - {}^3P_0$	698.4	118 s	1.35 mHz	0.52 pW cm^{-2}
$^3P_1 - {}^3S_1$	707.0	23.6 ns	6.68 MHz	2.5 mW cm^{-2}

Whilst not ordinarily present, it is possible to induce the $^1S_0 - {}^3P_0$ clock transition in bosonic isotopes through the application of a static magnetic bias field [96, 97]. This again causes the $^3P_0$ to acquire a small admixture of the $^1P_1$ and $^3P_1$ states. For atom interferometry, it is difficult to generate a field of the required strength which is uniform over the whole interferometry region, and failure to do so can lead to large systematic phase shifts [55]. As a result, proposals for atom interferometers using the clock transition favour the fermionic isotope ^{87}Sr.

In the fermionic isotope, the non-zero nuclear spin I also gives rise to hyperfine structure $\mathbf{F} = \mathbf{I} + \mathbf{J}$. The $^3P_1$ state for example has three levels $F = 7/2$, $9/2$ and $11/2$ each with $2F + 1$ m_F levels. This leads to nuances when cooling the fermionic isotope compared to the bosonic ones, in that additional laser frequencies are required to address the hyperfine levels [91].

2.2.2 Cooling and trapping strontium

Cold atoms experiments rely on laser cooling to prepare atomic samples [88]. Zeeman slowers, magneto-optical traps and optical molasses depend on the technique [98–100]. In laser cooling, thermal atoms undergo absorption and spontaneous emission which, over many cycles, act to reduce the average velocity of the atoms.

The Zeeman slower uses a magnetic field gradient and laser light propagating in the opposite direction to an atomic beam to slow and cool ballistic atoms down to a few Kelvin [101]. Magneto-optical traps use red-detuned laser light and a quadrupole magnetic field to reduce the temperature of atoms to a few mK down to μk, depending on the transition. The level structure of strontium lends itself to laser cooling, but before discussing why, it is helpful to define capture velocity and the Doppler and recoil limit.

An atom in the beam of a laser resonant with a transition experiences a scattering force in the direction of the laser. This force is the rate of change of momentum given by $F_{sc} = \hbar k \Gamma \rho_2$, where Γ is the linewidth and ρ_2 is the excited state population. Written out, this is $F_{sc} = \hbar k \frac{\Gamma}{2} \frac{s}{1+s}$ where s is the saturation parameter I/I_s. For $s \gg 1$, the excited state population ρ_2 tends to 1/2, and hence the maximum force is $F_{sc} = \hbar k \Gamma/2$. The force causes an acceleration $a = F_{sc}/M$, and given a fixed stopping distance D, a corresponding capture velocity for an atom. The maximum capture velocity is $\sqrt{2aD}$ but is usually stated as half that

$$v_c = \sqrt{aD} \tag{2.40}$$

to provide a margin accounting for fluctuations in the photon scattering rate [77]. Capture velocity is an important quantity when designing an experiment as it informs decisions such as the length of a Zeeman slower or the width of MOT beams.

The Doppler limit, arising from the stochastic nature of spontaneous emission, is

$$k_B T_D = \frac{\hbar \Gamma}{2} \tag{2.41}$$

where k_B is the Boltzmann constant and Γ the linewidth of the transition. This limit is typically higher than the recoil limit, which is given by

$$k_B T_r = \frac{\hbar^2 k^2}{M} \tag{2.42}$$

where M is the mass of the atom. This is the kinetic energy from a single-photon absorption or emission. In the absence of sub-Doppler cooling, these two limits set the minimum temperature for laser cooling [88].

The above equations show that both the capture velocity and the Doppler limit are proportional to the linewidth of the cooling transition. Therefore, there is a trade-off when identifying a cooling transition. It is possible to either address a broad velocity class of atoms or cool the atoms to a lower temperature, but not both simultaneously. One of the benefits of the rich level structure of strontium is the cooling scheme it facilitates, and it turns out that you can both have your cake and eat it.

Depending on the atomic species used in a cold atoms experiment, the atoms are typically released into the experiment from an atomic oven, a dispenser or from the bulk material itself. The vapour pressure of strontium is low [102], and atomic ovens are typically favoured over dispensers. These ovens run at temperatures of approximately 450 °C and are designed to produce a collimated atom flux with minimal transverse velocity. From the Maxwell-Boltzmann distribution, the rms velocity of a beam at this temperature is ≈ 500 ms^{-1}, requiring a transition that can support a high capture velocity.

The almost-cycling $^1S_0 - {}^1P_1$ line at 461 nm is such a transition. The broad linewidth enables atoms to scatter photons at a very high rate, making it well-

suited to stopping thermal atoms in a Zeeman slower or 2D MOT. Operating a 3D MOT, the blue MOT, on the same transition then enables cooling down to a few mK. Parasitic transitions from the $^1P_1 - {}^1D_2$ state act to limit the trapped atom number, but this is overcome by repumping via other transitions, such as the $^3S_1$ state shown in figure 2.8.

The Landé g-factor of the $^1S_0$ ground state is much less than that of the excited state [91]. This means the magnetic sub-levels are effectively degenerate, precluding sub-Doppler cooling techniques employed with other species. Fortunately, a second cycling transition, $^1S_0 - {}^3P_1$, allows for further cooling of the atoms to a few μK in the so-called narrow-line red MOT. The sequential cooling on the two transitions is known as a two-stage MOT. The dynamics of the narrow-line MOT significantly differ from those in typical MOTs. A detailed discussion of the red MOT dynamics can be found elsewhere [91, 103].

The transfer from the first-stage blue MOT into the second-stage red MOT is not trivial. The broad velocity distribution of atoms following the blue MOT leads to a range in the Doppler shift of the narrow-line MOT light. The linewidth is Doppler broadened to a full-width half maximum of

$$\Delta\nu_D = \sqrt{\frac{8k_BTln2}{M}}\frac{\nu}{c} \tag{2.43}$$

where T is the temperature of the atoms, M is the mass of an atom, and ν is the frequency of the transition at rest [77]. Since atoms in the first-stage blue MOT have a temperature of a few mK, the intercombination line is broadened to approximately 1 MHz. To efficiently cool and capture atoms from the blue MOT into the narrow-line red MOT, it is necessary to intentionally frequency broaden

Table 2.3: The transitions used in the two-stage MOT of strontium with linewidth, saturation parameter, Doppler temperature and recoil temperature [94].

Transition	λ	$\Gamma/2\pi$	I_s	T_D	T_r
$^1S_0 - {}^1P_1$	460.9	32 MHz	43 mW cm^{-2}	770 μK	1.0 μK
$^1S_0 - {}^3P_1$	689.4	7.5 kHz	3 μW cm^{-2}	180 nK	460 nK

the cooling light or power broaden the transition. Either way, the broadening is ultimately ramped or stepped down into a single frequency narrow-line MOT, resulting in a sample at just a few μK.

Cooling below the aforementioned Doppler and recoil limits requires either sub-Doppler cooling, such as polarisation gradient cooling or techniques like evaporative cooling. Neither sub-Doppler cooling nor evaporative cooling in magnetic traps is applicable in strontium due to the insensitivity of the ground state to magnetic fields. Fortunately, another option presents itself in the form of optical dipole traps, which are applicable for strontium [104]. Self-scattering length is the figure of merit in determining whether an isotope is well suited to evaporative cooling [88]. Too high and atoms are lost from the trap through three-body collisions, too low, and thermalisation happens too slowly for cooling to occur. It turns out the self-scattering length of ^{88}Sr is too low but that of ^{87}Sr is favourable [105]. This isotope can be cooled to temperatures of order 100 nK.

2.2.3 Strontium in atom interferometry

The isotopes of strontium lend themselves to atom interferometry for a few reasons. The level structure is well suited to laser cooling, with two cycling transitions and two repumping transitions, all at wavelengths that can be generated with Ti:Sapph and diode lasers. This allows efficient cooling of samples to μK temperatures.

Moreover, the properties of ^{87}Sr allow cooling to temperatures of order 100 nK through evaporative cooling.

The forbidden transitions between the ground state and the first triplet manifold are coupled by single, optical-frequency photons. In the past, interferometry was typically performed using two-photon Raman transitions [78]. This requires two laser frequencies and is comparatively inefficient since greater optical powers are needed to compensate for the detuning required to mitigate off-resonant coupling to other states. Directly coupling metastable states with a single, resonant photon is a significant simplification. The 21.3 μs lifetime of the intercombination line is short in the context of typical atom interferometry experiments. Still, it is interesting since it supports high Rabi frequencies and hence many pulses in a short period [56, 57]. Through careful design of LMT pulse schemes, it is also possible to circumvent the lifetime limit [56]. By contrast, the 118 s lifetime of the clock state is so long that the effects of spontaneous emission can be neglected entirely for the purposes of atom interferometry.

One of the largest sources of systematic errors in atom interferometry is the Zeeman shift, wherein magnetic fields perturb the energy of a state. According to the first-order Zeeman shift, a field B lifts the degeneracy of the $m_{J(F)}$ sublevels of a state $J(F)$ having Landé g-factor $g_{J(F)}$ by an amount $\Delta\nu_B = g\mu_B m_{J(F)}B/h$ in the weak-field case [71, 77]. The effect of the first-order Zeeman shift can be negated by using a bias field to selectively drive insensitive transitions, but the second-order Zeeman shift remains an issue. The g-factor of the $^1S_0$ and $^3P_0$ states comes from the nuclear spin only, which is much smaller, leading to a reduced sensitivity of the energy levels to magnetic fields [91]. By comparison, the magnitude of the first-order Zeeman shift for the D2 transition in ^{87}Rb is of order 100 kHz G^{-1} compared

to 100 Hz G^{-1} for the transition in ^{87}Sr [91, 106]. This is another advantageous feature of the clock transition in strontium for atom interferometry. The g-factor for the $^3P_1$ state is larger though, making the intercombination transition more sensitive to magnetic fields. In ^{88}Sr, $g_J = 3/2$ and in ^{87}Sr, g_F of the three F levels are -1/3, 2/33 and 3/11.

Chapter 3

Experiment

The overarching aim of this experiment is to develop techniques and strategies to enable beyond state-of-the-art large momentum transfer with strontium. Design decisions are therefore made to facilitate this aim and to allow for the best possible pulse fidelity. Initial work focuses on the bosonic isotope ^{88}Sr. Compared to ^{87}Sr, the bosonic isotope is more abundant and simpler to cool from a laser system point of view, whilst offering interesting possibilities for atom interferometry on the intercombination line. The experiment is however designed to allow for future work with ^{87}Sr, to take advantage of the clock transition.

At its heart, the experiment is a strontium cold atoms system. This is the core apparatus responsible for generating the atomic ensembles, wave packets, with which atom interferometry is performed. The cold atoms are prepared within a vacuum system that comprises two chambers: Chamber One and Chamber Two, as shown in figure 3.1 and 3.3. An atomic beam leaving the oven under vacuum in Chamber One at a temperature of 700 K is initially slowed by a 2D MOT using light at 461 nm, detuned from the $^1S_0 - {}^1P_1$ transition. From there, atoms are

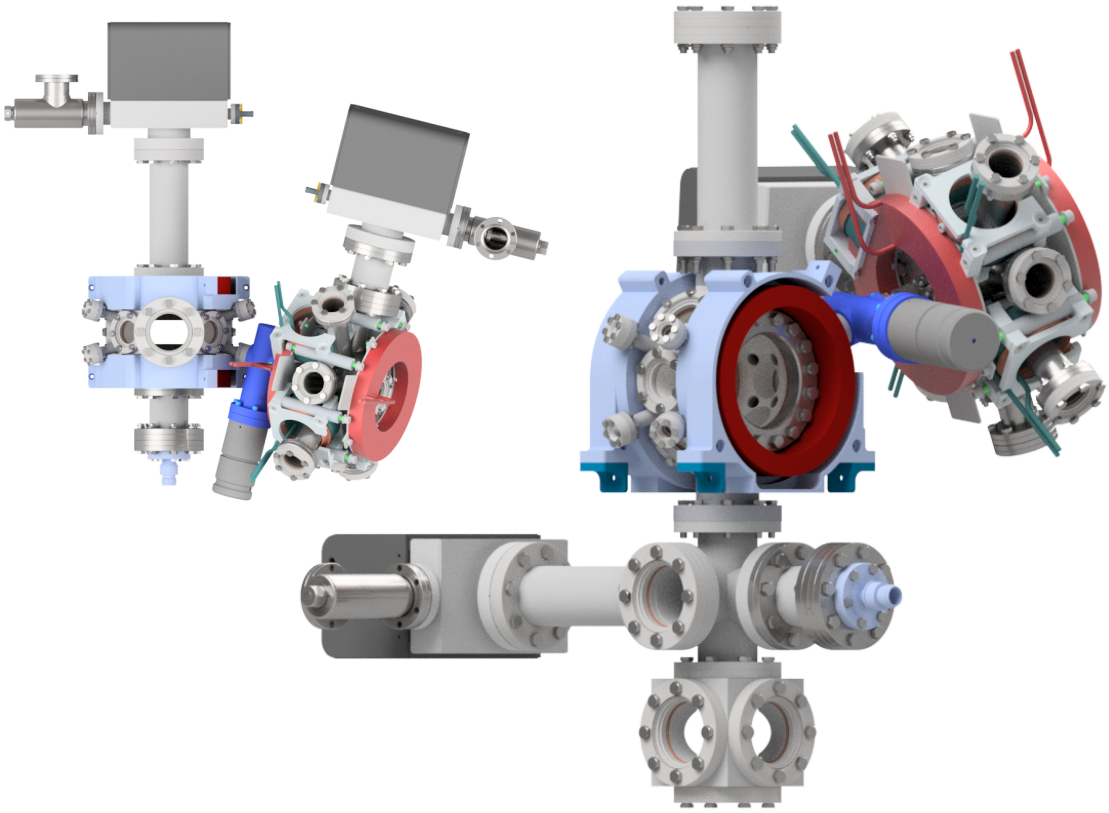


Figure 3.1: CAD renders of the vacuum system with magnetic field coils. The surrounding components and most of the support structure are hidden for clarity. The 3D MOT coils and 2D MOT axial shim coils are shown in red. On the left, the top-down view illustrates the angle at which Chamber One is attached to Chamber Two. An annotated schematic diagram of the vacuum chamber is shown in figure 3.3.

loaded into a blue 3D MOT in Chamber Two, assisted by a push beam on the same transition. Following the blue 3D MOT the atoms have a temperature of a few mK. These atoms are transferred into a frequency broadened and then narrow-line red 3D MOT on the $^1S_0 - {}^3P_1$ transition, with an ultimate temperature of a few μK. At this stage, additional cooling or velocity selection can be used to further reduce the sample temperature, or atom interferometry can be performed directly. Three wavelengths of light are used for the first-stage cooling, up to and including the blue 3D MOT. Lasers at 461 nm for the near-cycling cooling transition and 679 nm and 707 nm for repumping are all frequency-locked to a wavemeter. The second-stage cooling requires a fourth wavelength, 689 nm, which is derived from a laser locked to a stable, high-finesse optical cavity. The magnetic fields for the 2D MOT and 3D MOT are derived from permanent magnets and magnetic coils, respectively. Control and timing of the light and magnetic fields is orchestrated by the ARTIQ control system.

Several additional elements are required beyond the core strontium package in order to perform atom interferometry and to push the state-of-the-art in LMT.

- Atom interferometry laser and optical access for the interrogation beams. Viewports with anti-reflective coating and high optical flatness are required to minimise reflections and wavefront aberrations.

- A vertical free-fall region to enable fountain launches and large momentum transfer geometries.

- Detection system to measure the state populations after the interferometry sequence and optical access to allow efficient photon capture.

- Optical dipole trap apparatus to enable evaporative cooling and delta-kick cooling to below narrow-line MOT temperatures.

- Means to analyse and correct for aberrations in the interferometry beams.

There are also environmental requirements. For example, a low vacuum pressure is necessary to achieve a long optical dipole trap lifetime and long T-times [104]. Low residual magnetic fields are required, which can necessitate compensation bias fields. In atom interferometry, background magnetic fields introduce systematic phase shifts, and in cooling, they can limit the narrow-line MOT temperatures since the required magnetic field gradient is low. More broadly, it helps to have a quiet lab environment with stable ambient temperature.

3.1 Vacuum system

The vacuum systems, or 'sidearms', at the AION institutions, derive from a common design, enabling centralised, parallel construction of the sidearms at Daresbury Laboratory [107]. The Birmingham sidearm described herein, and shown in figure 3.3, shares the same design as the other sidearms within the AION consortium, except for a few notable differences.

The Birmingham sidearm is separated into two chambers. Chamber One, the 2D MOT chamber, is the point at which strontium atoms are released into vacuum from the atomic oven. Chamber Two is the 3D MOT and atom interferometry chamber. An extended free-fall region above and below the trap region in Chamber Two is one of the major distinctions between the Birmingham sidearm and other sidearms. This free-fall region facilitates various atom interferometry and large

momentum transfer schemes. The Birmingham sidearm also omits a third chamber present in other sidearms, Chamber Three. This chamber is intended for the development of atom transport techniques and sample rate improvement but is not essential for the aims of this experiment. Chamber One and Chamber Two are rigidly connected by a differential pumping aperture of 3 mm diameter and 17.3 mm length.

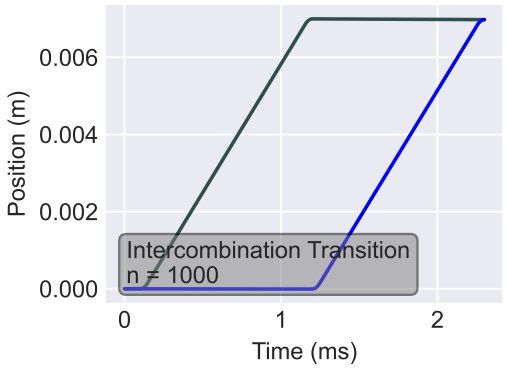
3.1.1 Free-fall region

Vertical free-fall distance for atom interferometry is one of the key specifications in the vacuum chamber design. Broadly speaking, there are two categories into which the space-time trajectories fall. Traditionally the trajectory is dominated by free fall under gravity, and the free-fall distance is large compared to the separation of the two atom interferometry paths. This scenario is applicable to atom interferometry carried out on the 698 nm clock transition since the π-times are long, and the lifetime supports long T-times. Conversely, in the regime of short pulses, high n LMT and short T-times, the photon recoil momenta dominate over gravity. When performing sequences using the 689 nm intercombination line, this regime is especially relevant. Here the π-times can be less than 100 ns, and T-times are constrained by the 21.3 μs excited state lifetime, in the absence of special techniques [56]. Provided the atoms are initially at rest, then the free-fall distance is negligible compared to the motion caused by photon recoils in large momentum transfer. Each photon recoil imparts a kick of $\sim$7 mm s^{-1}.

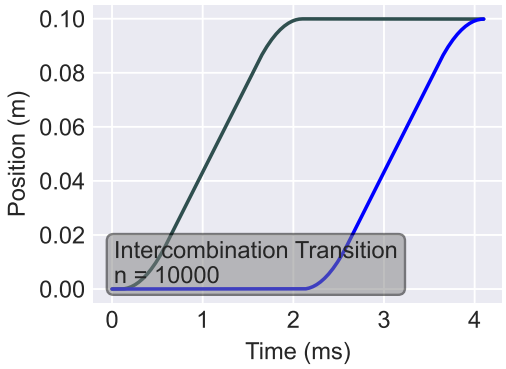
The vertical length of the atom interferometry chamber is informed by kinematic simulations of the space-time paths for different pulse schemes, illustrated in

figure 3.2. These show the space-time diagrams of some of the conceivable experiment schemes. For the purpose of these simulations, the simplifying assumptions are made that the two arms can be addressed independently or simultaneously and, crucially, that the 21.3 μs lifetime of the intercombination transition can be circumvented. In figures 3.2 (a), (b) and (d), the pulse scheme is broadly the same but with varying pulse timing and number of pulses. These schemes are extensions of the non-degenerate case discussed in section 2.1.5 and shown in figure 2.4a. An opening $\pi/2$-pulse is followed by n π-pulses, acting on the upper (grey) arm only, from alternating directions such that each pulse causes a momentum kick vertically upwards, resulting in a total momentum separation of $n\hbar k$. Following a drift time T, n π-pulses are applied, giving momentum kicks downwards to the same arm, undoing the additional momentum separation. A π-pulse is applied to both arms, inverting the state populations, before the same sequence of pulses is applied to the lower (blue) arm. Once the arms are overlapped, a final $\pi/2$-pulse closes the interferometer. In contrast, the scheme in (c) shows the degenerate case described in section 2.1.5 and depicted in figure 2.4b. In this case, following the opening $\pi/2$-pulse, n pulses act on both arms to cause a momentum separation of $2n\hbar k$. After a drift time T, $2n + 1$ π-pulses redirect the two arms towards one another. Then after another time T, n π-pulses act to undo the momentum separation so that the final $\pi/2$-pulse can close the sequence. For each simulation, the π-pulse durations and separation between pulses are taken to be constant.

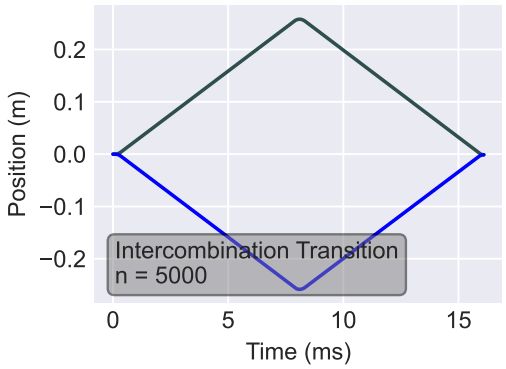
These simulations demonstrate how the path separation is predominantly influenced by the drift time T, and high orders of momentum separation can be achieved without the need for a long vacuum chamber. Even a modest vertical free-fall region of 50 cm should allow 10,000 $\hbar k$ separation, provided the time T



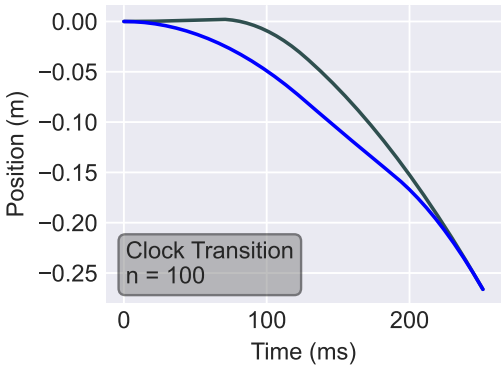
(a) 1000 $\hbar k$ on $^1S_0 - {}^3P_1$



(b) 10,000 $\hbar k$ on $^1S_0 - {}^3P_1$



(c) 10,000 $\hbar k$ symmetric on $^1S_0 - {}^3P_1$



(d) 100 $\hbar k$ on $^1S_0 - {}^3P_0$

Figure 3.2: Space-time simulations of various LMT schemes as described in the text. (a): $n = 1000$ on the intercombination transition, resulting in a momentum separation of 1000 $\hbar k$. The π-pulse duration and separation between consecutive pulses are 25 ns, and the drift time between sets of pulses $T = 1$ ms. (b): The same as (a) but with 10,000 $\hbar k$ separation as opposed to 1000. (c): 5000 pulses on the intercombination line address both the upper and lower arm to cause a momentum separation of 10,000 $\hbar k$. $T = 7.5$ ms, and the π-pulse duration and separation between pulses are again 25 ns. (d): 100 $\hbar k$ on the clock transition. $T = 10$ ms, and the pulse duration and inter-pulse time are 600 μs and 1 μs, respectively. Acceleration due to gravity is modelled in each sub-figure, but the effect is negligible for shorter timescales. The individual pulses are not illustrated, as there are too many to show. In (a), (b) and (c), the timing of the pulses is evident from the path curvature.

is of order a few ms. A limited time T is not an issue for the near-term goals of this experiment, where the purpose is to demonstrate the maximum LMT momentum separation whilst maintaining fringe visibility, as opposed to sensitivity. A schematic illustration of the chamber can be seen in figure 3.3. The vertical distance from the centre of the MOT region to the top viewport and the centre of the bottom detection chamber is 0.37 m. This distance is decided through simulations, space constraints in the laboratory and dimensions of off-the-shelf vacuum components. The free-fall region should also facilitate launches and gradiometry implemented through lattice techniques [54] or LMT pulses [56]. If atoms free fall from rest in the centre of the MOT chamber, the available free-fall time is > 250 ms. For a launch using the full height of the chamber, the available free-fall time is > 600 ms.

3.1.2 Atomic beam

Generating strontium samples requires a vapour, or beam, of strontium atoms released into the chamber. An atomic oven and 2D MOT are employed here to that end. The oven used in the AION sidearms, including the apparatus at Birmingham, is designed at the University of Oxford and manufactured at their workshop. This section provides a brief overview of the atomic oven, but the specifics are covered in depth in the thesis of Dongyang Xu [108].

The atomic oven is based on a tube attached to a DN40CF flange, which protrudes into the vacuum chamber. Six cartridge heaters, inserted into machined recesses, surround a reservoir containing bulk strontium and are responsible for heating the strontium. A steel nozzle with an array of 150 machined holes of 300

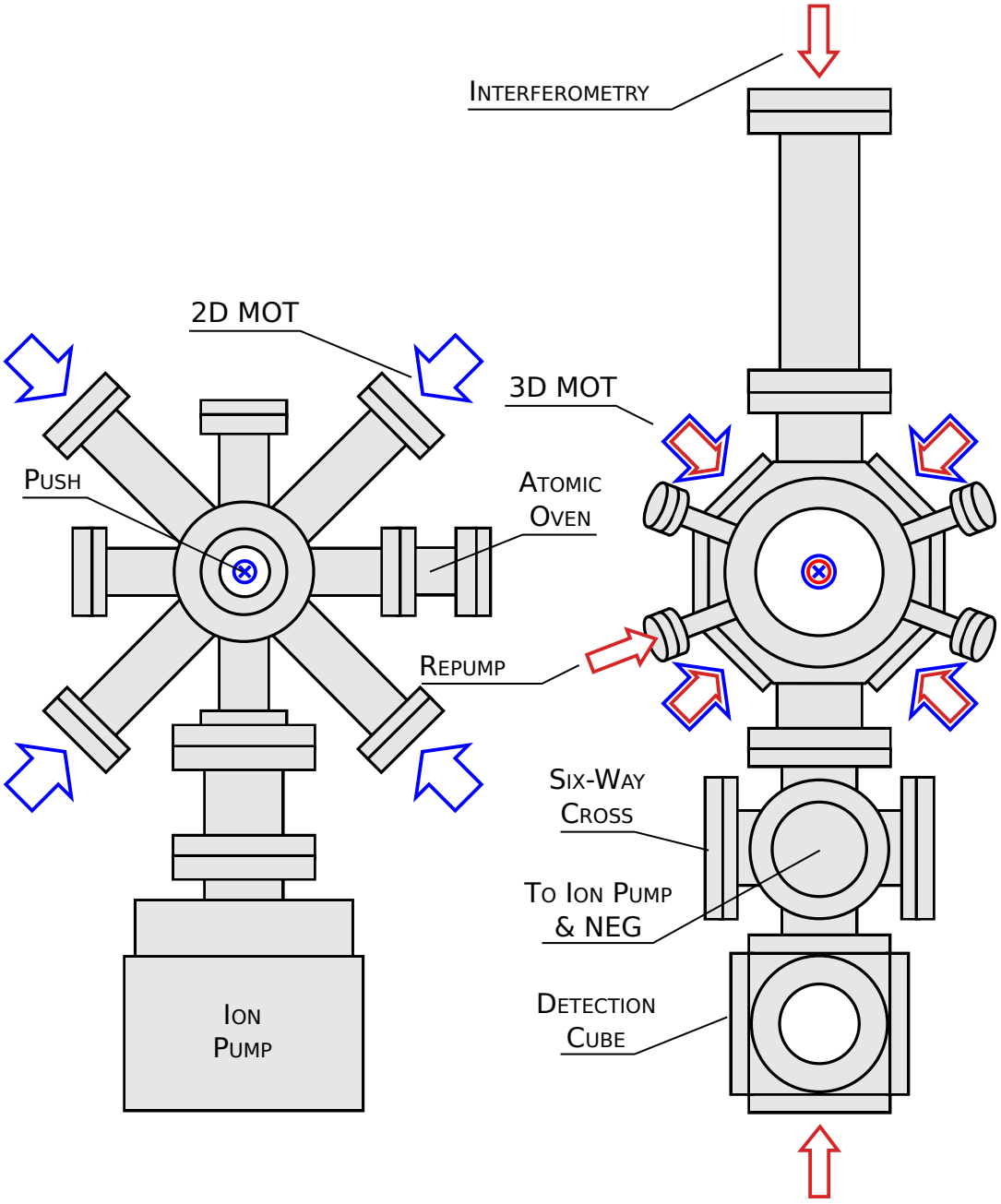


Figure 3.3: Chamber One (left) and Chamber Two (right) with the relevant light delivery illustrated. Both chambers are connected on the flange opposing the repump beam. CAD renderings of the side and top of the chamber are shown in figure 3.1. The large vertical region in Chamber Two allows a variety of atom interferometry geometries.

μm diameter and 3 mm length serves to collimate the atomic beam. Two further recesses around the oven locate thermocouple probes used for PID control of the temperature. One of the main advantages of the oven design is that it requires no vacuum feedthroughs or in-vacuum heating elements. The tube housing the oven is connected to the flange via a thin-walled section in order to minimise thermal conduction to the surrounding vacuum chamber via the flange. The atomic oven must be removed periodically to refill the crucible with strontium. A valve connecting the two chambers makes it possible to break vacuum in Chamber One without affecting Chamber Two.

To slow and cool the thermal atomic beam emanating from the oven requires laser cooling. A 2D magneto-optical trap is an effective alternative to the more commonly used Zeeman slower for slowing the flux from the atomic oven [101]. Atoms captured by the 2D MOT are transported to the 3D MOT using a low-intensity 461 nm beam along the connecting axis. This scheme avoids having the thermal atomic beam pass through the 3D MOT region. Loading the 3D MOT directly from a Zeeman slower would necessitate a mechanical shutter to prevent line-of-sight to the atomic oven during sensitive cooling and experimental processes such as planned evaporative cooling. Having the oven in a separate chamber from the science chamber also allows for efficient atom loading with improved pressures in the critical interferometry and trapping regions. Unlike using a Zeeman slower, there is also no requirement for a heated viewport opposite the atomic oven, reducing experimental complexity.

The decision to use a 2D MOT over a Zeeman slower is in part informed by AtomECS simulations [109] indicating a 2D MOT would provide a higher atom flux. However, with the available 461 nm laser power in this experiment, a hybrid

approach loading the 2D MOT with a Zeeman slower would likely outperform the 2D MOT presented here [110].

3.1.3 Optical access

Different aspects of the experiment require different optical accesses at a range of wavelengths, from visible to infrared.

- 2D MOT: Requires two pairs of counter-propagating 461 nm beams with axes that intersect at the centre of the 2D MOT chamber, with the atomic flux.
- Push beam: A unidirectional 461 nm beam propagating through the 2D MOT and 3D MOTs, in that order.
- Repump: Light at 679 nm and 707 nm propagating through the 3D MOT. Chosen here to be counter-propagating with the push beam such that the 2D MOT and pushed atoms are also illuminated.
- 3D MOT: Three pairs of counter-propagating, orthogonal beams at 461 nm and 689 nm, intersecting at the centre of the 3D MOT chamber.
- Interrogation beams: Vertical, counter-propagating beams at 689 nm passing through the centre of the 3D MOT chamber for atom interferometry.
- Detection: Uses 461 nm light delivered along the vertical interrogation axis and requires collection by detectors positioned radially.

Ideally, atom interferometry would be performed with perfectly flat optical wavefronts. An optical fibre delivering the light to the vacuum chamber acts as

a mode filter, but the reflection from and transmission through the subsequent optics introduces wavefront aberrations. One of the key metrics in selecting beam delivery optics is the optical flatness, and this extends to the viewports on the interferometry axis.

A CAD render and schematic diagram of the chambers are shown in figures 3.1 and 3.3, respectively. On Chamber One, there are seven DN40CF viewports. Four viewports on the two 2D MOT axes and one on the push axis deliver 461 nm light to the atoms. A viewport opposite the ion pump provides imaging access for the 2D MOT and a final viewport opposite the atomic oven is quickly coated with strontium when the oven is fired for the first time. Implementing a Zeeman slower on this axis would require a heated viewport to prevent strontium deposition. An aluminium gasket is used with this flange due to concerns that strontium could cause corrosion of annealed copper gaskets which are used on the viewports elsewhere.

Large aperture DN100CF viewports on the front and back of the 3D MOT region of Chamber Two are used to deliver the axial, horizontal 3D MOT light and also enable large numerical aperture imaging. Four DN40CF viewports on the two orthogonal MOT axes, in the vertical plane, deliver the radial MOT beams. Two further opposing DN40CF viewports on the horizontal axis passing through the MOT centre, in the radial plane, are used for the photodiode and ancillary camera described in section 3.5.2. Additional DN63CF viewports on the six-way cross and cube below the 3D MOT chamber allow for cloud imaging and detection after some free-fall distance. Additionally, there are seven DN16CF viewports around the 3D MOT region, four of which are intended for crossed optical dipole trap light delivery at 1064 nm.

Anti-reflection coating of the viewports is important to minimise power loss and interference effects resulting from reflections. This is especially true of the interrogation and optical dipole trap axes, which are all coated at the relevant wavelengths. All viewports are broadband anti-reflection coated at 440-800 nm, except for the DN16CF viewports, which are additionally coated at 1064 nm.

3.1.4 Vacuum pumping and performance

Imperfect vacuum can lead to losses during critical stages of the experiment, in particular during the atom interferometry sequence or evaporative cooling. These losses occur due to collisions between the strontium atoms and background atoms within the vacuum chamber. Ideally, these losses should be kept to a negligible level on the timescale of atom interferometry and evaporative cooling. The longest achievable free-fall time in the vacuum chamber is < 1 s, but evaporative cooling in an optical dipole trap can take from a few seconds up to 10 s [105, 111, 112].

A vacuum pressure of 5×10^{-10} mbar in Chamber One is maintained by a 45 L ion pump. The achievable pressure in this chamber is limited by the atomic oven, which would serve to increase pressure through heating, even in the absence of strontium vapour. In Chamber Two, a combination of a second 45 L ion pump and a NEG pump maintain a pressure of 2×10^{-11} mbar. These are the vacuum pressures estimated based on ion pump currents whilst the atomic oven is off. In normal operation, with an oven temperature setpoint of 420 ^{o}C, the pressure increases to 6×10^{-9} mbar and 2×10^{-11} mbar in Chamber One and Chamber Two, respectively. The lower pressure in Chamber Two relative to Chamber One indicates that the pumps and differential pumping are working effectively. Moreover,

the low pressures achieved in both chambers are a testament to the cleaning and vacuum preparation procedures carried out at Daresbury Laboratory as part of the centralised ultra-high vacuum (UHV) production [107].

The pressure in Chamber Two at the 3D MOT region is separately inferred via a measurement of the magnetic trap lifetime, details of which are presented in section 5.1.3. This technique independently finds the pressure to be 1.66×10^{-10} mbar. Since the 3D MOT and, hence, magnetic trap location is on-axis with the differential pumping aperture, it is reasonable to assume this places an upper bound on the pressure in Chamber Two.

3.2 Magnetic fields

3.2.1 Chamber One

The 2D magneto-optical trap in Chamber One requires a 2D quadrupole field, with the zero-field line aligned with the push axis connecting the 2D and 3D MOT centres. Permanent magnets are an attractive alternative to magnetic coils here, given the magnetic field does not need to be extinguished and does not affect the Chamber Two interferometry region. Coils would require dedicated power supply channels and may require passive or active cooling. Four permanent magnet holders, each with a pair of rare-earth permanent magnets, are located around the vacuum chamber. Figure 3.5a shows the arrangement of the magnets and simulated field lines for such a setup. Direct measurement of the radial field along one of the two 2D MOT light axes yields a gradient of (20.1 ± 0.6) G cm^{-1}, shown in figure 3.5b.

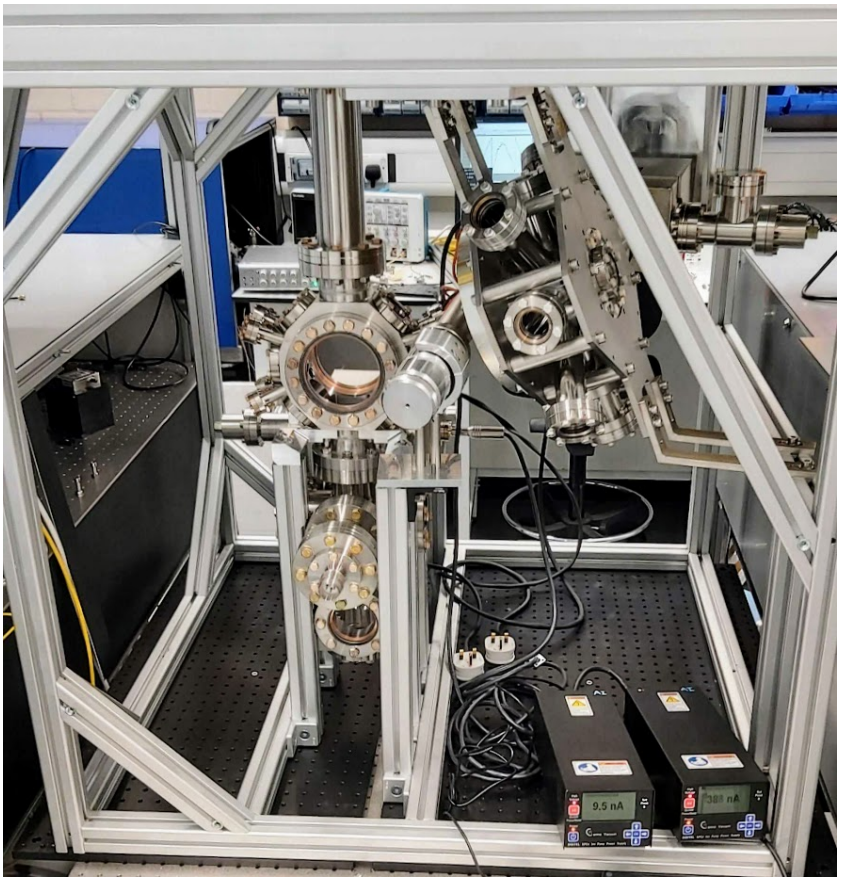
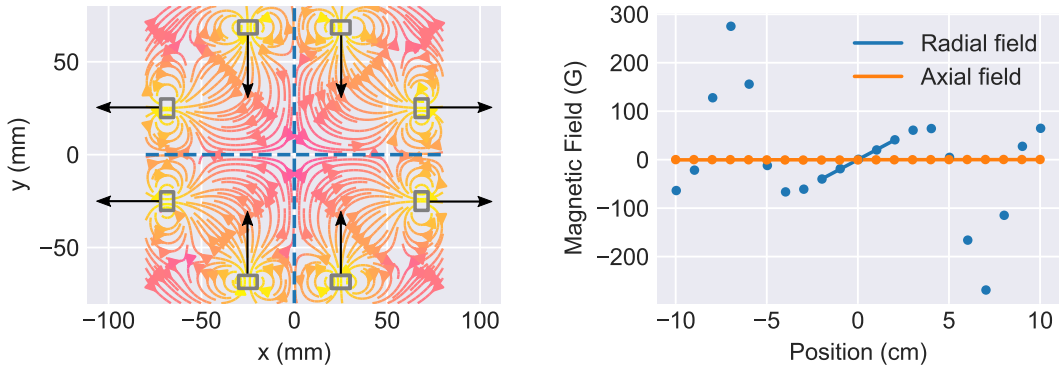


Figure 3.4: Installed sidearm following transport from Daresbury Laboratory. Chamber One is on the right of the image, and Chamber Two is on the left.



(a) Field simulation

(b) Measured field

Figure 3.5: (a): Simulated field of the 2D MOT permanent magnets on the plane intersecting the centre of each magnet. The magnet positions are marked by grey rectangles with north pole orientation shown by black arrows. The blue dashed lines represent the axes along which light is delivered. The field lines are simulated using the Python package Magpylib [113]. (b): The magnetic field from the 2D MOT permanent magnets, measured using a magnetic flux meter. The axial field is measured along the z-axis (x = 0, y = 0 in (a)). The radial field is measured along one of the 2D MOT light axes. The gradient of the linear region of the radial field is (20.1 ± 0.6) G cm^{-1} and the points recorded axially are within ± 1 G of zero. Error bars on the individual data points are too small to resolve.

Shim coils are located on either side of the 2D MOT chamber and built into each permanent magnet holder. In practice though, the permanent magnet field alone is found to produce a 2D MOT well aligned to the push axis, and these coils are not used. It is possible that optimisation of the shim coil current would yield a small improvement in the blue 3D MOT atom number or loading rate.

3.2.2 Chamber Two

In Chamber Two, the specifications for the quadrupole magnetic field are more stringent. Two distinct magnetic field gradients are required for the blue and red 3D MOTs, approximately 50 G cm^{-1} and 5 G cm^{-1} axially, respectively. The coils

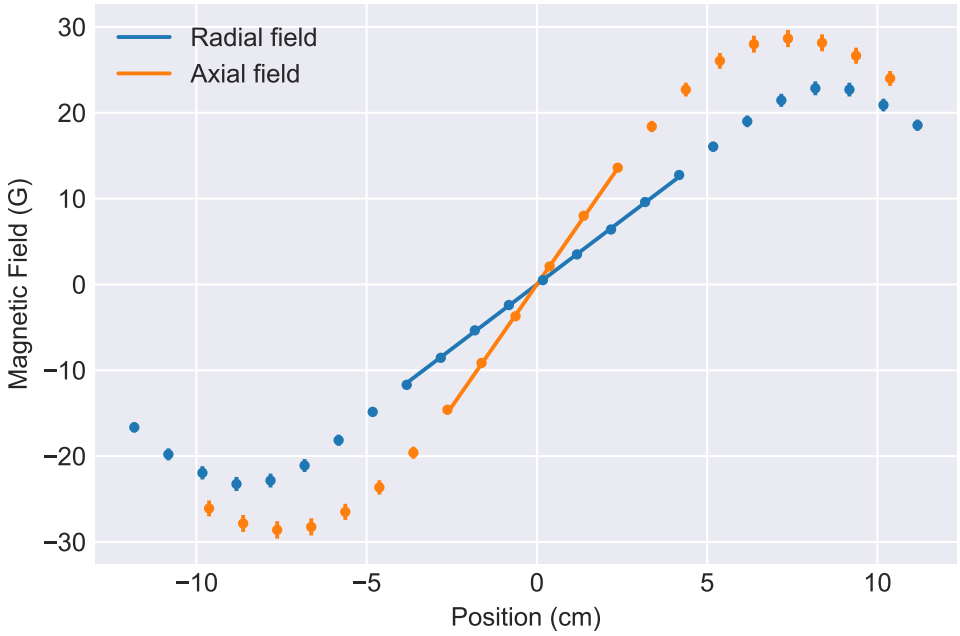


Figure 3.6: The axial and radial field for the 3D MOT coils, measured using a magnetic flux meter for a current of 15 A. The gradient of the linear region axially and radially are 0.380 ± 0.005 G cm^{-1}A^{-1} and 0.200 ± 0.001 G cm^{-1}A^{-1} respectively.

must be able to quickly switch from 50 G cm^{-1} to 5 G cm^{-1} between the red and blue MOTs and then to zero before interferometry. The coils should be able to switch on a timescale of order a few ms.

The dimensions of the coils are dictated by a few criteria. From the Biot-Savart law, the field gradient is proportional to the current, number of turns and inverse of coil radius and separation. Therefore, it is desirable to have the coils as small and as close as possible to reduce power draw and heating. The caveat is that the coils should not obstruct optical access of the viewports and cannot be closer than the width of the chamber. The field gradient should also ideally be constant

over the trapping region. The time constant of a coil is a function of inductance and resistance, $\tau = L/R$, and so inductance should be reduced. Coil inductance is given by $L = \mu_0 N^2 A/l$ where μ_0 is the magnetic permeability, N is the number of turns, A is the cross-sectional area, and l is the width of the coil. In practice, this means using fewer turns at a higher current will yield faster switching times.

To satisfy the above constraints and minimise the inductance, the quadrupole pair is designed with just 36 turns per coil. Both coils are connected in series such that the current in each coil flows in opposite directions, producing a field null at the trapping region centre. The measured axial field gradient is 0.380 ± 0.005 G cm^{-1}A^{-1}, from fitting to the data in figure 3.6. Producing a 50 G cm^{-1} gradient requires 132 A. Such a high current causes considerable heating, and so the coils are formed from hollow-core conductor through which coolant is pumped to prevent thermal runaway. Each 36-turn coil is also divided into two adjacent coils to enable cooling in parallel. The measured inductance of the coils is (156 ± 3) μH, corresponding to a time constant of 2.9 ms based on the measured resistance of 53 Ω.

3.3 Cooling laser system

The two-stage cooling scheme in strontium is explained in section 2.2.2. The first-stage cooling process requires light at 461 nm for the 2D MOT and blue 3D MOT and transfer between the two. 461 nm light is also used for cloud imaging and state detection following the interferometry sequence. As discussed in section 2.2.2, the parasitic $^1P_1 - {}^1D_2$ transition acts to deplete the blue MOT. Repump light at 679 nm and 707 nm is applied to bring atoms back into the cooling cycle via the $^3S_1$

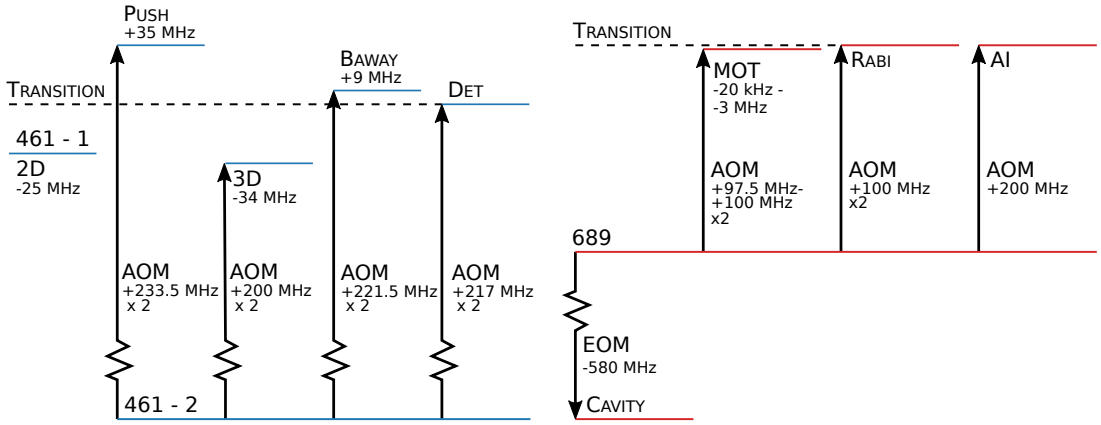
and $^3P_1$ states. Various different repump schemes can be employed [114–116], but external-cavity diode lasers (ECDL) conveniently address these two wavelengths. Linewidths of 32 MHz for the 461 nm transition and a few MHz for the 679 nm and 707 nm transitions relax frequency performance requirements on the corresponding lasers. Intensity stability over the course of seconds and minutes is more critical for consistent sample preparation.

The laser performance requirements are stricter in second-stage cooling. The narrower $2\pi\times$ 7.5 kHz linewidth of the intercombination line demands a commensurately narrow laser linewidth. To cool the atoms to the lowest temperatures in the red MOT requires a laser linewidth narrower than the linewidth of the atomic transition [103, 117]. As such, this laser is frequency stabilised to a high-performance optical cavity, and details of this setup are covered in section 3.4.

An eight-channel WS8 HighFinesse wavemeter enables the monitoring of all lasers and locking of the ECDL lasers. An iodine-stabilised HeNe acts as a reference for the wavemeter, and over the wavelength range of interest, the specified resolution and accuracy are 200 kHz and 2 MHz, respectively. The 461 nm, 679 nm and 707 nm lasers are all locked to the wavemeter, mitigating the need for spectroscopy. The WS8 wavemeter software facilitates PID locking of the laser frequencies via feedback on the piezoelectric transducer of each ECDL.

3.3.1 First-stage cooling

All lasers for the first-stage cooling are situated on the same optical bench, referred to here as the blue table and shown schematically in section 3.8. Two 461 nm lasers are used, MOGLabs injection-locked amplifier (ILA) units, each comprising an



(a) First-stage (b) Second-stage

Figure 3.7: (a): 461 nm light is derived from two lasers both locked below resonance to the wavemeter. Laser 461 - 1 is locked directly at the 2D MOT frequency. Laser 461 - 2 is locked further below resonance, and double-passed AOMs driven at the labelled frequencies are used to provide the push, blue 3D MOT, blow-away and detection light. (b): The -1 sideband of an EOM is used to lock the 689 nm laser to the nearest cavity mode below resonance. The frequency of the laser can be moved relative to the cavity mode by adjusting the EOM drive frequency. The atom interferometry light is derived using single-pass AOMs, whereas the red MOT and Rabi light rely on double-pass AOMs.

ECDL master laser and injection-locked slave diode (high-power Nichia NDB4916 diode). Each laser nominally outputs up to 200 mW on the ECDL output and up to 800 mW on the slave output. The master light not used for injection is output from a dedicated port on the laser unit, and some of this light is used to lock the lasers.

The 461 - 1 laser for the 2D MOT is locked at -27 MHz detuning, and the light is split into two fibres going to the ports of the 2D MOT. AtomECS simulations indicate an optimal power of 230 mW in 24 mm radial waist beams on the two axes. To maximise the available power, a mechanical shutter is installed instead of using an acousto-optic modulator (AOM) to switch the light. This is possible because the 2D MOT light can run in steady state, requiring neither intensity nor frequency modulation. Even so, the maximum power coupled here is approximately 150 mW per axis, and typical operating powers are closer to 120 mW. As a potential future upgrade, by reflecting a single beam through an open bowtie-style geometry, it should be possible to almost double the available power per beam. Currently, the installed Thorlabs SH05R shutters are not used at all during experiment runs, as the vibrations cause frequency issues with the blue table lasers.

On the master output of the 461 - 2 laser, light is picked off to go to the wavemeter for locking, and the remainder is frequency shifted by a double-pass AOM to give a blue detuning of 31 MHz for the push beam. The more powerful slave output is split into two paths, one for the 3D MOT light and one for detection. Both paths use a double-pass AOM, putting the detection light at resonance and detuning the 3D MOT light by -36 MHz. Figure 3.7a illustrates the way in which the relevant frequencies are derived.

Two MOGLabs ECDL lasers at 679 nm and 707 nm output a nominal 30 mW

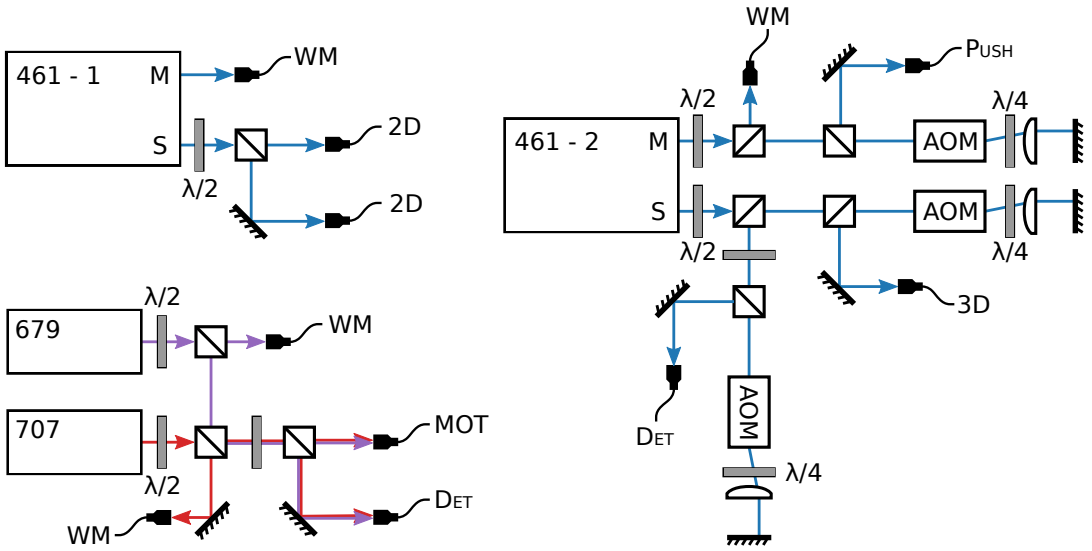


Figure 3.8: Two 461 nm ILA lasers provide the blue light. Each unit uses a master ECDL and slave diode laser. Light from the first 461 nm laser is split into two fibres for the two ports of the 2D MOT. On the second 461 nm laser, double-passed AOMs are used for frequency and intensity control of the push and blue 3D MOT light. Unused light from the master ECDL of each laser is split off to the wavemeter to which they are locked. The repump light comes from two ECDL lasers at 679 nm and 707 nm. The repump light is also locked to the wavemeter with pickoffs before the two frequencies are overlapped and coupled into two fibres for the MOT and detection.

each. The 707 nm ECDL struggles to meet this specification, and it is suspected that the required frequency is at the edge of the tuning range of the laser. Light from both lasers is overlapped and then split so that it can be delivered along the push axis, passing through the 3D MOT, but also on the vertical axis for detection. Both lasers are locked to the wavemeter.

3.3.2 Second-stage cooling

Second-stage cooling requires only one laser since the ${}^1S_0 - {}^3P_1$ transition is closed. The 689 nm red MOT light is derived from an M Squared SolsTiS Ti:Sapph laser,

as shown in figure 3.9. The specified output power is more than 2.5 W. However, since installation, the maximum output of this laser has fallen from 2.5 W to 1.5 W. This is suspected to be a result of degradation in the performance of the Equinox pump laser.

The schematic design of this laser system is shown in figure 3.9. Due to the narrow $2\pi\times$ 7.5 kHz linewidth of the intercombination line, frequency stabilisation to a reference cavity is necessary. A half-wave plate and polarising beam splitter (PBS) pick-off light for locking as well as wavemeter monitoring. Combining a Pockels cell and PBS enables dynamic reallocation of the 689 nm light between cooling and atom interferometry. The voltage supply used to drive the Pockels cell, an Ultravolt 4HVA24, has a considerably faster rise time than fall time, $\sim$1 ms versus $\sim$100 ms. The time to switch from cooling to interferometry is critical and needs to be kept as short as possible, so by default, the light travels to the MOT path, but by applying the half-wave voltage of the Pockels cell, the light is sent to interferometry. The red MOT light is coupled into one fibre and divided on the delivery breadboard, as with the blue 3D MOT. The AOM in double-pass configuration allows fast switching of the light and frequency ramping but is also used to apply frequency broadening during the broadband MOT phase. A portion of the light is split to the Rabi path for performing Rabi scans as described in section 5.3.1. In section 5.4.1, this laser path is used to perform Rabi scans and atom interferometry. This Rabi scan path is required since the dedicated atom interferometry setup described in section 4.2.1 uses single-pass AOMs that can't tune in frequency.

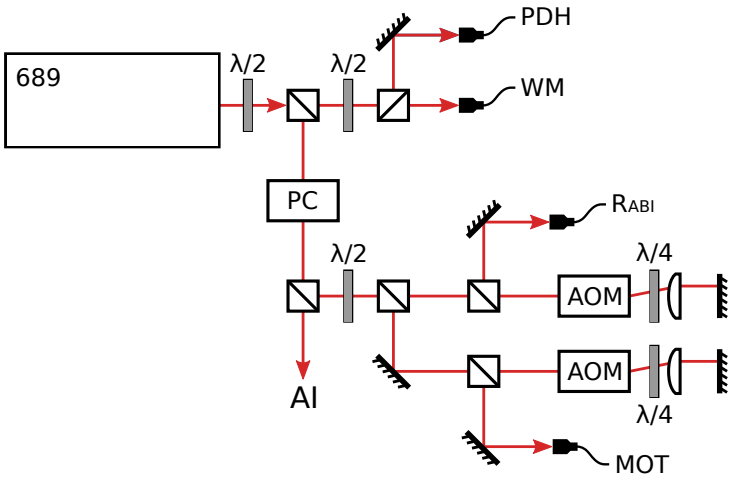


Figure 3.9: 689 nm light for second-stage cooling, Rabi scans and atom interferometry is derived from the same Ti:Sapph laser. A Pockels cell and polarising beam splitter allow dynamic allocation of light so that the majority of light can be available during interrogation. A half-wave plate and PBS pick off light, which is sent to the optical reference cavity for PDH locking and to the wavemeter for monitoring. The double-passed AOM enables the frequency tunability required for the second-stage cooling in the broadened and narrow-line MOT. The atom interferometry path is shown in figure 4.2.

3.3.3 Optical delivery

All light is delivered to the experiment from the laser tables via optical fibres. These serve to clean the spatial mode and decouple alignment but modulate the power and can introduce phase and polarisation noise. Power loss in-fibre is especially an issue for shorter wavelengths and so efforts are made to keep the 461 nm fibres as short as possible.

Two telescopes produce circularly polarised light for the 2D MOT, each with a $1/e^2$ waist of 20 mm and typical power of 120 mW. It is likely that elliptically shaped 2D MOT beams would yield a greater 2D MOT atom number and hence 3D MOT loading rate. The two beams are delivered via viewports on orthogonal axes. A mirror and quarter-wave plate on the two opposing viewports retroreflect each beam, flipping handedness. 0.25 mW of light collimated to a $1/e^2$ waist of 1.5 mm is delivered on the push beam axis running through the 2D and 3D MOT centres. Repump light is input along the same axis but in the opposite direction. 2 mW of 679 nm light and 2 mW of 707 nm light is delivered with a 3.4 mm radial waist. Delivering the repump light along this axis is found to yield a $\sim 2\times$ improvement in blue 3D MOT atom number compared to delivering through the DN100CF viewports.

The 461 nm and 689 nm light for two-stage cooling is delivered to an optical breadboard below the 3D MOT chamber. Both wavelengths are overlapped using a dichroic mirror and then split along three paths for the axial and two radial MOT axes, defined with respect to the MOT coils. As with the 2D MOT, the counterpropagating beams with opposite handedness on each axis are derived from a retroreflecting mirror and quarter-wave plate. Telescopes on the three paths

expand the beams, and the waists of the red and blue light can be set independently by changing the relevant collimator and, thus, input waist. At the time of writing, the waists of the red and blue beams are equal at 5 mm. The waist size is large compared to typical red MOT beam sizes. This is possible here because of the high power output from the Ti:Sapph laser as configured. In any case, the size of the narrow-line red MOT is primarily determined by the magnetic field gradient and the detuning of the light rather than the beam waists. In the 461 nm case, a total of 20 mW is split into two beams of 7 mW radially and one axial beam of 6 mW. During the frequency-broadened phase of the red MOT, a total of 60 mW is divided between the three axes in the same ratio as the blue beams. Achromatic waveplates are used downstream of the dichroic mirror where the two wavelengths are overlapped. As an interesting aside, the two radial beams are found not to require quarter-waveplates on the input. By setting the input polarisation with a half-waveplate, the mirrors sending the light to the chamber produce an ellipticity of 43^o, verified using a polarimeter.

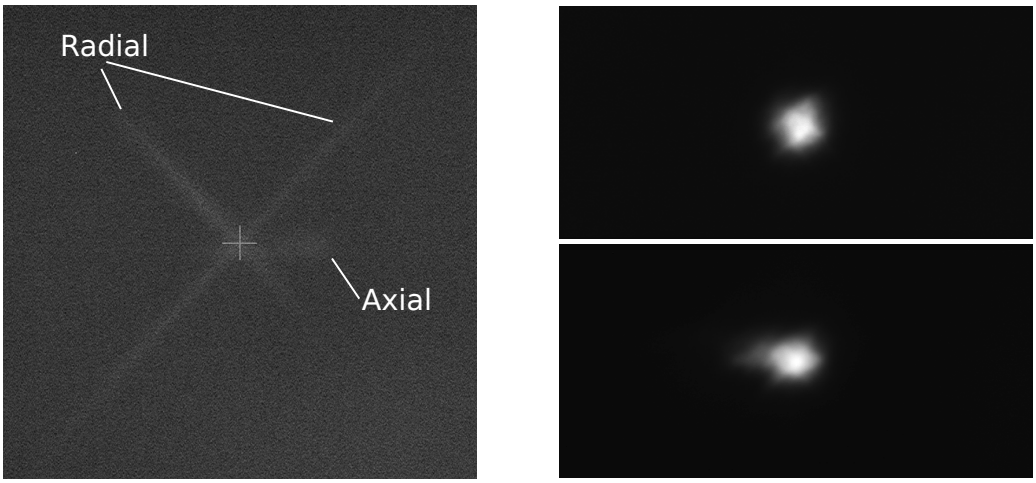
A limitation of the current design is that the alignment of the blue and red light are not independently adjustable. This is non-optimal since the centre of the red and blue MOTs are not necessarily spatially overlapped. However, this hasn't prevented achieving the narrow-line red MOT, and may not be an issue as a result of the large beam waists.

The push beam is aligned to maximise the 3D blue MOT atom number. Optimal alignment is found to have the push beam slightly offset from the 3D MOT since aligning through the MOT blows atoms out, as illustrated in figure 3.10b. Initial alignment of the 3D MOT light is carried out geometrically, using masks that attach to the viewports. The alignment is then improved through beam walk-

ing to increase the blue MOT atom number, and this simple approach is sufficient to observe a blue and broadband red 3D MOT. Beyond that, a more precise approach is desired. Alignment of the 3D MOT beams to the field null is achieved by leveraging the fluorescence of the atoms in the three pairs of 461 nm beams. Using scientific cameras on the large DN100CF viewport and side DN40CF viewport, it is possible to image the atom cloud, or fluorescence, in two vertical planes at roughly 45^o. By reducing the effective beam diameters with irises and observing the fluorescence in two planes, the three beam pairs can be made to intersect at a point. Then, by toggling the 3D MOT field gradient between a high and low value and observing the direction in which the atoms move, the intersection can be iteratively walked to the null of the field. Fringes in the atom cloud from the interference of the light can be observed when the beam pairs are almost perfectly counterpropagating. The retroreflected beam in each pair is slightly misaligned to avoid this issue.

3.4 Frequency stabilisation

To address the narrow-line 689 nm ${}^1S_0 - {}^3P_1$ transition, the linewidth of the Ti:Sapph laser must be reduced. This can be achieved in a few different ways, for example, by locking to an optical reference cavity or by beat note locking to a cavity stabilised frequency comb or another laser more stable in frequency. The approach employed in this experiment is to lock the laser to a high-finesse optical cavity via the Pound-Drever-Hall (PDH) technique [118, 119]. The laser stabilisation system, including electronics and optical delivery, is designed within the AION consortium by Imperial College and Rutherford Appleton Laboratories.



(a) Alignment (b) Push beam effect

Figure 3.10: (a): Fluorescence of the apertured blue MOT beams is used to align the 3D MOT light. (b): Effect of the push beam, directed from right to left, on the blue 3D MOT. Top: The push beam is misaligned slightly from the MOT. Bottom: The push beam passes through the MOT, causing degradation in the shape and an offset in position.

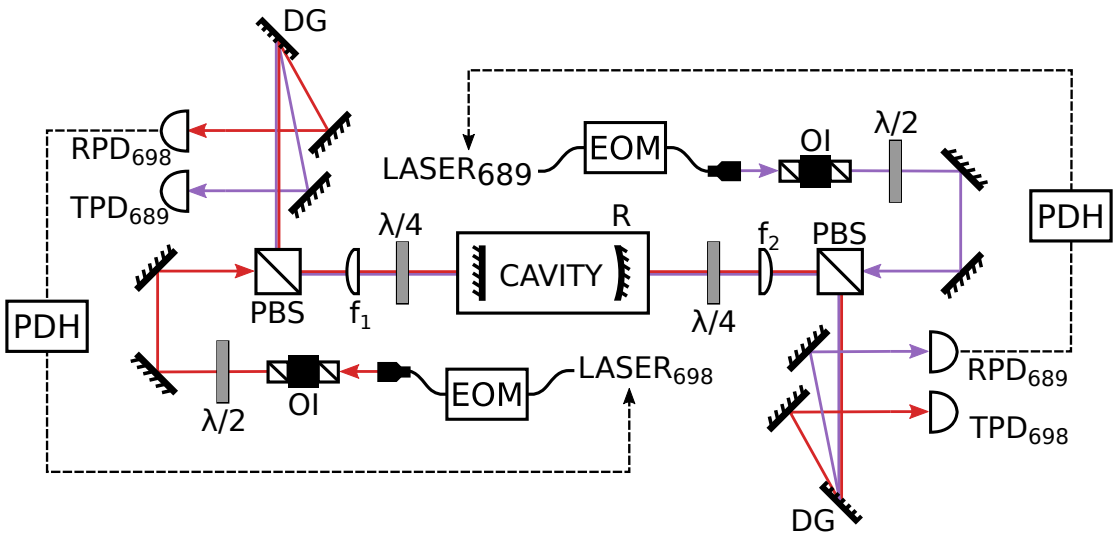


Figure 3.11: Schematic overview of the reference cavity breadboard for PDH locking two lasers at 689 nm and 698 nm. Light from both lasers is delivered in fibre and coupled into free space using a fibre collimator (FC) followed by an optical isolator (OI). A PBS and quarter-wave plate ($\lambda/4$) separate the ingoing light from light reflected or transmitted by the cavity, with a half-wave plate ($\lambda/2$) before the PBS set for maximum transmission of the ingoing light. On the reflecting port of each PBS, a diffraction grating (DG) reflects the cavity-transmitted light from one laser and the reflected light of the other onto the transmission photodiode (TPD) and reflection photodiode (RPD), respectively. Mode-matching lenses of focal length f = 200 mm optimise overlap with the cavity mode.

3.4.1 Reference cavity

The cavity is a Stable Laser Systems notched plano-concave Fabry-Perot cavity, with a 50 cm radius of curvature on the curved mirror. To mitigate the effects of mechanical and acoustic vibrations from the lab, the cavity is suspended on Viton balls within a vacuum enclosure held at 10^{-7} mbar by an ion pump. The notch design of the cavity reduces its inherent susceptibility to vibrations [120]. Further isolation is achieved by mounting the cavity vacuum system on an anti-vibration platform within an acoustically insulated enclosure. The cavity mirrors are optically bonded to an ultra-low expansion glass spacer, and heating elements within the chamber maintain the temperature at the zero-crossing of the coefficient of thermal expansion of the material. Sitting at this crossing makes the cavity length first-order insensitive to thermal fluctuations. Two layers of thermal shielding act as a low-pass filter against short-term temperature fluctuations.

The cavity finesse $\mathcal{F}$ is defined as the ratio of the free spectral range ν_{FSR}, the fundamental mode spacing, to the full width half maximum ν_{FWHM} of the lineshape, $\mathcal{F} = \nu_{FSR}/\nu_{FWHM}$. The cavity lineshape is related, in turn, to the cavity lifetime τ by

$$\nu_{FWHM} = \frac{1}{2\pi\tau}. \tag{3.1}$$

To measure the cavity lifetime, ringdown measurements are performed, and the transmitted intensity as a function of time is fitted to

$$I(t) = I_0 e^{-t/\tau} \tag{3.2}$$

where I_0 is the initial transmission intensity. The free spectral range of the cavity

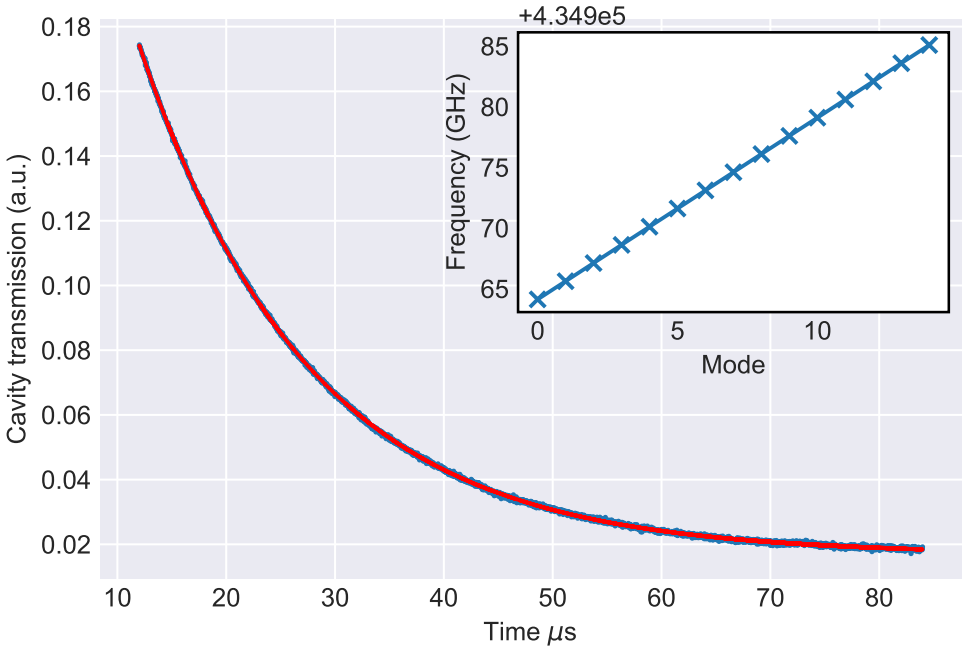


Figure 3.12: Typical cavity transmission ringdown measurement. The time constant from 20 traces is (15.6 ± 0.2) μs. Inset: From fitting to the frequencies of successive cavity modes, as measured using the wavemeter, the free spectral range is found to be (1.49753 ± 0.00001) GHz.

is measured to be 1.49753 ± 0.00001 GHz with a lineshape from ringdown measurements of 10.2 ± 0.1 kHz, corresponding to a finesse of 146000 ± 2000. An example ringdown dataset and the data from which the free spectral range is inferred are shown in figure 3.12.

3.4.2 Locking scheme

The current phase of the experiment requires narrow-linewidth light at 689 nm for cooling and atom interferometry. Future stages of the experiment will require 698 nm light to address the ${}^1S_0 - {}^3P_0$ clock transition. Stabilisation of the clock

laser will also be essential, and the frequency performance requirements are even stricter in this case as a result of the 1.35 mHz transition linewidth. The cavity apparatus is therefore set up to facilitate simultaneous locking of both 689 nm and 698 nm light. One inspired feature of the design is the use of a diffraction grating to separate the two wavelengths. The two wavelengths of light can be locked to the same cavity without a diffraction grating by modulating light from both lasers at different frequencies. However, you would compromise the ability to independently monitor the transmission and reflection signals of the two lasers. Coupling of both wavelengths is achieved in the same way but on opposite inputs of the cavity, as illustrated in figure 3.11. On each side, light is coupled in fibre from the optical table to the cavity breadboard, and a fibre electro-optic modulator (EOM) applies the modulation necessary for PDH locking. An optical isolator prevents transmission of back reflections to the laser. A mode-matching lens is used to overlap the ingoing mode with the mode of the cavity. A PBS separates the reflected light from the ingoing laser, which is sent to a fast photodiode for locking, from the transmitted light from the other side, which is used for monitoring.

For the laser at 689 nm, the signal from the high-bandwidth photodiode is amplified and then demodulated by a ZRPD-1 phase detector. After demodulation, the error signal is passed to a Vescent DS-125 PIID controller, and feedback is applied to the Ti:Sapph's fast piezo input. The servo controller gains are optimised by minimising the peaks in the frequency spectrum of the residual error signal, as shown in figure 4.6. For optimal lock performance, the first integrator cutoff frequency is set to 5 kHz, the second integrator to 20 kHz, and the differential term to 50 kHz. Characterisation of the locked laser performance is shown in section 4.2.2.

3.5 Detection

Extracting the phase at the close of the atom interferometry sequence requires a measurement of the relative state populations through detection. This is typically achieved via fluorescence imaging or absorption imaging [121], employing resonant or near-resonant light to probe the atoms. In the case of fluorescence imaging, the sensor captures light which is scattered via spontaneous emission. In absorption imaging, the detection light propagates towards the sensor perpendicular to its surface, and the sensor measures the shadow of the atoms caused by absorption of the light. In fluorescence imaging, the fraction of scattered photons incident on the detector is set by the solid angle fraction since the atoms scatter photons uniformly in all directions. Conversely, in absorption imaging, the scattered photons not incident on the sensor contribute to the signal. The fraction of photons detected is, therefore, higher in the case of absorption imaging. In practice, a low probe beam intensity is required so as not to saturate the sensor, and this limits the absolute number of photons which can be detected.

Either a photodiode or scientific camera can be used as the detector. Camera-based detection has an advantage in that it offers spatial information about the imaged atoms. This can enable simultaneous imaging of the two atomic states, provided that they are spatially separated. It is also a requirement of phase shear enhanced readout [122]. Additionally, camera-based detection allows for the characterisation of sample temperature via time-of-flight (TOF) measurements [123, 124].

The blue ${}^1S_0 - {}^1P_1$ cycling transition, used in cooling, is also used in performing detection. Compared to the ${}^1S_0 - {}^3P_1$ and ${}^1S_0 - {}^3P_0$ transitions, the broader

linewidth yields a much higher scattering rate for a given light intensity. This allows for an improved signal-to-noise ratio and state-dependent detection with the transitions of interest in atom interferometry.

3.5.1 Camera imaging

State detection in this experiment uses a camera for the advantage of being able to perform spatially resolved state detection. This will also enable the characterisation of large momentum transfer beam splitter sequences where the two states can be macroscopically separated. The camera used is an Andor iXon Ultra 888 electron-multiplying charge-coupled device (EMCCD) with a blue light band-pass filter for background light rejection. The camera is currently aligned to image at the 3D MOT region, at an approximate angle of 30^o to the axial MOT axis.

The impressive photon sensitivity of the iXon camera proves to be an issue when attempting to perform time-of-flight imaging of the blue MOT. During the blue MOT, the pixels become over-saturated and imaging before the built-up charge can be drained from the sensor reveals a 'ghost' of a MOT. This can be mitigated by either waiting for a sufficiently long duration that the charge has drained or by using the physical shutter of the camera to shield the sensor from unwanted light. The physical shutter of the iXon camera is found to open approximately 20 ms before the global shutter, which places a lower limit on how soon imaging can take place after the blue MOT.

Initial atom interferometry on the ${}^1S_0 - {}^3P_1$ transition is performed on timescales of order 20 μs, the approximate state lifetime. In this case, the free fall distance of the atoms is minimal, as shown in section 3.1.1, and a single camera can both

image the MOT and perform state detection at the close of the interferometry sequence. Planned experiments involving longer atom interferometry sequences and drop times will require detection to be performed below the MOT region. The detection chamber, connected below the MOT chamber, facilitates this, and the detection camera can be relocated accordingly. In this case, a secondary camera will be required for MOT temperature characterisation and diagnostics. A Lucid Vision Labs Triton TRI0204S-MC CMOS camera is already installed to this end, at an angle of 120^o to, but on the same horizontal plane as the Andor camera. This configuration images the atoms in bisecting vertical planes, which is useful for tasks such as MOT optimisation, beam alignment and background magnetic field characterisation. The peak in the quantum efficiency curve of both cameras lies close to 461 nm, making them well suited for detection on the ${}^1S_0 - {}^1P_1$ transition. The quantum efficiencies of the iXon and Triton at this wavelength are $> 85\%$ and $> 72\%$, respectively.

3.5.2 Detection sequence

At the close of the atom interferometer, the atoms are divided between the two states as a function of the interferometer phase. State detection is commonly achieved by sequentially measuring the population of the two states or by measuring the population of one state and then both states combined. This is usually made possible by imaging the atoms using a different transition to the one used for interferometry, selectively causing atoms in one state or the other to fluoresce.

In the case of the ${}^1S_0 - {}^3P_1$ transition in strontium, one could image the ground state atoms using the blue ${}^1S_0 - {}^1P_1$ transition whilst the excited state atoms are

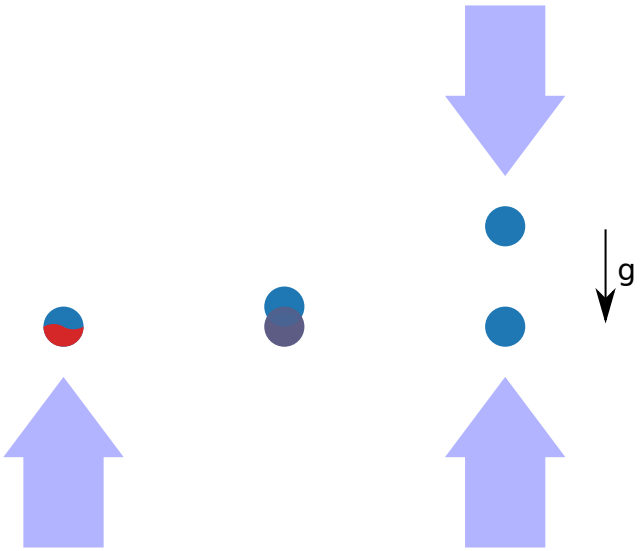


Figure 3.13: A pulse from a beam of unbalanced (unidirectional) light resonant with the ${}^1S_0 - {}^1P_1$ transition propagates vertically upwards, accelerating the atoms initially in the ground state. These atoms are pushed away from the pulse-insensitive atoms in the ${}^3P_1$ state. After some propagation time, the two atom clouds are spatially resolvable, and all atoms have decayed to the ground ${}^1S_0$ state. A balanced (retroreflected) pulse on the vertical axis then illuminates the clouds for fluorescence imaging.

effectively shelved. One could then either blow away those ground state atoms or not and detect the excited state population or combined populations, respectively. However, to precisely measure the phase via the relative state populations, one must somehow resolve the two populations before a significant fraction of excited state atoms can decay. Since the lifetime of the $^3P_1$ state is so short, 21.3 μs, the states should be resolved within just a few μs of the end of the atom interferometer sequence. To perform sequential detection on this time scale would be experimentally very challenging. Consequently, a different approach must be taken.

The detection sequence presented here relies on an unbalanced pulse of 461 nm light with a duration <10 μs, blue detuned by 7 MHz from the $^1S_0 - {}^1P_1$ transition, which selectively pushes the ground state atoms vertically upwards. Those atoms travel away from the atoms occupying the excited state at the close of the sequence, which meanwhile decay into the ground state. After a delay of order 10 ms, the two populations are spatially separated, and the excited state atoms have all fallen back to the ground state, at which point a resonant detection pulse is applied, imaging both clouds. This detection scheme is illustrated in figure 3.13.

A schematic for the optical delivery of the detection beams is shown in section 4.2.1, figure 4.5. A single 461 nm beam is delivered from below the chamber and retroreflected above. Compared to dividing the light into two vertical beams, this effectively doubles the available optical power, enabling shorter blow-away or push pulses. The light is magnified to a 7.5 mm waist to minimise the effects of spatial intensity variation over the cloud, which is anticipated to have a radial waist of about 200 μm once optimised [54, 56, 125]. A lens with a mirror at its focal

distance forms a 1:1 telescope, allowing the beam to pass through a mechanical shutter without clipping. This shutter is closed to deliver unidirectional push pulses and open for balanced, retroreflected detection pulses. The shutter rise time of <1 ms places a lower limit on how soon the balanced detection pulse can be implemented after the push or blow-away pulse. Due to the critical nature of the pulses, the frequency, timing and intensity of each pulse are still controlled by the AOM.

3.5.3 Photodiode

One drawback associated with using a camera compared to a photodiode is the limited measurement bandwidth. The maximum frame rates of the Andor and Lucid Vision Labs cameras are 26 frames per second (FPS) and six FPS, respectively. When performing combined two-state detection, this is a non-issue, but for measuring signals that vary more quickly in time, such as MOT loading curves, it can be prohibitive.

For this reason, a photodiode is located on the horizontal plane of the 3D MOT, on the DN40CF viewport opposite the Triton camera. It is also more straightforward to increase the solid angle of a photodiode, compared to a camera and lens system, as a camera requires an image to be formed at the sensor, whilst a photodiode only requires that the light be focused within the sensor area. A 50 mm diameter lens is used with the photodiode, and the solid angle is instead limited by the 38 mm inner flange diameter. The solid angle fraction is 0.012.

3.6 Timing, control and data acquisition

Precise temporal control of all aspects of the experiment is essential. The durations and sequence of the steps must be executed exactly for repeatable sample preparation. These requirements are critical during the interferometry sequence, where timing jitter and pulse duration errors can lead to phase error and pulse fidelity reduction.

For this experiment, several different capabilities are demanded of the timing system. DDS and high-frequency synthesizer channels are required to drive the AOM and EOM RF signals in the laser system for timing and frequency control. DAC channels are used for controlling the 3D MOT coil current and hence field gradient. TTL channels trigger fast RF switches, mechanical shutters, cameras and data acquisition.

3.6.1 ARTIQ

ARTIQ, or Advanced Real-Time Infrastructure for Quantum physics, is open-source hardware and firmware designed for control of quantum physics experiments. A Python-based programming language is used to write experimental sequences that run on a field-programmable gate array (FPGA) with ns timing resolution.

The ARTIQ infrastructure provides flexibility in selecting the modules to be used. ARTIQ hardware used in this experiment is supplied by M-Labs. The crate is configured with one master and one satellite Kasli, four Urukul DDS boards, one Mirny synthesizer board, four TTL boards, a Fastino DAC board, analog-to-digital converter (ADC) Sampler board and Grabber CameraLink board.

3.6.2 ndscan

The ndscan library for ARTIQ, developed by the Oxford Ion Trap Group, proves to be one of the most indispensable tools for this experiment. ndscan introduces the functionality of building block 'fragments' from which experiment code can be composed. The framework allows for automated, randomised N-dimensional scans over all experiment parameters, plotting results channels in real-time. This is very useful when optimising experiment parameters, running calibrations, or otherwise acquiring data.

Chapter 4

Laser systems for strontium atom interferometry

The $^1S_0 - {}^3P_1$ intercombination line in strontium is a unique and interesting transition in the context of atom interferometry. It is optically coupled by a single photon, like the $^1S_0 - {}^3P_0$ transition in ^{87}Sr, and in contrast to the two-photon transitions employed in the majority of preceding work. Unlike the $^1S_0 - {}^3P_0$ transition, which requires a strong driving electric field due to the weak coupling, the intercombination transition readily supports Rabi frequencies of several MHz. Whilst the $2\pi\times$ 7.5 kHz linewidth supports high Rabi frequencies, enabling interesting large momentum transfer schemes, the corresponding 21.3 μs lifetime raises its own technical challenges.

In previous single-photon large momentum transfer demonstrations, the degree of momentum separation that can be achieved with visible fringe contrast is predominantly limited by spontaneous emission and pulse fidelity [56, 57]. Rudolph et al. overcome the issue of spontaneous emission during the interrogation time

T, between LMT π-pulse groups by shelving both atom interferometer arms in the ground state [56]. This facilitates T-times not limited by the excited state lifetime. However, the fundamental limitation of spontaneous emission during the LMT pulse sequences remains.

In a degenerate large momentum transfer atom interferometer, the opening beam splitter sequence, comprising a $\pi/2$-pulse and n_π sequentially counterpropagating π-pulses, imparts a momentum difference between arms of $2n_\pi + 1$ $\hbar k$. A mirror sequence of $2n_\pi + 1$ further π-pulses reverses the momentum of the two paths before n_π more π-pulses and a $\pi/2$-pulse closes out the interferometer. $4n_\pi + 1$ π-pulses are therefore required for a momentum separation of $2n_\pi + 1$ $\hbar k$ in the degenerate case. An interferometer with 201 $\hbar k$ maximum momentum separation between arms requires 401 π-pulses. Assuming a π-pulse duration of 100 ns and neglecting the time between individual pulses, this amounts to 40.1 μs. Since each pulse flips the internal state of the wave functions of the two paths between the ground and excited state, any given atom spends half the time in the excited state. This means each atom cumulatively spends approximately 20 μs in the excited state, almost equal to the excited state lifetime 21.3 μs. The LMT sequence need not fit within the lifetime, but for each passing lifetime, the maximum achievable contrast is diminished by a factor e.

Since the AI per-shot sensitivity scales with the imparted momentum separation between interferometer arms, it is desirable to increase the order of LMT as far as possible. Moreover, given the lifetime of the transition, the greater the repetition rate of the pulses, the greater the momentum separation it is possible to impart within the limits of spontaneous emission. Implementing large momentum transfer pulses on the ${}^1S_0 - {}^3P_1$ transition in strontium requires a laser at 689 nm

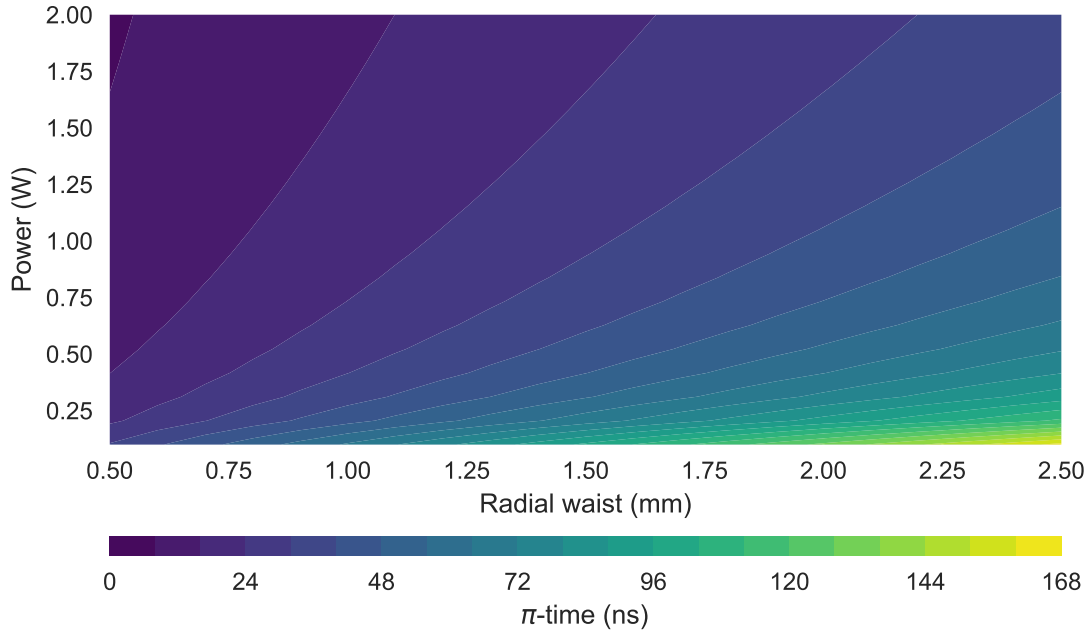


Figure 4.1: π-pulse duration for the ${}^1S_0 - {}^3P_1$ intercombination transition as a function of optical power and beam waist, from equation 4.1. For a single strontium atom at the centre of a Gaussian laser beam, resonant with the transition.

which is both narrow and stable in frequency and which can deliver optical powers sufficient to drive short pulses. Figure 4.1 shows the achievable π-pulse durations for varying optical power and beam waists. The Rabi frequency for a single atom resonant with the driving field is

$$\Omega = \sqrt{\frac{I}{I_{sat}}}\frac{\Gamma}{\sqrt{2}} \tag{4.1}$$

where I is the intensity of the beam, I_{sat} is the saturation parameter and Γ is the transition linewidth [77, 88]. The contour plot is based on the peak intensity for a Gaussian beam, $I_0 = \frac{2P_0}{\pi w_0^2}$ where P_0 is the laser power and w_0 is the beam waist [126]. Given optical powers currently available in commercial continuous-wave lasers, it is possible to access $\sim$10 ns pulses. In this regime, the act of shaping such short pulses becomes technically challenging. Indeed, the π-pulse durations might not be limited by available laser power but by the hardware and timing electronics which shape the pulses.

Shorter pulses confer the additional advantage of a broader pulse bandwidth and reduced velocity selectivity, as discussed in section 2.1.8. This is especially relevant when the Doppler shift between the atoms and the laser is dominated by the recoil momenta from LMT pulses. Unlike the common Doppler shift from free fall, a single frequency cannot simultaneously track the oppositely shifting resonant frequencies of both interferometer arms. Here, the laser frequency should be located centrally between the resonant frequencies of the two arms, relying on the pulse bandwidth to address them.

This chapter covers the details of the laser system used to perform atom interferometry on the ${}^1S_0 - {}^3P_1$ transition, designed to push the state-of-the-art in

large momentum transfer. Pulse durations of 30 ns and repetition rates of 30 MHz are demonstrated. The shortest reported atom interferometry π-pulses, to the author's knowledge, are 100 ns [57]. Typical pulse lengths in 'traditional' atom interferometry experiments are considerably longer though, of order a few μs [17, 127, 128]. The performance requirements of the atom interferometry laser are stricter compared to those of the cooling lasers. Limited laser performance in cooling can result in non-optimal sample temperatures and shot-to-shot variation in atom number, for example. In atom interferometry, the intensity, frequency and phase noise directly cause deleterious effects in the measurement phase and contrast. Characterisation of the frequency performance of the laser is also presented in this chapter.

4.1 Pulse shaping

Short π-pulses of duration < 100 ns are novel in atom interferometry. Other applications exist requiring short pulse times, such as cavity Q-switching, pulse picking from ultrafast lasers and pulse slicing [129, 130]. Whilst pulse lengths are comparable to those desired here, the requirements in atom interferometry differ in critical ways. Firstly, atom interferometry requires the continuous-wave light to be extinguished perfectly, or at least near-perfectly, between pulses. Secondly, the aforementioned use cases typically do not demand high, sustained repetition rates as required in atom interferometry on the ${}^1S_0 - {}^3P_1$ transition.

4.1.1 Techniques for pulse shaping

Different techniques exist for shaping pulses, each with advantages and drawbacks. The technique best suited to a given application depends on the requirements. This context necessitates short switching speeds of order 10 ns, high power handling of 1 W or more and repetition rates exceding 10 MHz. Examples of devices used for pulse shaping include optical switches, Pockels cells and AOMs. Fibre-based optical switches are either too slow or limited in the power they can handle. Mechanical-based options are much too slow and would lack the precision to enact π-pulses reliably. Therefore, an AOM or Pockels cell is likely the best solution for fast pulse shaping.

A Pockels cell located between orthogonal polarisers functions as an optical switch. Applying the half-wave voltage of the crystal results in a rotation of the light polarisation axis such that the transmission goes from a minimum to a maximum. The rise time can be very short, on the timescale of a few ns, and is typically limited by the driving electronics and capacitance of the cell and associated connectors. BBO Pockels cells are well suited to fast pulse shaping, with typical optical transmissions of >98%, damage thresholds of $\sim$1 GW cm^{-2} and low capacitances supporting switching times of a few ns or better. The intrinsic contrast ratio of a Pockels cell, of order 1000:1, can limit the extinction of the switch when set to 'off', still allowing a fraction of the light to pass. This may be reduced to an acceptable level using an additional cell and polariser in series or a single cell in a double-pass configuration. Since the Pockels cell half-wave voltage is typically a few kV, driving the cell at a high repetition rate is technically challenging. The fastest Pockels cell drivers can achieve repetition rates of $\sim$10

MHz. However, driving pulses with repetition rates exceeding 1 MHz can cause piezoelectric ringing, which significantly reduces the contrast ratio of the cell [131].

Shaping pulses using an AOM is much simpler from a driving electronics standpoint. Generic RF components can be used instead of high-voltage electronics. The rise time, in the case of AOMs, is limited by the time taken for an acoustic wave to propagate across the beam waist in crystal. By focusing a laser beam through an AOM, rise times of < 10 ns can be achieved. A limitation of this approach is that the rise time is inversely proportional to the beam waist, but the AOM diffraction efficiency also scales inversely with the beam waist. A trade-off must be made between rise time and efficiency.

Single-photon large momentum transfer using ultrafast lasers presents an interesting avenue for future research. Two-photon atom interferometry using a picosecond laser has been demonstrated with rubidium [132]. In this work, thousands of pulses were required to achieve population transfer as a result of the low Rabi frequency and requirement for counterpropagating pulses to overlap at the position of the atoms. High-probability coherent population transfer on a single-photon transition has also been demonstrated in the context of ion trapping experiments [133]. The relatively high Rabi frequencies supported by the intercombination line in strontium make it an interesting transition in this context.

4.1.2 Implementation

Performing large momentum transfer using a single-photon transition requires two counter-propagating and overlapped laser beams. In this experiment, the two atom interferometry beams are delivered vertically and the light for the upward

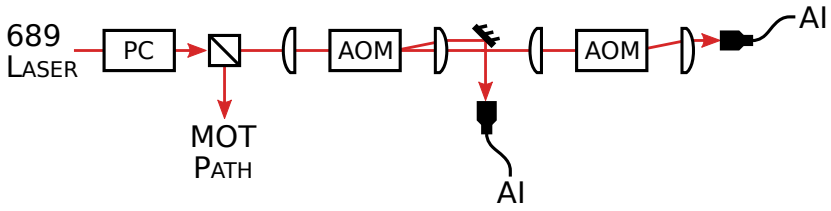


Figure 4.2: Sequential single-pass AOM arrangement controlling atom interferometry pulses for the two vertical beams. Mode-matching telescopes for the two fibre couples are not shown. The schematic for the cooling path, derived from the same laser, is shown in figure 3.9.

and downward beams is controlled by two AOMs. The decision to use AOMs over Pockels cells is motivated by the need for short, high repetition rate pulses. A Pockels cell-based approach may still prove useful when shaping pulses to address the ${}^1S_0 - {}^3P_0$ clock transition. Achievable pulse lengths are much longer in this case, and the increased pulse efficiency and damage threshold afforded could be advantageous.

The design of the atom interferometry laser is shown in figure 4.2. Both AI AOMs are operated in single-pass as opposed to double-pass configuration. This allows for improved efficiency at the expense of frequency tunability. As discussed previously, in this regime, the Doppler shift is dominated by recoil momenta in opposite directions for both interferometer arms, rendering it impossible to compensate. The two AOMs are arranged in series with the undiffracted zeroth order of the first AOM seeding the second AOM. The zeroth and first order of the first AOM are separated using a D-shaped mirror, and only one AOM is driven at a time. Not dividing the optical power between the two AOMs effectively doubles the power available to each, enabling higher intensities, shorter π-times and increased momentum separation. This scheme could be extended to double-pass in order to

track free-fall Doppler shifts over longer T-times at the expense of efficiency.

As discussed, there is a compromise between the AOM diffraction efficiency and the switching time. The rise and fall time of an AOM depends on the time it takes for the acoustic wave to propagate across the beam in the crystal. As such, the switching time is a function of the beam waist, and the shortest rise and fall times are achieved by focusing to a tight waist through the AOM. Achieving the best possible diffraction efficiency, however, requires that the light satisfies the Bragg condition $n\lambda = 2\sin\theta$. Peak efficiency is achieved for paraxial incoming light, but focusing to tighter waists effectively increases the range of angles of the incident light. Further, one observes a significant roll-off in efficiency beyond a certain angle as rays at extreme angles begin to populate adjacent diffraction orders. To realise the fastest rise times, an AOM must be placed at the focal point of a converging lens. The diffraction-limited spot size for such a lens is given by

$$w_f = 1.22\frac{f\lambda}{w_0} \tag{4.2}$$

where f is the focal length of the lens, and w_0 is the waist of the ingoing beam incident on the lens [134]. A shorter focal length lens yields a tighter beam waist, but it demands more precise AOM positioning due to the increased rate of change of the beam waist with respect to axial distance. An achromatic lens will also produce a more tightly focused waist when compared to singlet lenses. Figure 4.3 shows how for a given focal length, the rise time is much shorter for an achromatic doublet than a singlet lens. The two rightmost points are produced using achromat lenses, showing that despite having the largest predicted waists, they have the shortest rise times and improved rise time-to-efficiency ratios.

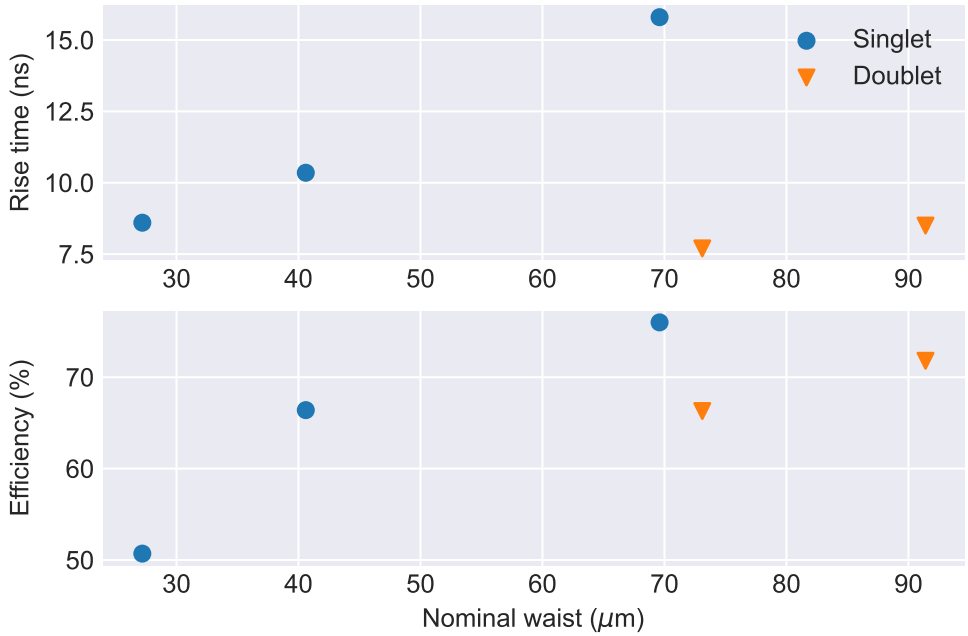


Figure 4.3: Plot showing the 10-90% rise time and efficiency of a Brimrose TEFM-200-100-689 AOM for different beam waists through changing the focusing lens and the ingoing waist. The two rightmost data points are for achromatic doublet lenses.

Even with the tightest waist in the AOM crystal, the rise time is only as fast as the rise time of the driving RF. The solid-state ZASWA-2-50DRA+ is the fastest packaged RF switch sold by Minicircuits and is found to switch marginally faster than the integrated RF switches on the ARTIQ Urukul channels. The 200 MHz RF driving each AOM is supplied by amplified Urukul channels, with the switch being controlled by ARTIQ TTL outputs.

4.1.3 Performance

Figure 4.4 shows the shortest achievable pulses with the two sequential AOMs. Both AOMs are driven by the shortest pulses found to reach full amplitude as measured by the photodiode, a triggering pulse of width 16.8 ns. Each AOM is pulsed every 60 ns, resulting in a combined pulse repetition rate of 33.3 MHz. This is faster than any commercially available pulse-shaping technology, to the author's knowledge. This is the fastest repetition rate possible before the pulses begin to overlap, requiring careful adjustment of the relative timing of the driving pulses. The bumps between pulses are artefacts of the amplified photodiode measurement, they do not manifest in a loss in intensity of the reciprocal AOM pulse.

The first-order diffraction efficiencies of the two AOMs are 62% and 59% for the first and second AOM respectively, and the fibre-couple efficiency is better than 90% for both paths. A π-time of 30 ns corresponds approximately to the fifth darkest contour in figure 4.1. For a typical 200 μm cloud and 2 mm waist, satisfying the 10:1 beam-to-cloud ratio guideline, a power of 1-1.5 W is required at the atoms to achieve the 30 ns π-time. This requires a maximum laser power exceeding 2 W, above what the Ti:Sapph can deliver since the maximum output

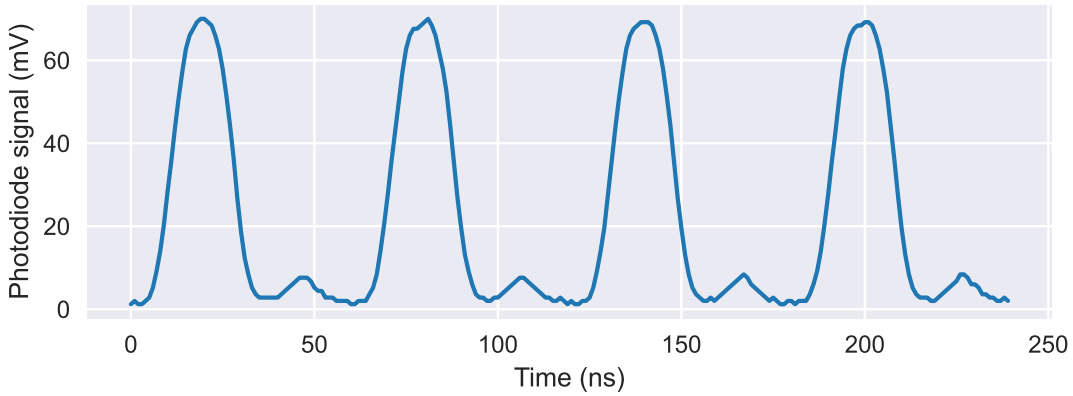


Figure 4.4: Photodiode signal for pulses shaped by one of the two AOMs. Pulses of width 16.8 ns drive both AOMs alternatingly at a repetition rate of 16.7 MHz. The repetition rate of the pulses from both AOMs is 33.3 MHz.

power has fallen from the specified 2.5 W to < 1.5 W. If the radial waist of the cloud could be reduced to 100 μm then the same π-time could be implemented using just 250 mW of optical power in a 1 mm waist beam. The current laser system can deliver these powers, even using generic Thorlabs fibres limited to 300 mW.

The efforts here focus on achieving the largest momentum separation in an atom interferometer whilst maintaining fringe visibility. Realising the most sensitive measurements will require an analysis of the optimum number of LMT pulses, taking into consideration spontaneous emission and pulse fidelity. Applying many successive π-pulses in an LMT sequence compounds the effects of imperfect pulse fidelity and can quickly diminish fringe contrast. One also has to consider whether a pulse can still efficiently drive a π-transition in two arms once they are separated in momentum by the $n\hbar k$. Pulse fidelity decreases as successive momentum recoils increase the detuning between the laser and atoms, and compensating techniques such as floquet or composite pulses have longer durations leading to increased

spontaneous emission losses [57, 64–67].

4.2 Atom interferometry laser

In this experiment, atom interferometry will be conducted using vertical beams in a setup sensitive to gravitational acceleration. Unlike other orientations, this approach ensures atoms remain within the beams even when extending the T-time of the sequence. The diameter of the beams should be large compared to that of the atom cloud to minimise the effects of dephasing. Flat optical wavefronts are desired to reduce phase errors in the interferometer, this means selecting optics with the best optical flatness and minimising the number of surfaces. The design should be efficient in terms of optical power such that sufficiently high intensities can be produced at the atoms in order to drive short π-times. Other sources of phase noise include mechanical vibrations of the beam delivery optics relative to the atoms, and pointing instability of the two laser beams.

Performing atom interferometry demands specific intrinsic performance of the interrogation laser. Due to the high pulse bandwidth of short pulses, effective detuning introduced by frequency noise is less of an issue for fidelity, provided the laser linewidth is narrow compared to pulse bandwidth. However, phase and frequency noise will couple into the measured AI phase, so should be kept below the level of the signal of interest in general. Intensity noise can affect the area of an atom optic pulse, such that it doesn't precisely enact the intended operation, limiting pulse fidelity. Thus, the intensity noise of the laser must also be bounded.

4.2.1 Design

All 689 nm light for addressing the $^1S_0 - {}^3P_1$ transition in this experiment is derived from a single Ti:Sapph laser. The design of the non-interferometry paths is described in section 3.3.2. A Pockels cell between orthogonal polarising beam splitter cubes forms an optical switch. Applying the half-wave voltage of the crystal results in a rotation of the light's polarisation axis such that the intensity on the reflected PBS port goes from a minimum to a maximum. The switch allows dynamic optical power allocation to both the red 3D MOT cooling path and Rabi scan path, and the atom interferometry path. As a result, a single 689 nm laser can fulfil all purposes without reducing the power available for interferometry, which would place a floor on attainable π-times. Compared to a variable retarder plate, a Pockels cell offers faster switching times and reduced susceptibility to thermal drifts.

The power handling capacity of optical fibres can constrain the maximum power transmitted between the optical table and the experiment. As an illustration, standard single-mode fibre patch cables from Thorlabs can accommodate up to approximately 300 mW at 689 nm. By situating the pulse-shaping AOMs pre-fibre, the full $\sim$300 mW can be delivered to the atoms as opposed to having that power reduced by downstream AOM inefficiencies. Using short 2 m patch cables with pulsed light, it is anticipated that issues from stimulated Brillouin scattering can be avoided. Mode-matching telescopes for both fibre inputs improve coupling efficiency to approximately 90%. Replacement of the current generic fibres with high-power fibres should enable the coupling of higher powers to the experiment in the future.

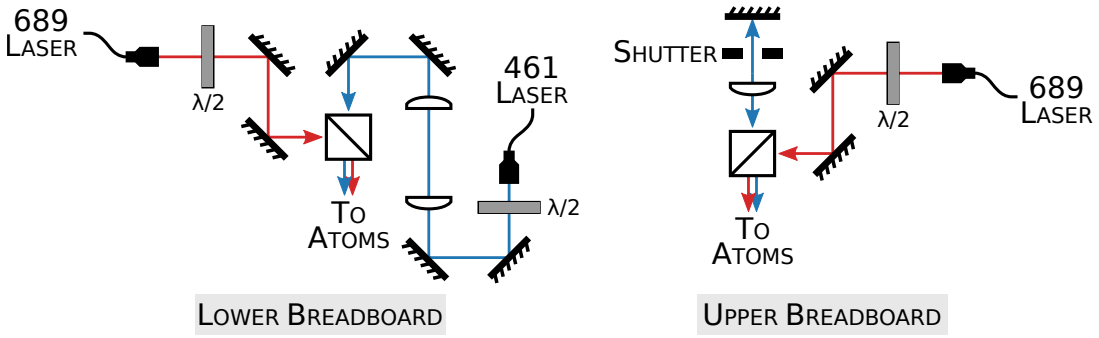


Figure 4.5: Design of the delivery optics for the atom interferometry and detection beams. Light at 461 nm and 689 nm is overlapped using PBSs. The 461 nm light is delivered in fibre on the lower breadboard and retroreflected on the upper breadboard. The retroreflecting 461 nm path on the upper breadboard uses a shutter to allow for both balanced light for detection, as well as unbalanced light for pushing the atoms or blow-away pulses. A 5× telescope expands the blue beam to a waist of 7.5 mm.

The interrogation light is delivered from above and below the chamber in the configuration shown in figure 4.5. Polarising beam splitters serve a dual purpose, filtering the polarisation of the atom interferometry light and overlapping the 689 nm light with the 461 nm light used for detection. This avoids the need to use a separate polariser and dichroic mirror. The interferometry light is incident on the reflected port of each PBS for improved wavefront flatness and polarisation extinction ratio. On both the top and the bottom breadboard, a mirror at 45^o to the horizontal plane directs the two wavelengths of light onto the vertical axis intersecting the atoms. The optics are arranged such that the polarisation of the light is parallel to the axis of the MOT coils. Polarising the atom interferometry light in this way means that the MOT coils or compensation coils can apply a bias field to selectively drive the $\Delta m_J = 0$ transition, suppressing transitions to the other m_J levels.

4.2.2 Performance

As described in section 3.4, feedback for the 689 nm Ti:Sapph laser is applied using the fast piezo input with a specified servo bandwidth of 50 kHz. This limits the loop bandwidth which could be improved by instead applying feedback using a dedicated AOM. Nonetheless, this approach is preferred here because it doesn't compromise available optical power and for the reduced complexity of the optical setup. The PIID gains are optimised by reducing the amplitude of the peaks and overall noise floor in the residual error frequency spectrum shown in figure 4.6. The prominent peak in the error signal spectrum is due to the Ti:Sapph etalon lock dither frequency at 19.2 kHz. This is reduced by lowering the amplitude of the dither or nulled by temporarily holding the etalon dither using a TTL input on the laser controller.

The frequency performance of the locked laser is characterised by performing an optical beat note measurement against another laser at the same wavelength. The AION lab at the University of Birmingham fortunately shares a lobby with the iqClock lab, a strontium optical lattice clock project [135]. A fibre connection between the labs facilitates comparisons between the lasers. The frequency difference between the two lasers is set to approximately 80 MHz, and light from both lasers is overlapped onto a fast photodiode. By fitting the Lorentzian lineshape to the beat note signal in figure 4.7, a 3 dB linewidth of 100 Hz is measured, limited by the 100 Hz resolution bandwidth of the spectrum analyser. Figure 4.8 shows the peak frequency from a spectrogram of the beat note, over $\sim$1 min. Frequency excursions from the mean are bounded within $\pm$ 75 Hz. The short-term linewidth and longer-term frequency drift are much less than the $2\pi\times$ 7.5 kHz of the ${}^1S_0 - {}^3P_1$

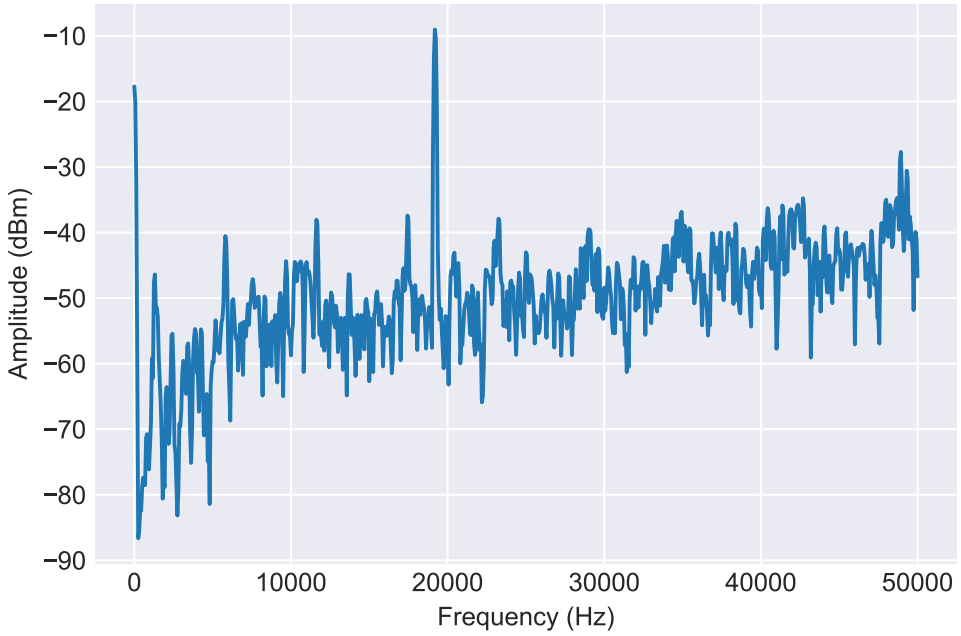


Figure 4.6: Residual error signal from Pound-Drever Hall lock. The peak at 19.2 kHz is due to the Ti:Sapph etalon lock dither.

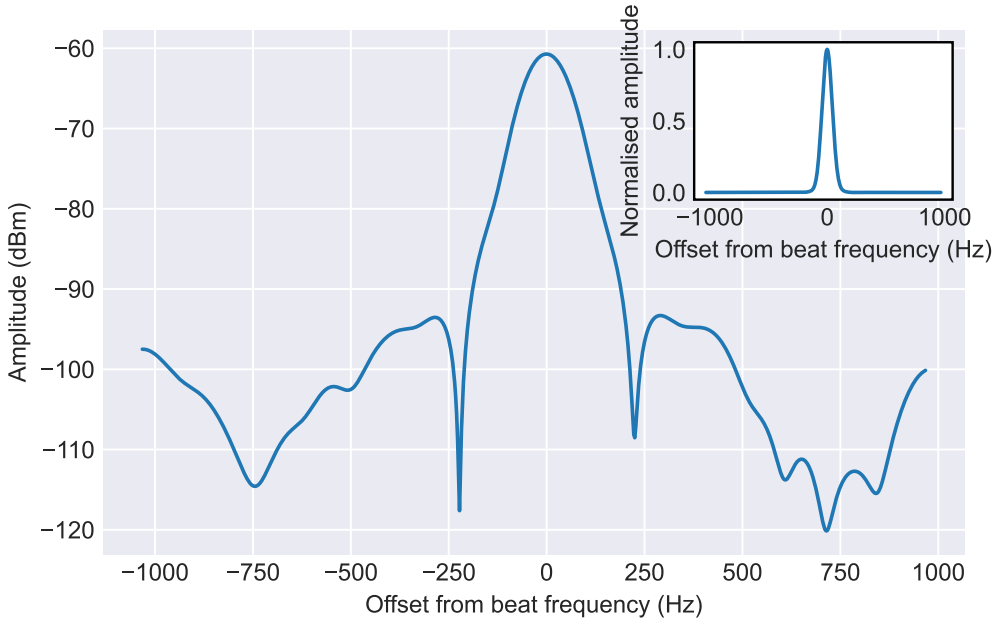


Figure 4.7: Typical beat note trace between the AION and iqClock 689 nm lasers. The laser exhibits a 3 dB linewidth of 100 Hz, limited by the resolution bandwidth of 100 Hz. Inset: The same signal but with a linear axis for amplitude, showing the Lorentzian lineshape of the beat note.

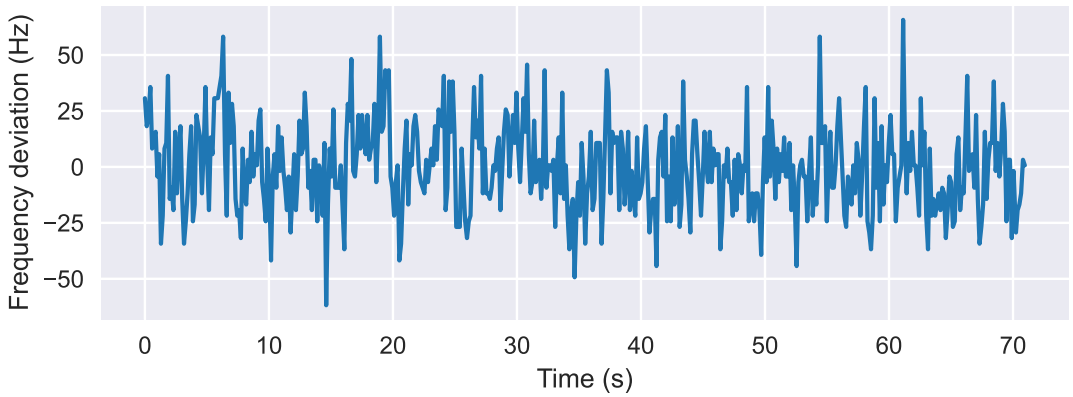


Figure 4.8: Spectrogram centre frequency of the beat note between the AION and iqClock 689 nm lasers.

transition by a factor of 10-100.

4.2.3 Alignment

Vertical and counter-parallel alignment of the two interrogation beams should be ensured. Aligning the beams vertically will allow measurements of local gravity. Improper pointing will lead to phase errors. Vertical alignment is also important when scaling interrogation times such that gravity does not cause the atoms to fall axially out of the beams, causing dephasing. Counter-parallel alignment is necessary because off-axis components of the recoil kicks could move the atoms out of the reciprocal beam over many pulses. Each photon recoil imparts a velocity kick of roughly 7 mm s^{-1}, and the issue is compounded for many pulses and longer interrogation times.

To align the beams, the following alignment protocol can be followed. The down-propagating beam is retroreflected by a liquid or floating mirror and aligned such that it couples back into the same fibre, ensuring the beam is vertical. It should also axially intersect the centre of the red MOT, and this can be verified by imaging the atom cloud following a π-pulse to examine the spatial dependence of the pulse. Once this beam is both vertical and aligned to the atoms, the up-propagating light can be aligned into the down-propagating fibre coupler. This ensures the two beams are counter-parallel. Light returning to the laser due to propagation between fibres is minimized, as only one AOM will be driven at any given time.

4.3 Pulses for long-baseline atom interferometry

The research presented in this thesis is largely geared towards performing atom interferometry on the $^1S_0 - {}^3P_1$ intercombination transition in strontium. Whilst this transition is interesting for large momentum transfer due to the short pulses it supports, the lifetime becomes an issue when scaling to long-baseline atom interferometer gradiometers. As the baseline increases, the propagation time for a pulse to travel the baseline becomes consequential. For sequentially counter-propagating pulses, a given pulse must pass through both atom interferometers before the next pulse can be delivered. For a 100 m baseline, the propagation time exceeds 300 ns, limiting the achievable pulse repetition rate and the number of pulses that can be applied as constrained by spontaneous emission. This motivates using a longer-lived single-photon transition, such as the $^1S_0 - {}^3P_0$ clock transition in ^{87}Sr.

The clock transition has a lifetime of 118 s. This far exceeds achievable measurement times, which are instead limited by the available free-fall distance or finite temperature cloud expansion. Spontaneous emission-related decoherence is, therefore, virtually negligible. The narrow linewidth and weak coupling of the transition introduce different technical challenges. In later stages of AION, momentum separations of $10^4\ \hbar k$ are targeted with interrogation times of approximately one second. Completing the requisite number of pulses in a fraction of the interrogation time requires pulses of order 1-10 μs, but due to the weak coupling, this demands intensities of $\sim$20 kW cm^{-2}. To achieve this intensity in a beam of waist sufficiently large compared to the atomic cloud would require laser powers of several kW, well beyond the capabilities of available lasers. This will be one of the

biggest technical challenges in scaling to large LMT over long baselines.

A method for overcoming the prohibitive power requirements is proposed in a paper co-authored by the author of this thesis [136]. The proposed scheme employs resonant enhancement of spatially-resolved pulses within a travelling-wave cavity of 1 km baseline and 6 km round trip path length. A schematic diagram of the cavity is shown in figure 4.9. Counterpropagating pulses are periodically coupled into the cavity off-resonance, and an intracavity Pockels cell is used to shift the pulses of light onto resonance to deliver π and $\pi/2$ pulses, using Serrodyne modulation. This modulation is also used to track the Doppler shifts of the atoms as they recoil from the applied pulses. For the given cavity, the minimum beam radius at the atoms is 15 mm, as governed by the dynamics of Gaussian beam propagation. The circulating intensity in steady-state is enhanced relative to the input intensity by $I_{circ} = (\mathcal{F}/\pi)I_{in}$. Assuming a cavity finesse of 4000, a 20 kW cm^{-2} intensity can be achieved with an input power of only 16 W, despite the large mode size.

For shorter baseline experiments such as AION-10, optical cavity enhancement could still play an important role. On the $^1S_0 - {}^3P_0$ clock transition in ^{87}Sr, it would not be possible to couple spatially-resolved π-pulses for an atom interferometer on this baseline. However, because of the narrow transition linewidth, the circulating light field would be resonant with the atoms in just one direction. An in-cavity atom interferometry experiment would stand to benefit from power enhancement and spatial mode filtering. There are two primary challenges associated with cavity-enhanced atom interferometry, though. Firstly, a beam-to-cloud size ratio of 10:1 is desired from contrast considerations, but it is difficult to achieve a large spatial mode in a geometrically stable cavity. Secondly, the cavity resonance must track the Doppler-shifted transition frequency during freefall, the sign

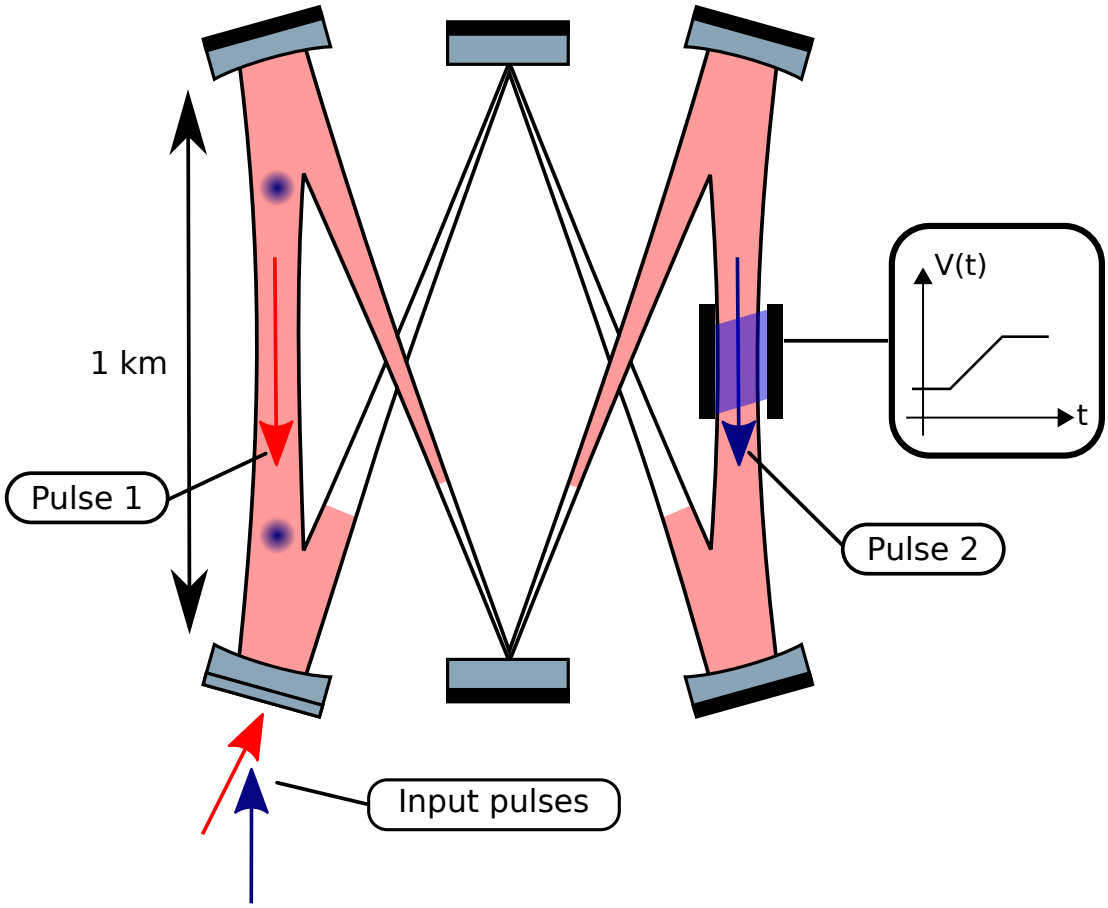


Figure 4.9: Two circulating pulses counterpropagating in a 1 km baseline cavity of 6 km round trip length. Serrodyne modulation from linear voltage ramps applied to a Pockels cell tune the frequencies of the pulses. The figure also appears in the paper [136].

of which is opposite for upgoing and downgoing light. The author of this thesis also contributed to a paper demonstrating techniques to overcome these limitations [137]. An intracavity telescope is used to magnify the spatial mode, and an intracavity Pockels cell enables tracking of the resonant atomic frequencies. For further details, the reader is referred to the thesis of Rustin Nourshargh [138].

The circulating pulse technique overcomes the pulse bandwidth limit for cavity finesses outlined by Alvarez et al., associated with the cavity build-up and ring-down pulse elongation [139, 140]. It also confers the benefit of spatial mode filtering inherent to cavities. This would be the purview of a facility-scale experiment and would clearly be challenging to implement. It is, however, the first practicable approach to delivering on the pulse requirements of the AION projects. The scheme for large-mode cavity enhancement with frequency tracking could stand to benefit the generation of 10 m detectors currently in construction.

4.4 Summary

In this chapter, the design is presented for the atom interferometry laser system. The system is capable of driving 30 ns pulses at 30 MHz repetition rates to meet the needs of large momentum transfer pulses on the intercombination line. A Pockels cell acting as an optical switch allows the same Ti:Sapph laser to fulfil the requirements in second-stage cooling without compromising optical power during atom interferometry. Beyond the pulse-shaping capabilities, the laser's linewidth is characterised and found to be better than 100 Hz. The performance of the laser system is further validated in chapter 5, producing red MOTs and demonstrating atom interferometry fringes.

The chapter concludes with a discussion of a proposal for meeting demanding optical power requirements in future long-baseline atom interferometers.

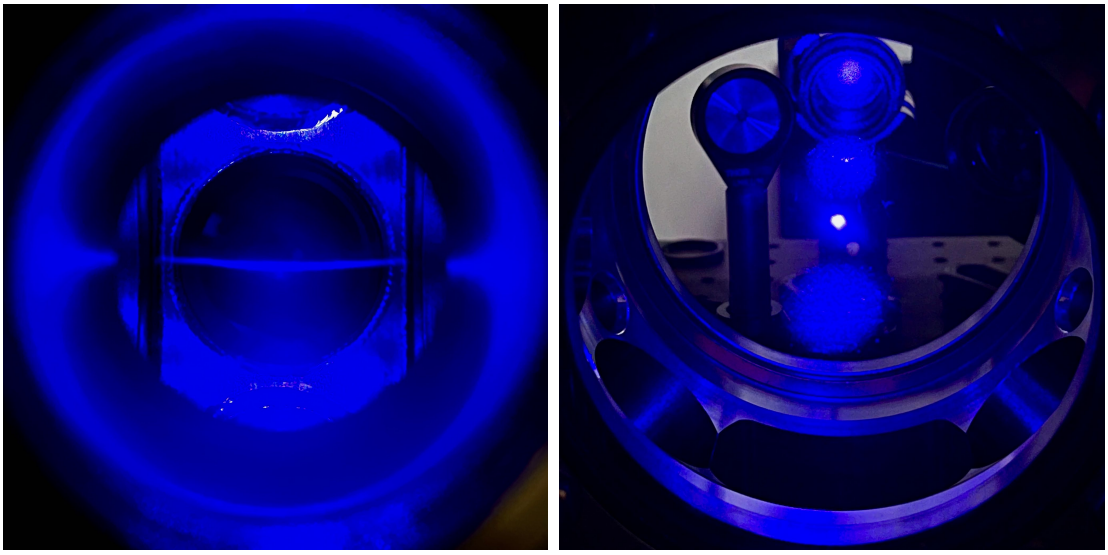
Chapter 5

Strontium atom interferometry

This chapter details the progress in building a strontium atom interferometer for future research into improving contrast and fidelity for extremely large momentum transfer. It validates the design and performance of the various subsystems, including the laser, timing, detection and vacuum systems.

5.1 Cold atoms

Samples of cold atoms form the wave packets with which light pulse-atom interferometry is performed. Temperatures as cold as possible are desired to mitigate against dephasing, as well as the fidelity loss described in section 2.1.8. In this experiment, strontium atoms are cooled from a thermal beam to microkelvin temperatures using a 2D MOT followed by two-stage cooling.



(a) 2D MOT (b) Blue 3D MOT

Figure 5.1: (a): The 2D MOT in Chamber One on the 461 nm ${}^1S_0 - {}^1P_1$ transition. (b): The blue 3D MOT in Chamber Two on the same transition.

5.1.1 Blue MOT

Cooling and trapping in the first stage of the two-stage process is achieved using 461 nm light addressing the ${}^1S_0 - {}^1P_1$ transition. Atoms enter Chamber One from the atomic oven with ballistic velocities at temperatures exceeding 400^{o}C. They are first slowed and confined along an axis by the 2D MOT, as shown in figure 5.1a. A push beam sends atoms from the 2D MOT to the 3D MOT, shown in figure 5.1b, passing through the differential pumping aperture. The relevant detunings and powers are presented in section 3.3.

To achieve the highest blue MOT atom number, it is essential to repump dark state atoms lost via the parasitic ${}^1P_1 - {}^1D_2$ transition. Figure 5.2 shows the effect of applying repump light whilst loading the blue 3D MOT. 2 mW of 679 nm light and 2 mW of 707 nm light, co-propagating in a 3.4 mm radial waist beam, is delivered along the axis connecting the 2D and 3D MOT in the opposite direction to the

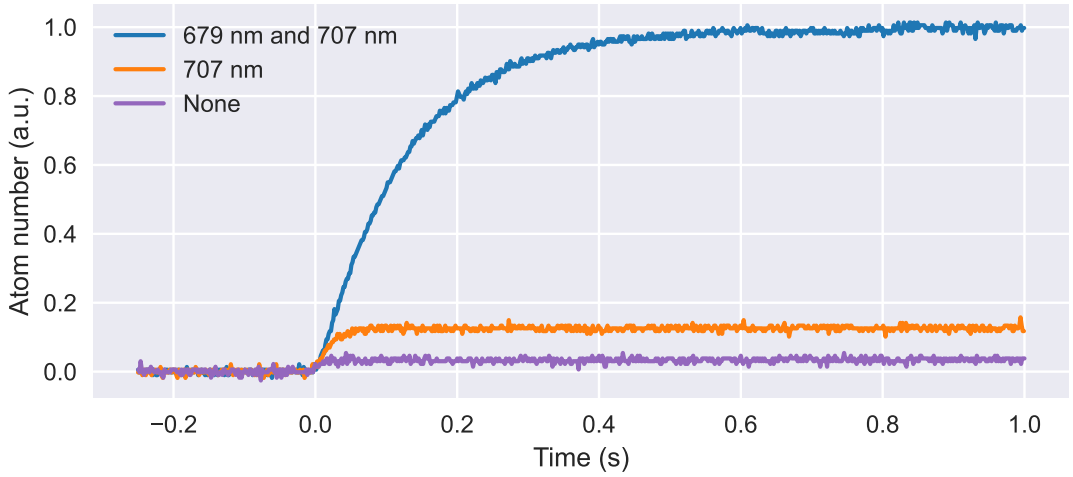


Figure 5.2: Blue 3D MOT loading curve photodiode signal taken for different repump configurations. Using 707 nm or 679 nm and 707 nm yields roughly an eight-fold or 28-fold improvement, respectively, compared to the non-repumped case. The background photodiode signal is subtracted in each case.

push beam. Applying 707 nm light alone increases the atom number by $\sim 8\times$ but a portion of atoms are lost from the cooling cycle to the dark $^3P_0$ state via $^3S_1$. 679 nm light pumps the atoms from this state, returning them to the cooling cycle. Using both wavelengths increases the MOT atom number by $\sim 28\times$. It is found that applying the repump light along the push axis increases the MOT number by $\sim 2\times$, compared to inputting the light through the large DN100CF viewport. This is likely because the pushing light causes some fraction of the transported atoms to fall into the $^3P_2$ state, and those atoms would pass through the 3D MOT region in the absence of repump light.

5.1.2 Red MOT

This section contains the characterisation of the red MOT as well as the optimisations leading to the system parameters at the time of writing. Figure 5.3 illustrates

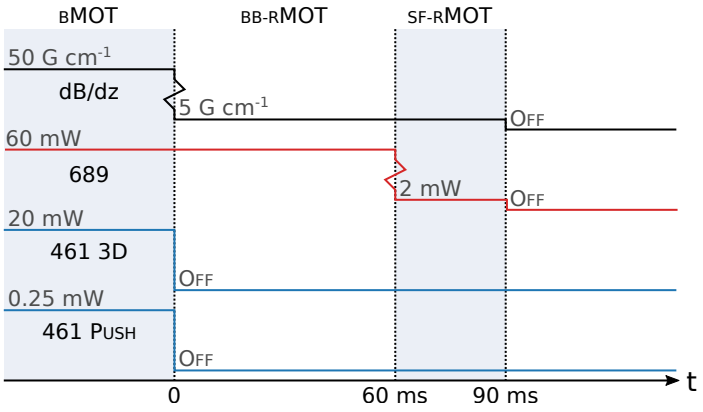


Figure 5.3: Timing sequence for the red MOT. The frequency-broadened red MOT (bb-rMOT) begins at t = 0, at the end of the blue MOT (bMOT), lasting for 60 ms. After 60 ms the frequency modulation of the 689 nm light is stopped and the optical power is stepped down for the single-frequency red MOT (sf-rMOT) which lasts 30 ms. The 2D MOT light and repump light are found not to affect the red MOT and so are left on continuously.

the timing of the light and magnetic field during the red MOT sequence. The current sequence is quite basic, and it is anticipated that implementing an intensity ramp and magnetic field compression at the end of the broadband red MOT will yield reduced cloud temperatures and sizes.

A slightly counterintuitive finding is that the greatest blue MOT atom number generally doesn't yield the greatest red MOT atom number. This is illustrated in figure 5.4 where the peak red MOT atom number is achieved with approximately 3 to 4× lower intensity than the peak blue MOT value. This is likely because a reduced light intensity during the blue MOT leads to a colder or more dense sample and, hence, more efficient transfer from the blue to red MOT. The duration of the blue MOT is 1 s, allowing the atom number to reach steady state. Applying 689 nm red MOT light continuously during the blue MOT is found to improve the transfer efficiency into the frequency-broadened red MOT. This is consistent with

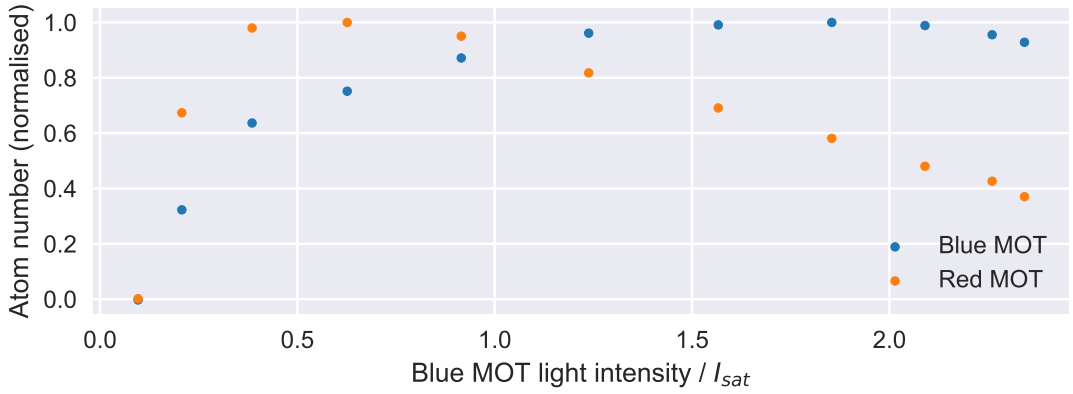


Figure 5.4: Red MOT and blue MOT atom number as a function of blue MOT light intensity. The peak atom numbers are 2×10^7 and 8×10^6 atoms for the blue and red MOT, respectively.

the recently published findings of Höschele et al. [141].

To address a broader velocity class of atoms from the relatively hot 3D blue MOT and transfer a greater fraction of atoms to the red MOT, the red MOT light is intentionally frequency broadened at first. The RF driving the red MOT AOM is frequency-modulated using a sawtooth waveform over 4 MHz at a rate of 130 kHz, starting 120 kHz below resonance. This frequency modulation in the time domain creates a comb in the frequency domain whose teeth effectively address the resultant velocity classes from the blue MOT. Figure 5.5 shows that the optimal detuning of the ramp centre frequency is approximately half the ramp span. When the ramp centre is closer to resonance than this, some comb teeth are blue-detuned, diminishing the restoring force of the trap.

Following the frequency-broadened red MOT, the frequency modulation is switched off, and the total power is stepped from 60 mW to 2 mW. Scanning the detuning of the non-frequency-broadened red MOT light reveals an interesting spectrum. Figure 5.6 shows how a sharp peak at $\Delta = -2\Gamma$ is surrounded

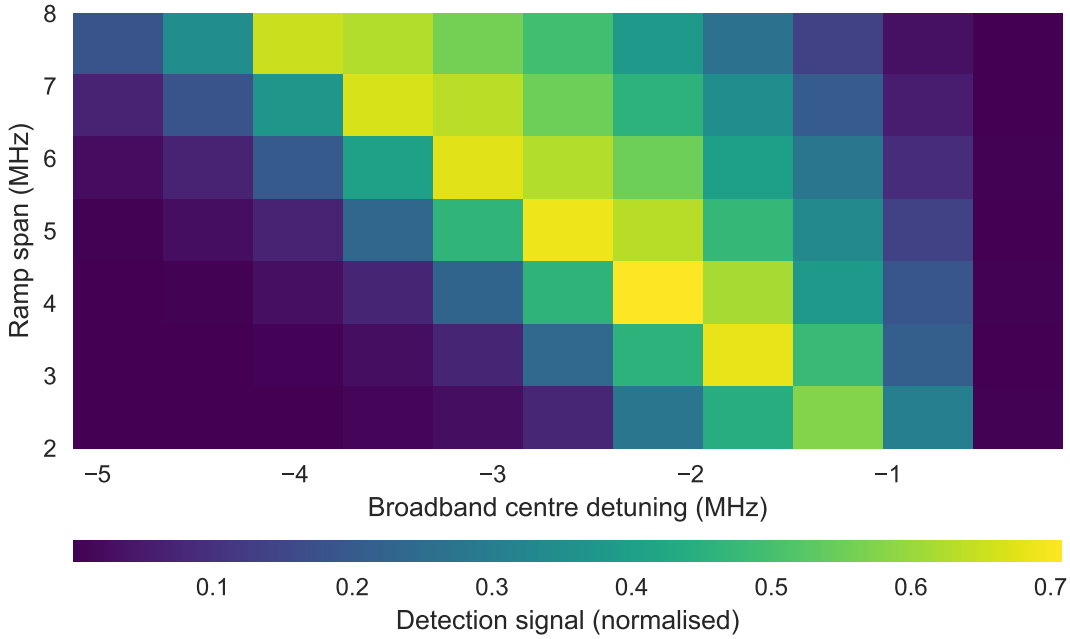


Figure 5.5: Red MOT signal, as a function of centre frequency and span of the frequency-broadened red MOT light. The fluorescence signal during the detection 461 nm pulse post red MOT is normalised against the fluorescence signal during the blue MOT.

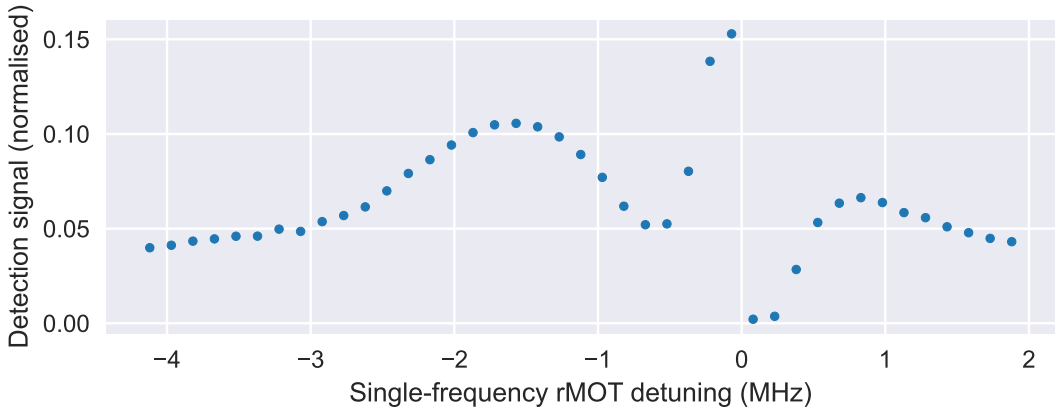
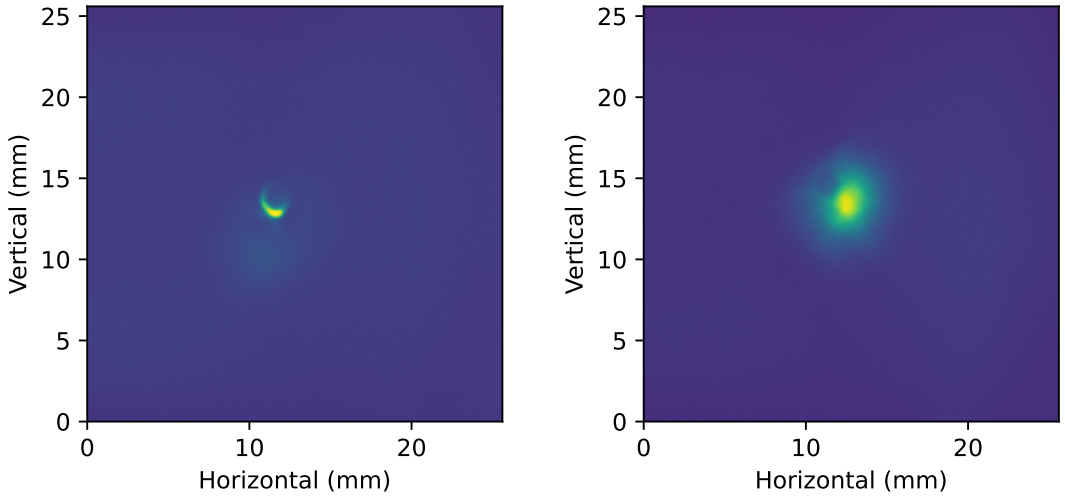


Figure 5.6: Detection signal as a function of detuning of the single-frequency red MOT light from resonance. Measured 1 ms after the red MOT light switches off. The peak is at $\Delta = -2\Gamma$ or ~ -50 kHz. The fluorescence signal during the detection 461 nm pulse following the red MOT is normalised against the fluorescence signal during the blue MOT.

by broader bumps below and above resonance. A narrow-line red MOT can be observed for detunings of roughly -100 kHz to - 1 MHz. The narrow-line MOT is typified by the way atoms sag under gravity to a position where the laser detuning balances the Zeeman shift. An example image is shown in figure 5.7a. The radius of the shell into which the atoms relax increases with detuning. The horizontal asymmetry seen is suspected to be the result of a slight power imbalance between, or misalignment of, the two radial beams. Figure 5.7b shows the sample corresponding to the peak in figure 5.6. By using a blue detuning of order 100 kHz it is also possible to observe momentum-space crystals as described by Loftus et al. [103].

Time-of-flight data for the expansion of the atoms following the red MOT are shown in figure 5.8. Each data point in the time series corresponds to an image taken with the EMCCD camera, and the intensity profile is fit to a 2D Gaussian to



(a) -500 kHz (b) -50 kHz

Figure 5.7: Atom cloud fluorescence images 1 ms after the single-frequency red MOT end. (a): Shows the narrow-line red MOT at -500 kHz detuning, typified by the shape with atoms sagging under gravity. (b): Resultant atom sample following the single-frequency light phase at -50 kHz detuning, corresponding to the peak in figure 5.6.

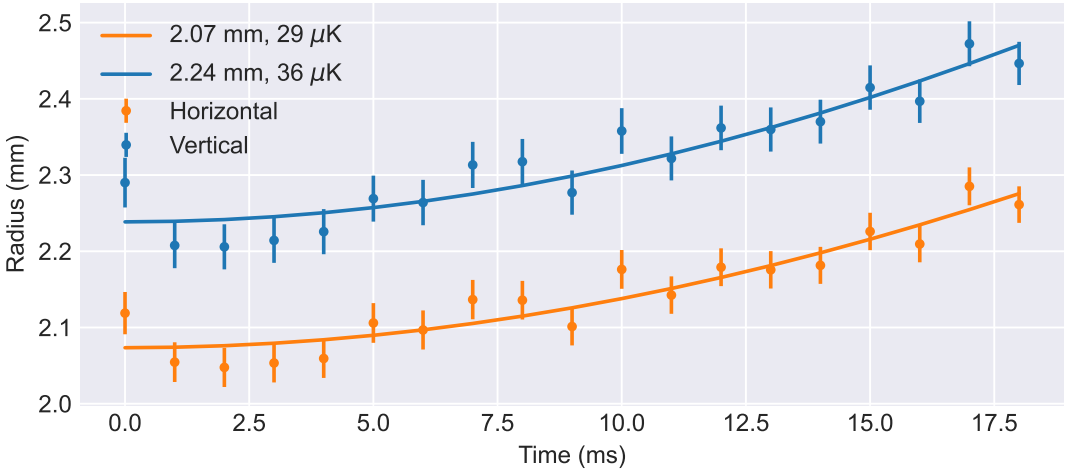


Figure 5.8: Time-of-flight expansion following the red MOT, with the horizontal and vertical $1/e^2$ radii from 2D Gaussian fitting for each image in the time series. The solid lines correspond to the fitted parameters. The fitted horizontal and vertical temperatures are (29 ± 3) μK and (36 ± 3) μK, respectively.

extract the horizontal and vertical $1/e^2$ radii. The initial radius σ_0 and temperature T are extracted by fitting to the equation for cloud radius as a function of time

$$\sigma^2(t) = \sigma_0^2 + \frac{k_B T}{m} t^2 \tag{5.1}$$

where k_B is the Boltzmann constant and m the mass of an atom. From fitting to this equation, horizontal and vertical temperatures of (29 ± 3) μK and (36 ± 3) μK are extracted, respectively. The horizontal and vertical waists are 2.07 mm and 2.24 mm, respectively.

Figure 5.9 shows the decay of atoms from the frequency-broadened red MOT as a function of time. The time constant of the decay τ is extracted by fitting the atom number $N(t)$ with the equation for exponential decay

$$N(t) = N_0 e^{-t/\tau} + c. \tag{5.2}$$

Here N_0 is the initial population, τ is the trap lifetime and c accounts for the background signal. The time constant is (227 ± 2) ms.

5.1.3 Magnetic trap

It is possible to magnetically trap strontium atoms in the metastable $^3P_2$ state [142, 143]. Population of this state occurs during operation of the blue MOT, via the parasitic $^1P_1 \rightarrow {}^1D_2 \rightarrow {}^3P_2$ decay path shown in figure 2.8. During typical operation of the blue MOT, these atoms are brought back into the cooling cycle using repump light at 679 nm and 707 nm. The magnetic trap can be loaded by running the blue MOT in the absence of repump light, as the magnetic trap is

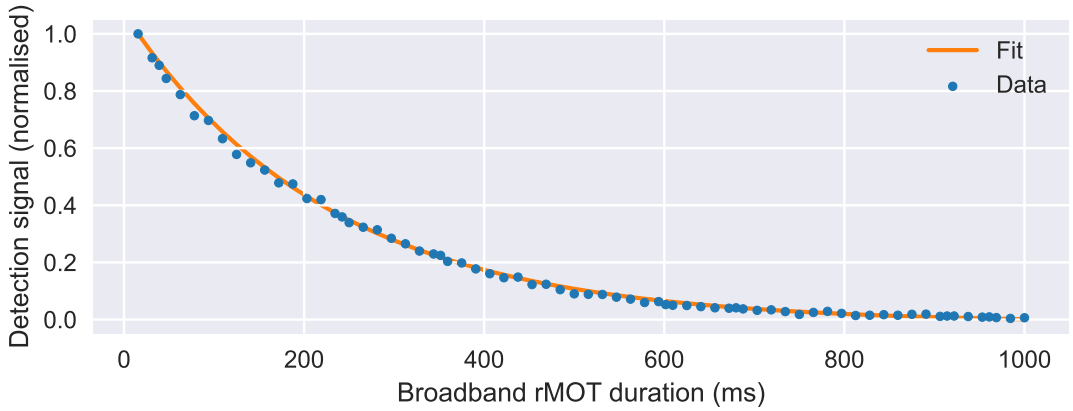


Figure 5.9: Lifetime measurement of the frequency-broadened red MOT.

generated by the same quadrupole field required during the blue MOT. Continuous outcoupling from the magnetic trap offers interesting prospects for zero-deadtime atom interferometers and optical atomic clocks [144].

Nagel et al. found that the magnetic lifetime for ^{88}Sr is limited by collisions with background atoms rather than Sr-Sr collisions and that the vacuum pressure can be inferred from the lifetime [143]. The magnetic trap population as a function of hold time is described by equation 5.2. A delay following the end of the blue MOT is used sufficient such that the relatively warm blue MOT atoms have dissipated and are not counted during detection. By fitting the decay in figure 5.10 to this equation, a lifetime of (17.7 ± 0.4) s is extracted. This far exceeds any drop time possible in the experiment vacuum chamber and also exceeds the timescales associated with evaporative cooling, as discussed in section 3.1.4. This lifetime infers a vacuum pressure of 1.66×10^{-10} mbar.

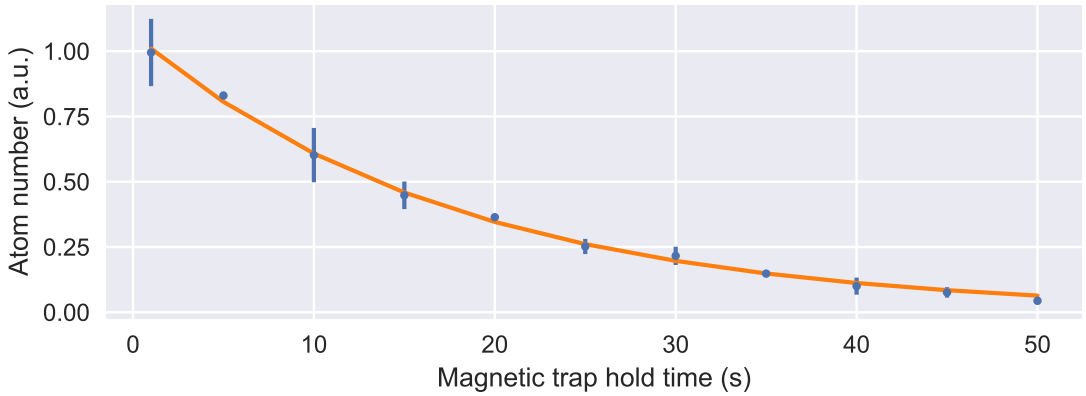


Figure 5.10: Population of the magnetically trapped $^3P_2$ state as a function of time. The fitted lifetime is (17.7 ± 0.4) s. The data are kindly provided by Oliver Ennis and Ben Stray.

5.2 Detection

Characterisation and optimisation of the cold atoms samples require knowledge of the atom number or at least some metric that is proportional to the atom number. Moreover, performing Rabi scans and atom interferometry demands knowledge of the state populations. Currently, the detection photodiode signal is used to infer atom number. The EMCCD is used to make qualitative assessments of the atom clouds but will ultimately be integrated with ARTIQ to perform real-time analyses such as two-state detection and time-of-flight.

The number of atoms in a sample can be calculated from the total rate of scattered photons R_γ and the estimated photon scattering rate for a single atom R_{sc}. When counting the photons using a photodiode, the number of scattered photons is related to the measured photodiode voltage V, by

$$R_\gamma = \frac{V}{\mathcal{R}G} \cdot \frac{1}{hf} \cdot \frac{1}{\Omega/4\pi} \tag{5.3}$$

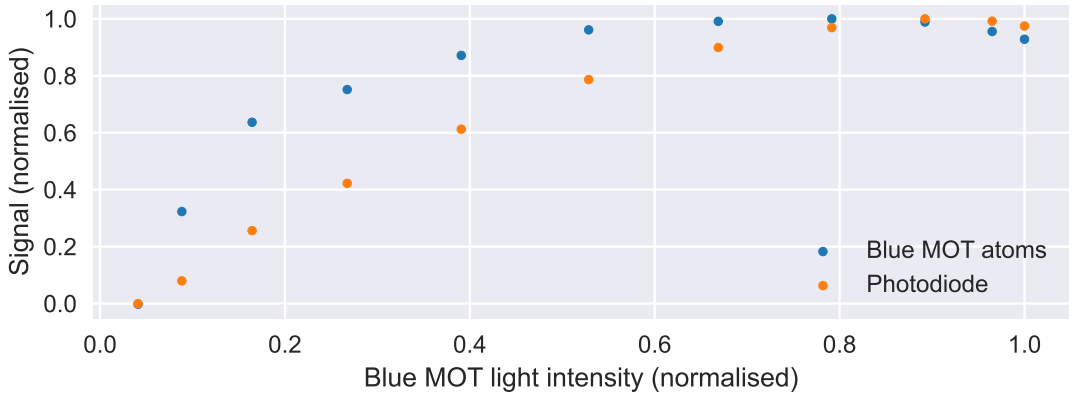


Figure 5.11: The photodiode signal and corresponding calculated blue MOT atom number as a function of blue MOT light intensity.

where $\mathcal{R}$ is the photodiode responsivity at the relevant wavelength, G is the gain, hf is the energy of a single photon of frequency f and $\Omega/4\pi$ is the solid angle fraction of the detection setup. The photon scattering rate is given by

$$R_{sc} = \frac{\Gamma}{2} \frac{I/I_s}{1 + I/I_s + 4(\Delta/\Gamma)^2} \tag{5.4}$$

where Γ is the linewidth of the transition, I is the combined intensity of the detection beams, I_s is the saturation parameter, and Δ is the detuning of the detection light from resonance [77]. The number of atoms is then

$$N_A = \frac{R_\gamma}{R_{sc}}. \tag{5.5}$$

Throughout this chapter, the photodiode signal during fluorescence detection pulses is often used as a proxy for atom number since N_A scales in V. The number of atoms in the blue MOT can also be estimated based on equation 5.5 from the MOT fluorescence itself. Care must be taken when scanning the blue MOT

parameters, though, as the highest photodiode signal is not necessarily indicative of the highest atom number, demonstrated in figure 5.11. In scans of the red MOT parameters, the photodiode signal is typically normalised against the photodiode signal during the blue MOT, accounting for blue MOT atom number fluctuations.

The blue MOT beams are currently used to provide the detection light, with the frequency set to resonance in the absence of any applied magnetic field. To find the resonance of the ${}^1S_0 - {}^1P_1$ transition, the frequency of a detection pulse following the red MOT is scanned, as in figure 5.12. Per equation 5.4, the maximum scattering rate, and hence recorded intensity, occurs for resonant light ($\Delta = 0$). The cold sample temperature resulting from the red MOT minimises Doppler effects and should provide a reliable estimate of the resonant frequency. This frequency is measured by the wavemeter as 650.503825 THz, which disagrees with the NIST value of 650.5035 THz [94] but is closer to the value reported by Stellmer et al. of 650.3775 THz [145]. At 689 nm the wavemeter agrees with the ${}^1S_0 - {}^3P_1$ transition frequency to better than 1 MHz, but the wavemeter may be less accurate at shorter wavelengths. Due to the width of the MOT beams, the maximum time-of-flight times are limited to around 20 ms. The detection setup is being upgraded to use dedicated vertical beams as described in section 3.5.2 to overcome this.

Performing state detection after an atom interferometry sequence requires that the two atomic states can be resolved. With balanced MOT beams, it is not possible to push the two populations apart, but it is possible to blow away ground-state atoms. To test the blow-away pulse, a red MOT is loaded and then dropped, and the atoms are allowed to relax into the ground state over 1 ms. Figure 5.13 shows that the largest fraction of atoms is blown away for a blue detuning of 7 MHz. A blue detuning is likely optimal as the light is resonant with atoms moving

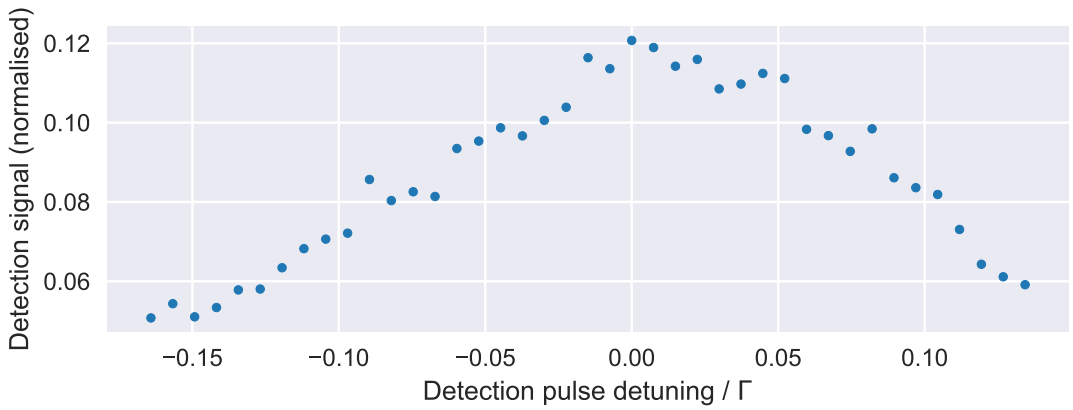


Figure 5.12: Detection signal following the red MOT, as a function of the detuning of the detection light frequency. The signal is normalised against the photodiode signal during the 3D blue MOT. The noise is predominantly due to shot-to-shot variation in atom number.

away from each laser. Again, by moving to an unbalanced beam as laid out in section 3.5.2, the efficiency of the blow-away pulse should be improved.

5.3 Atom optics

The atom interferometry sequence relies upon atom optics, π and $\pi/2$-pulses, which carry out the required state transfer operations. These pulses are introduced in section 2.1.1 and are the same whether performing a simple three-pulse Mach-Zehnder sequence or an LMT sequence with many pulses. To determine the Rabi frequency and pulse durations, Rabi scans are performed.

5.3.1 Rabi scan

Achieving maximum contrast in atom interferometry when addressing a single-photon transition requires the laser frequency to be resonant with the transition.

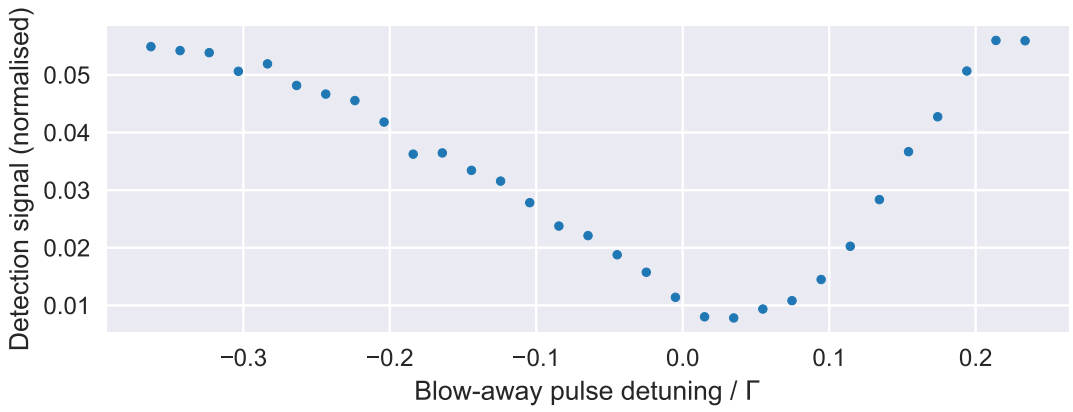


Figure 5.13: Detection signal following a 50 μs blow-away pulse, of intensity $\sim$2.5 I_{sat}. The signal is normalised against the photodiode signal during the 3D blue MOT.

Precise knowledge of the pulse lengths is also required such that the atom optics pulses execute their intended operation exactly. That is, a π-pulse should maximally invert the population of the states, while a $\pi/2$-pulse should split the wave function equally. One method of locating the atomic resonance involves iterative execution of Rabi and spectrum scans, the definitions of which are provided subsequently. The Rabi scan also yields the $\pi/2$ and π-pulse durations.

A Rabi scan is performed by applying a pulse of light with a constant frequency and intensity but of varying duration. Providing that the atoms start in the ground state, one can map out an oscillation of the form given in equation 2.10 by measuring the population of atoms excited by the pulse. The prefactor in this equation, $\Omega^2/(\Omega^2 + \Delta^2)$, is maximal when detuning $\Delta = 0$. In principle, one could perform Rabi scans and vary the laser frequency to maximise oscillation amplitude and locate resonance. Because the π-time and laser frequency are coupled, it is preferable to choose a pulse duration that situates you on the positive slope of the oscillation and vary the laser frequency to maximise excited state occupation.

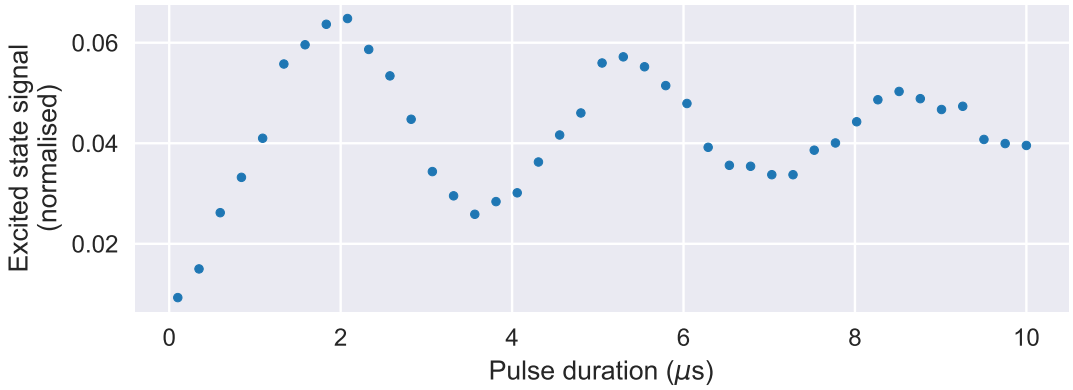


Figure 5.14: Rabi scan of the excited state population as a function of pulse duration. The signal is normalised against the photodiode signal during the 3D blue MOT.

This process is referred to in this context as a spectrum scan.

To carry out the first Rabi scan, the Rabi frequency and π-time are initially estimated from equation 4.1. For a 7.5 mm waist beam of 50 mW power, the Rabi frequency at the centre of the beam and corresponding π-time are approximately 0.7 MHz and 1.5 μs, respectively. The frequency of the red MOT serves as a starting point for performing the first Rabi scan. Said scan varies the pulse duration over several π-times, 0-10 μs in this case, in order to extract the π-time at the given frequency. Then, by performing a spectrum scan for a pulse length of half this duration, one can make a more refined estimate of the resonant frequency. By iterating between the two scans, the resonant frequency and π-time can be established. An example Rabi scan is shown in figure 5.14. The decaying amplitude of the oscillation is largely due to spontaneous emission and, to a lesser extent, from dephasing.

Whilst it would be straightforward to allocate more power to the Rabi scan and employ shorter pulses, this isn't necessarily desirable. Since the Fourier-limited

linewidth of a light pulse is inversely proportional to its duration, it is more instructive to select a longer pulse duration. A narrower linewidth facilitates better resolution of spectral features. In the case of the $^1S_0 - {}^3P_1$ transition, this comes with the caveat that the pulse duration should not be so long that spontaneous emission limits the contrast. In this experiment, the light for Rabi scans is delivered using a separate path to the atom interferometry light. This is because the two atom interferometry paths employ single-pass AOMs, as detailed in section 4.2.1, and so cannot dynamically adjust frequency. The Rabi scan light is delivered through one of the large DN100CF windows.

Here, contrast is predominantly limited by how detection is currently performed. To detect the excited state, a blow-away pulse is applied to remove atoms that were in the ground state, followed by a detection pulse after some delay. The fluorescence signal from the detection pulse is captured using the detection photodiode. Since this method only allows direct measurement of the excited state, a rudimentary normalisation is performed by dividing the excited state signal by the photodiode signal taken during the blue MOT. This normalisation doesn't account for fluctuations in the red MOT atom number. An improved method for normalisation should be possible by recording the photodiode signal during the blow-away pulse. The blow-away pulse uses the MOT beams at a blue detuning of 7 MHz. Since the MOT beams are nominally balanced, a relatively long pulse duration of 10 μs is required to dissipate a significant fraction of the ground state atoms. Transitioning to the detection scheme using an unbalanced blow-away beam, detailed in section 3.5.2, should facilitate shorter blow-away pulses, resulting in improved contrast.

5.4 Atom interferometry

Having validated the state detection and established the $\pi/2$ and π-pulse durations, it is now possible to construct the atom interferometry sequence.

5.4.1 Initial atom interferometry

The system presented in this thesis is designed to perform atom interferometry in the vertical axis, aligned to gravity. Initial proof of principle measurements are however made using light delivered in the horizontal plane in the same way as for the Rabi scan described in section 5.3.1. Just one k-vector of light is required in the standard three-pulse sequence, a fortuitous feature of single-photon transitions compared to two-photon transitions. This greatly simplifies initial AI efforts since there are no issues arising from degeneracy between, or alignment of, counter-propagating beams.

Each shot of the Mach-Zehnder style AI sequence on the ${}^1S_0 - {}^3P_1$ transition proceeds as follows. Following the red MOT, the atoms are allowed to fall for 1 ms, approximately 50 times the excited state lifetime, such that all the atoms are in the ground state. Resonant $\pi/2 - \pi - \pi/2$ -pulses are applied, separated by some fixed dark time, or time between pulses. The pulses couple the $|{}^1S_0,\ p\rangle$ and $|{}^3P_1,\ p + \hbar k\rangle$ states. Following the pulse sequence, less than 1 μs after the final $\pi/2$ beam splitter, a blow-away pulse is applied. This removes the ground state atoms, allowing detection of the excited state atoms only.

An example fringe is shown in figure 5.15. The π-time and dark time are both 2 μs and to scan out the fringe, the relative phase of the final $\pi/2$-pulse is varied for each shot. This is done by using ARTIQ to update the phase of the RF

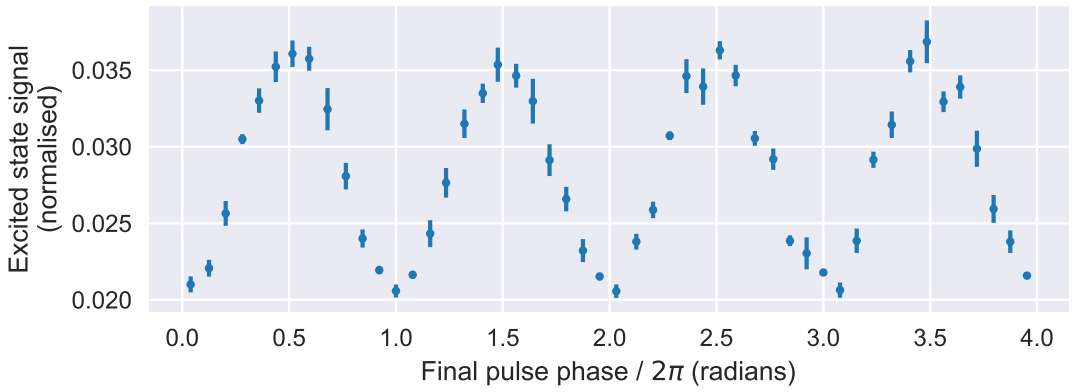


Figure 5.15: Atom interferometer fringe using the standard $\pi/2-\pi-\pi/2$ sequence. The π-time is 2 μs and the dark time is also 2 μs. The fringe is scanned out by varying the phase of the final $\pi/2$-pulse. The signal is normalised against the photodiode signal during the 3D blue MOT.

driving the pulse-shaping AOM, between the middle and final pulse. Blow-away and detection are performed in the same way as for the Rabi and spectrum scans described in section 5.3.1. Since normalisation for this fringe is performed between the excited state signal and blue MOT signal, it is not possible to determine the fringe contrast. The noise is likely dominated by shot-to-shot variation in red MOT atom number. Theoretically, the atom interferometer in this configuration is sensitive to accelerations along the interrogation axis. However, sensitivity is very poor due to the short T-times.

5.5 Summary

In this thesis, the primary focus is on building the test bed experiment to improve sensitivity limits in atom interferometry through high-fidelity large momentum transfer. This work directly contributes to Birmingham's role within the AION

collaboration. The results presented in this chapter effectively showcase the successful realisation of these aims.

Cold atoms samples of 8×10^6 atoms with waist 2.1 mm at a temperature of 30 μK are realised through two-stage cooling. Through continued optimisation, it should be possible to produce samples of $\sim$200 μm horizontal waist at $\sim$1 μK [54, 56, 125]. Progress in atom interferometry has been made despite larger-than-ideal cloud waists and temperatures. State detection is verified, and then atom optics pulses are implemented, coupling the $^1S_0 - {}^3P_1$ transition. Ultimately, atom interferometry fringes are presented.

Initial atom interferometry demonstrations are achieved with light in one direction from the Rabi scan path of the laser. To perform single-photon large momentum transfer requires counterpropagating light. The laser system and associated delivery optics described in chapter 4 will deliver the required counterpropagating pulses. This laser system and the associated delivery optics are now installed, and the first LMT results will be possible in the near term. The detection scheme described in section 3.5.2 is also built and ready to be implemented. One of the biggest contrast limitations in the initial atom interferometry results arises from the temporary detection scheme employed. The upgraded scheme should markedly improve the contrast.

With sample generation and atom interferometry demonstrated, the Birmingham strontium sidearm is established, and the described upgrades will further improve performance. The system is ready to perform large momentum transfer atom interferometry and deliver on the project aims of developing new schemes for pushing the state-of-the-art in sensitivity.

Chapter 6

Conclusion

Proposed long-baseline atom interferometry experiments have the potential to probe uncharted parameter space in fundamental physics searches. The single-photon 'clock' transitions in alkaline-earth atoms have catalysed the development of a new generation of atom interferometers. These transitions offer a solution to the long-standing challenge of technical laser phase noise that arises with two-photon transitions over extended baselines. Meeting the sensitivity targets of proposed experiments will require beyond state-of-the-art sensitivities, and one of the more scalable approaches is the technique of large momentum transfer. The current published record in single-photon large momentum transfer separation is 441 $\hbar k$ [57]. One of the aims of the AION collaboration is to investigate and push the limits of what is possible in the context of LMT, targetting momentum separations of 10^4 $\hbar$k in later phases. Reaching such demanding goals will require novel techniques and sustained research efforts. This thesis presents the design and implementation of a strontium atom interferometry experiment, laying the groundwork for developing such techniques.

In this work, a strontium cold atoms experiment is taken from its conception to the generation of atomic samples, and then the first demonstrations of atom interferometry fringes. An ultra-high vacuum apparatus is designed with geometric consideration for achieving record-beating spatial and momentum separations. The laser system comprising five lasers at four wavelengths for two-stage cooling and trapping of strontium is designed and implemented. Both systems are integrated, and a 2D MOT loads a blue 3D MOT of 2×10^7 atoms. The 689 nm laser for addressing the intercombination transition in strontium is characterised as having a linewidth better than 100 Hz. The performance is further validated in the generation of red MOT samples of 8×10^6 atoms at a temperature of 30 μK. Through optimisation, the temperature should be improved to achieve 1 μK samples, but the relatively high temperature has not prevented progress in demonstrating atom interferometry. A $\pi/2-\pi-\pi/2$-pulse sequence Mach-Zehnder configuration atom interferometer with strontium is demonstrated - a UK first. To enable large momentum transfer, a laser system for shaping 30 ns pulses at 30 MHz repetition rate is realised. Given sufficient laser power and fidelity, achieving momentum separations of 1,000 $\hbar$k in the near term is a realistic goal. Having demonstrated atom interferometry, work is currently underway towards the first realisation of large momentum transfer with the system. The experiment is well-poised to develop techniques for high-sensitivity, high-contrast LMT sequences. Further, the experiment will serve as a platform for developing techniques in single-photon atom interferometry on both the intercombination line and clock transition. The cooling laser system is designed for operation with the fermionic isotope ^{87}Sr, offering the clock transition and evaporative cooling to quantum degeneracy.

As strontium atom interferometry is in its infancy, there are a plethora of di-

rections in which research can lead. The single-photon transitions offer potential for interesting and novel schemes, such as polychromatic pulses [72] and hybrid schemes, using both the clock and intercombination transitions in strontium. As the apparatus is already designed to prepare ^{87}Sr, progressing to work with the clock transition should be straightforward. The experiment will also enable development of techniques to compensate for wavefront aberrations, one of the main sources of systematic phase shifts in large momentum transfer atom interferometry. Indeed, novel techniques will be necessary to achieve the LMT and sensitivity targets of the AION project. To meet the overall physics goals of the project will require continued research efforts over many years, and facility-scale experiments.

The progress presented in this thesis paves the way towards future fundamental physics searches based on large momentum transfer atom interferometry. Techniques and expertise developed here will be deployed to benefit the AION collaboration in current and future phases. AION stands to open a new window into gravitational wave astronomy in the mid-band, complementing LISA, LIGO and VIRGO. It will also probe dark matter, as well as physics beyond the standard model [25]. Furthermore, the experiment constructed in this research will act as a foundation for developing strategies to enhance fidelity, contrast, and sensitivity. These improvements are poised to influence cutting-edge atom interferometry experiments on a broader scale. Beyond the realm of fundamental physics, these advancements promise significant potential for real-world applications in quantum technology.

Acknowledgements

I couldn't possibly acknowledge all the people who have in some way contributed to this thesis and to making the strontiferometry dream a reality. As my friend Jacob Hines joked during his viva presentation: "Science does not happen in a vacuum.", indeed this work has benefitted from the combined input of many over the past few years. To everyone who helped proofread or otherwise gave feedback and advice regarding this thesis, you know who you are, thank you.

A special thank you to my supervision team. Mike, for encouraging me along this path, for the help and support throughout, and for having an anecdote or cautionary tale for any given situation, thanks. It was only towards the end of my undergraduate studies that I began to consider pursuing a PhD but, in hindsight, it was the best decision I could have made. This is in no small part a testament to the culture which you have fostered within the group at Birmingham. Mehdi, thank you for the mentorship and wisdom, and for always providing a healthy dose of perspective. Even after your move to LA, your support never wavered. Samuel, your insights during the latter part of my PhD were crucial and much appreciated.

Ben and Ollie, you brought energy and camaraderie to the lab. Special appreciation to Ollie for countless late nights in the pursuit of results. Thank you also to Soumyodeep, who despite having only recently joined the team has already

made a great impact. I also want to express my gratitude to the entire group, particularly Carlos and my PhD peers Ben and David.

Many thanks to Jason Hogan and the group at Stanford for hosting me, and to Fang for helping to arrange my secondment. It was a privilege to work with such a talented group of scientists during the first half a year of my PhD. I am grateful to all the friends I made inside and outside of the group, who made my time in California so enjoyable.

A big thank you to Jan, Rustin and Ben, whom by working alongside in the lab, I learned the most during my PhD. Jan for teaching me to couple my first fibre and introducing me to the world of great coffee. Rustin, for being a patient teacher, even after the fourth daily double espresso. And Ben, for all the practical lab skills and for introducing me to the ways of Bengineering. To Kieran McGovern, thank you for being a great lab partner for three years pre-PhD, your sense of humour and taste in music helped me through many a late night spent report writing. I hope this makes up for forgetting to acknowledge you in my masters report.

To all my friends throughout these four years, your presence offered a much-needed respite from the labours of research. Be it climbing, surfing, cycling, or simply unwinding, your company was my anchor.

Lastly, to my family - Mum, Dad, Oliver and the rest of my family, I thank you for your unwavering support and for always encouraging me to follow my interests. I couldn't have done it without you.

Bibliography

[1] P. R. Berman. *Atom interferometry*. Academic press, 1997.

[2] M. Kasevich and S. Chu. Atomic interferometry using stimulated Raman transitions. *Physical Review Letters*, 67(2):181, 1991.

[3] O. Carnal and J. Mlynek. Young's double-slit experiment with atoms: A simple atom interferometer. *Physical Review Letters*, 66(21):2689, 1991.

[4] D. W. Keith, C. R. Ekstrom, Q. A. Turchette, and D. E. Pritchard. An interferometer for atoms. *Physical Review Letters*, 66(21):2693, 1991.

[5] E. M. Rasel, M. K. Oberthaler, H. Batelaan, J. Schmiedmayer, and A. Zeilinger. Atom wave interferometry with diffraction gratings of light. *Physical Review Letters*, 75(14):2633, 1995.

[6] J. Hogan, D. Johnson, and M. Kasevich. Light-pulse atom interferometry. In *Atom Optics and Space Physics*, pages 411–447. IOS Press, 2009.

[7] T. Gustavson, P. Bouyer, and M. Kasevich. Precision rotation measurements with an atom interferometer gyroscope. *Physical Review Letters*, 78(11): 2046, 1997.

[8] B. Canuel, F. Leduc, D. Holleville, A. Gauguet, J. Fils, A. Virdis, A. Clairon, N. Dimarcq, C. J. Bordé, A. Landragin, et al. Six-axis inertial sensor using cold-atom interferometry. *Physical Review Letters*, 97(1):010402, 2006.

[9] M. Kasevich and S. Chu. Measurement of the gravitational acceleration of an atom with a light-pulse atom interferometer. *Applied Physics B*, 54(5): 321–332, 1992.

[10] G. Rosi, F. Sorrentino, L. Cacciapuoti, M. Prevedelli, and G. Tino. Precision measurement of the Newtonian gravitational constant using cold atoms. *Nature*, 510(7506):518–521, 2014.

[11] R. H. Parker, C. Yu, W. Zhong, B. Estey, and H. Müller. Measurement of the fine-structure constant as a test of the Standard Model. *Science*, 360 (6385):191–195, 2018.

[12] P. Asenbaum, C. Overstreet, M. Kim, J. Curti, and M. A. Kasevich. Atom-interferometric test of the equivalence principle at the 10^{-12} level. *Physical Review Letters*, 125(19):191101, 2020.

[13] C. Overstreet, P. Asenbaum, J. Curti, M. Kim, and M. A. Kasevich. Observation of a gravitational Aharonov-Bohm effect. *Science*, 375(6577):226–229, 2022.

[14] Y. Bidel, N. Zahzam, C. Blanchard, A. Bonnin, M. Cadoret, A. Bresson, D. Rouxel, and M. Lequentrec-Lalancette. Absolute marine gravimetry with matter-wave interferometry. *Nature Communications*, 9(1):1–9, 2018.

[15] R. Geiger, V. Ménoret, G. Stern, N. Zahzam, P. Cheinet, B. Battelier, A. Villing, F. Moron, M. Lours, Y. Bidel, et al. Detecting inertial effects with airborne matter-wave interferometry. *Nature Communications*, 2(1): 1–7, 2011.

[16] Y. Bidel, N. Zahzam, A. Bresson, C. Blanchard, M. Cadoret, A. V. Olesen, and R. Forsberg. Absolute airborne gravimetry with a cold atom sensor. *Journal of Geodesy*, 94(2):20, 2020.

[17] B. Stray, A. Lamb, A. Kaushik, J. Vovrosh, A. Rodgers, J. Winch, F. Hayati, D. Boddice, A. Stabrawa, A. Niggebaum, et al. Quantum sensing for gravity cartography. *Nature*, 602(7898):590–594, 2022.

[18] L. Antoni-Micollier, D. Carbone, V. Ménoret, J. Lautier-Gaud, T. King, F. Greco, A. Messina, D. Contrafatto, and B. Desruelle. Detecting volcano-related underground mass changes with a quantum gravimeter. *Earth and Space Science Open Archive*, 2022.

[19] K. Bongs, M. Holynski, J. Vovrosh, P. Bouyer, G. Condon, E. Rasel, C. Schubert, W. P. Schleich, and A. Roura. Taking atom interferometric quantum sensors from the laboratory to real-world applications. *Nature Reviews Physics*, 1(12):731–739, 2019.

[20] J. Vovrosh, A. Dragomir, B. Stray, and D. Boddice. Advances in Portable Atom Interferometry-Based Gravity Sensing. *Sensors*, 23(17):7651, 2023.

[21] V. Ménoret, P. Vermeulen, N. Le Moigne, S. Bonvalot, P. Bouyer, A. Landragin, and B. Desruelle. Gravity measurements below 10^{-9} g with a transportable absolute quantum gravimeter. *Scientific Reports*, 8(1):1–11, 2018.

[22] B. P. Abbott, R. Abbott, T. Abbott, M. Abernathy, F. Acernese, K. Ackley, C. Adams, T. Adams, P. Addesso, R. Adhikari, et al. Observation of gravitational waves from a binary black hole merger. *Physical Review Letters*, 116(6):061102, 2016.

[23] G. M. Tino and F. Vetrano. Is it possible to detect gravitational waves with atom interferometers? *Classical and Quantum Gravity*, 24(9):2167, 2007.

[24] S. Dimopoulos, P. W. Graham, J. M. Hogan, M. A. Kasevich, and S. Rajendran. Atomic gravitational wave interferometric sensor. *Physical Review D*, 78(12):122002, 2008.

[25] L. Badurina, E. Bentine, D. Blas, K. Bongs, D. Bortoletto, T. Bowcock, K. Bridges, W. Bowden, O. Buchmueller, C. Burrage, et al. AION: an atom interferometer observatory and network. *Journal of Cosmology and Astroparticle Physics*, 2020(05):011, 2020.

[26] M. Abe, P. Adamson, M. Borcean, D. Bortoletto, K. Bridges, S. P. Carman, S. Chattopadhyay, J. Coleman, N. M. Curfman, K. DeRose, et al. Matter-wave atomic gradiometer interferometric sensor (MAGIS-100). *Quantum Science and Technology*, 6(4):044003, 2021.

[27] B. Canuel, A. Bertoldi, L. Amand, E. Pozzo di Borgo, T. Chantrait, C. Danquigny, M. Dovale Álvarez, B. Fang, A. Freise, R. Geiger, et al. Exploring gravity with the MIGA large scale atom interferometer. *Scientific Reports*, 8(1):1–23, 2018.

[28] M.-S. Zhan, J. Wang, W.-T. Ni, D.-F. Gao, G. Wang, L.-X. He, R.-B. Li, L. Zhou, X. Chen, J.-Q. Zhong, et al. ZAIGA: Zhaoshan long-baseline atom interferometer gravitation antenna. *International Journal of Modern Physics D*, 29(04):1940005, 2020.

[29] T. Kovachy, P. Asenbaum, C. Overstreet, C. Donnelly, S. Dickerson, A. Sugarbaker, J. Hogan, and M. Kasevich. Quantum superposition at the half-metre scale. *Nature*, 528(7583):530–533, 2015.

[30] D. Schlippert, C. Meiners, R. Rengelink, C. Schubert, D. Tell, É. Wodey, K. Zipfel, W. Ertmer, and E. Rasel. Matter-wave interferometry for inertial sensing and tests of fundamental physics. In *CPT and Lorentz symmetry: proceedings of the eighth meeting on CPT and Lorentz symmetry*, pages 37–40. World Scientific, 2020.

[31] S. Herrmann, H. Dittus, C. Lämmerzahl, et al. Testing the equivalence principle with atomic interferometry. *Classical and Quantum Gravity*, 29 (18):184003, 2012.

[32] V. Schkolnik, O. Hellmig, A. Wenzlawski, J. Grosse, A. Kohfeldt, K. Döringshoff, A. Wicht, P. Windpassinger, K. Sengstock, C. Braxmaier, et al. A compact and robust diode laser system for atom interferometry on a sounding rocket. *Applied Physics B*, 122(8):1–8, 2016.

[33] V. Xu, M. Jaffe, C. D. Panda, S. L. Kristensen, L. W. Clark, and H. Müller. Probing gravity by holding atoms for 20 seconds. *Science*, 366(6466):745–749, 2019.

[34] C. Panda, M. Tao, J. Eggelhof, M. Ceja, A. Reynoso, V. Xu, and H. Müller. Probing Gravity for one Minute with an Optical-Lattice Atom Interferometer. *arXiv preprint arXiv:2301.13315*, 2023.

[35] A. Steane, M. Chowdhury, and C. Foot. Radiation force in the magneto-optical trap. *JOSA B*, 9(12):2142–2158, 1992.

[36] D. J. Wineland, J. J. Bollinger, W. M. Itano, F. Moore, and D. J. Heinzen. Spin squeezing and reduced quantum noise in spectroscopy. *Physical Review A*, 46(11):R6797, 1992.

[37] M. Kitagawa and M. Ueda. Squeezed spin states. *Physical Review A*, 47(6): 5138, 1993.

[38] K. C. Cox, G. P. Greve, B. Wu, and J. K. Thompson. Spatially homogeneous entanglement for matter-wave interferometry created with time-averaged measurements. *Physical Review A*, 94(6):061601, 2016.

[39] L. Salvi, N. Poli, V. Vuletić, and G. M. Tino. Squeezing on momentum states for atom interferometry. *Physical Review Letters*, 120(3):033601, 2018.

[40] A. Shankar, L. Salvi, M. L. Chiofalo, N. Poli, and M. J. Holland. Squeezed state metrology with Bragg interferometers operating in a cavity. *Quantum Science and Technology*, 4(4):045010, 2019.

[41] F. Anders, A. Idel, P. Feldmann, D. Bondarenko, S. Loriani, K. Lange, J. Peise, M. Gersemann, B. Meyer-Hoppe, S. Abend, et al. Momentum entanglement for atom interferometry. *Physical Review Letters*, 127(14): 140402, 2021.

[42] G. P. Greve, C. Luo, B. Wu, and J. K. Thompson. Entanglement-enhanced matter-wave interferometry in a high-finesse cavity. *Nature*, 610(7932):472–477, 2022.

[43] D. M. Giltner, R. W. McGowan, and S. A. Lee. Atom interferometer based on Bragg scattering from standing light waves. *Physical Review Letters*, 75 (14):2638, 1995.

[44] S.-w. Chiow, T. Kovachy, H.-C. Chien, and M. A. Kasevich. 102 $\hbar k$ large area atom interferometers. *Physical Review Letters*, 107(13):130403, 2011.

[45] B. Plotkin-Swing, D. Gochnauer, K. E. McAlpine, E. S. Cooper, A. O. Jamison, and S. Gupta. Three-path atom interferometry with large momentum separation. *Physical Review Letters*, 121(13):133201, 2018.

[46] A. Béguin, T. Rodzinka, L. Calmels, B. Allard, and A. Gauguet. Atom interferometry with coherent enhancement of Bragg pulse sequences. *Physical Review Letters*, 131(14):143401, 2023.

[47] S. S. Szigeti, J. E. Debs, J. J. Hope, N. P. Robins, and J. D. Close. Why momentum width matters for atom interferometry with Bragg pulses. *New Journal of Physics*, 14(2):023009, 2012.

[48] P. Cladé, S. Guellati-Khélifa, F. Nez, and F. Biraben. Large momentum beam splitter using Bloch oscillations. *Physical Review Letters*, 102(24): 240402, 2009.

[49] H. Müller, S.-w. Chiow, S. Herrmann, and S. Chu. Atom interferometers with scalable enclosed area. *Physical Review Letters*, 102(24):240403, 2009.

[50] G. D. McDonald, C. C. Kuhn, S. Bennetts, J. E. Debs, K. S. Hardman, M. Johnsson, J. D. Close, and N. P. Robins. 80 $\hbar k$ momentum separation with Bloch oscillations in an optically guided atom interferometer. *Physical Review A*, 88(5):053620, 2013.

[51] Z. Pagel, W. Zhong, R. H. Parker, C. T. Olund, N. Y. Yao, and H. Müller. Symmetric Bloch oscillations of matter waves. *Physical Review A*, 102(5): 053312, 2020.

[52] M. Gebbe, J.-N. Siemß, M. Gersemann, H. Müntinga, S. Herrmann, C. Lämmerzahl, H. Ahlers, N. Gaaloul, C. Schubert, K. Hammerer, et al. Twin-lattice atom interferometry. *Nature Communications*, 12(1):1–7, 2021.

[53] T. Rodzinka, E. Dionis, L. Calmels, S. Beldjoudi, A. Béguin, D. Guéry-Odelin, B. Allard, D. Sugny, and A. Gauguet. Optimal Floquet Engineering for Large Scale Atom Interferometers. *arXiv preprint arXiv:2403.14337*, 2024.

[54] L. Hu, N. Poli, L. Salvi, and G. M. Tino. Atom interferometry with the Sr optical clock transition. *Physical Review Letters*, 119(26):263601, 2017.

[55] L. Hu, E. Wang, L. Salvi, J. N. Tinsley, G. M. Tino, and N. Poli. Sr atom interferometry with the optical clock transition as a gravimeter and a gravity gradiometer. *Classical and Quantum Gravity*, 37(1):014001, 2019.

[56] J. Rudolph, T. Wilkason, M. Nantel, H. Swan, C. M. Holland, Y. Jiang, B. E. Garber, S. P. Carman, J. M. Hogan, et al. Large momentum transfer clock atom interferometry on the 689 nm intercombination line of strontium. *Physical Review Letters*, 124(8):083604, 2020.

[57] T. Wilkason, M. Nantel, J. Rudolph, Y. Jiang, B. E. Garber, H. Swan, S. P. Carman, M. Abe, J. M. Hogan, et al. Atom Interferometry with Floquet Atom Optics. *Physical Review Letters*, 129(18):183202, 2022.

[58] T. L. Nicholson, S. Campbell, R. Hutson, G. E. Marti, B. Bloom, R. L. McNally, W. Zhang, M. Barrett, M. S. Safronova, G. Strouse, et al. Systematic evaluation of an atomic clock at 2×10^{-18} total uncertainty. *Nature Communications*, 6(1):1–8, 2015.

[59] F. Riehle, P. Gill, F. Arias, and L. Robertsson. The CIPM list of recommended frequency standard values: guidelines and procedures. *Metrologia*, 55(2):188, 2018.

[60] T. Mazzoni, X. Zhang, R. Del Aguila, L. Salvi, N. Poli, and G. Tino. Large-momentum-transfer Bragg interferometer with strontium atoms. *Physical Review A*, 92(5):053619, 2015.

[61] X. Zhang, R. P. del Aguila, T. Mazzoni, N. Poli, and G. M. Tino. Trapped-atom interferometer with ultracold Sr atoms. *Physical Review A*, 94(4): 043608, 2016.

[62] R. P. del Aguila, T. Mazzoni, L. Hu, L. Salvi, G. M. Tino, and N. Poli. Bragg gravity-gradiometer using the $^1S_0 - {}^3P_1$ intercombination transition of 88Sr. *New Journal of Physics*, 20(4):043002, 2018.

[63] P. W. Graham, J. M. Hogan, M. A. Kasevich, and S. Rajendran. New method for gravitational wave detection with atomic sensors. *Physical Review Letters*, 110(17):171102, 2013.

[64] D. L. Butts, K. Kotru, J. M. Kinast, A. M. Radojevic, B. P. Timmons, and R. E. Stoner. Efficient broadband Raman pulses for large-area atom interferometry. *JOSA B*, 30(4):922–927, 2013.

[65] A. Dunning, R. Gregory, J. Bateman, N. Cooper, M. Himsworth, J. A. Jones, and T. Freegarde. Composite pulses for interferometry in a thermal cold atom cloud. *Physical Review A*, 90(3):033608, 2014.

[66] P. Berg, S. Abend, G. Tackmann, C. Schubert, E. Giese, W. P. Schleich, F. Narducci, W. Ertmer, and E. Rasel. Composite-light-pulse technique for high-precision atom interferometry. *Physical Review Letters*, 114(6):063002, 2015.

[67] J. C. Saywell, M. Carey, M. Belal, I. Kuprov, and T. Freegarde. Optimal control of Raman pulse sequences for atom interferometry. *Journal of Physics B: Atomic, Molecular and Optical Physics*, 2020.

[68] J. C. Saywell, M. S. Carey, P. S. Light, S. S. Szigeti, A. R. Milne, K. S. Gill, M. L. Goh, V. S. Perunicic, N. M. Wilson, C. D. Macrae, et al. Enhancing the sensitivity of atom-interferometric inertial sensors using robust control. *Nature Communications*, 14(1):7626, 2023.

[69] Z. Chen, G. Louie, Y. Wang, T. Deshpande, and T. Kovachy. Enhancing strontium clock atom interferometry using quantum optimal control. *Physical Review A*, 107(6):063302, 2023.

[70] V. Schkolnik, B. Leykauf, M. Hauth, C. Freier, and A. Peters. The effect of wavefront aberrations in atom interferometry. *Applied Physics B*, 120: 311–316, 2015.

[71] Q.-Q. Hu, C. Freier, B. Leykauf, V. Schkolnik, J. Yang, M. Krutzik, and A. Peters. Mapping the absolute magnetic field and evaluating the quadratic Zeeman-effect-induced systematic error in an atom interferometer gravimeter. *Physical Review A*, 96(3):033414, 2017.

[72] S. Lellouch, O. Ennis, R. Haditalab, M. Langlois, and M. Holynski. Polychromatic atom optics for atom interferometry. *EPJ Quantum Technology*, 10(1):1–16, 2023.

[73] M.-k. Zhou, Q. Luo, X.-c. Duan, Z.-k. Hu, et al. Observing the effect of wavefront aberrations in an atom interferometer by modulating the diameter of Raman beams. *Physical Review A*, 93(4):043610, 2016.

[74] A. Trimeche, M. Langlois, S. Merlet, and F. P. Dos Santos. Active control of laser wavefronts in atom interferometers. *Physical Review Applied*, 7(3): 034016, 2017.

[75] R. Karcher, A. Imanaliev, S. Merlet, and F. P. D. Santos. Improving the accuracy of atom interferometers with ultracold sources. *New Journal of Physics*, 20(11):113041, 2018.

[76] P. W. Graham, J. M. Hogan, M. A. Kasevich, and S. Rajendran. Resonant mode for gravitational wave detectors based on atom interferometry. *Physical Review D*, 94(10):104022, 2016.

[77] C. J. Foot. *Atomic physics*, volume 7. OUP Oxford, 2004.

[78] F. A. Narducci, A. T. Black, and J. H. Burke. Advances toward fieldable atom interferometers. *Advances in Physics: X*, 7(1):1946426, 2022.

[79] P. Storey and C. Cohen-Tannoudji. The Feynman path integral approach to atomic interferometry. A tutorial. *Journal de Physique II*, 4(11):1999–2027, 1994.

[80] A. Bertoldi, F. Minardi, and M. Prevedelli. Phase shift in atom interferometers: Corrections for nonquadratic potentials and finite-duration laser pulses. *Physical Review A*, 99(3):033619, 2019.

[81] W. M. Itano, J. C. Bergquist, J. J. Bollinger, J. Gilligan, D. Heinzen, F. Moore, M. Raizen, and D. J. Wineland. Quantum projection noise: Population fluctuations in two-level systems. *Physical Review A*, 47(5):3554, 1993.

[82] P. Cheinet. *Conception et réalisation d'un gravimètre à atomes froids*. PhD thesis, Université Pierre et Marie Curie-Paris VI, 2006.

[83] D. W. Sesko, T. Walker, and C. E. Wieman. Behavior of neutral atoms in a spontaneous force trap. *JOSA B*, 8(5):946–958, 1991.

[84] M. Chiarotti, J. N. Tinsley, S. Bandarupally, S. Manzoor, M. Sacco, L. Salvi, and N. Poli. Practical limits for large-momentum-transfer clock atom interferometers. *PRX Quantum*, 3(3):030348, 2022.

[85] J. M. Mcguirk, G. Foster, J. Fixler, M. Snadden, and M. Kasevich. Sensitive absolute-gravity gradiometry using atom interferometry. *Physical Review A*, 65(3):033608, 2002.

[86] J. Rudolph, W. Herr, C. Grzeschik, T. Sternke, A. Grote, M. Popp, D. Becker, H. Müntinga, H. Ahlers, A. Peters, et al. A high-flux BEC source for mobile atom interferometers. *New Journal of Physics*, 17(6):065001, 2015.

[87] T. Kovachy, J. M. Hogan, A. Sugarbaker, S. M. Dickerson, C. A. Donnelly, C. Overstreet, and M. A. Kasevich. Matter wave lensing to picokelvin temperatures. *Physical Review Letters*, 114(14):143004, 2015.

[88] H. J. Metcalf and P. van der Straten. *Laser Cooling and Trapping*. Springer-Verlag, 1999.

[89] J. M. Hogan and M. A. Kasevich. Atom-interferometric gravitational-wave detection using heterodyne laser links. *Physical Review A*, 94(3):033632, 2016.

[90] A. Arvanitaki, P. W. Graham, J. M. Hogan, S. Rajendran, and K. Van Tilburg. Search for light scalar dark matter with atomic gravitational wave detectors. *Physical Review D*, 97(7):075020, 2018.

[91] M. M. Boyd. *High precision spectroscopy of strontium in an optical lattice: Towards a new standard for frequency and time*. PhD thesis, University of Colorado at Boulder, 2007.

[92] A. D. Ludlow. *The strontium optical lattice clock: optical spectroscopy with sub-Hertz accuracy*. PhD thesis, University of Colorado at Boulder, 2008.

[93] S. Stellmer. *Degenerate quantum gases of strontium*. PhD thesis, University of Innsbruck, 2013.

[94] J. Sansonetti and G. Nave. Wavelengths, transition probabilities, and energy levels for the spectrum of neutral strontium (Sr I). *Journal of Physical and Chemical Reference Data*, 39(3):033103, 2010.

[95] J. A. Muniz, D. J. Young, J. R. Cline, and J. K. Thompson. Cavity-QED measurements of the Sr 87 millihertz optical clock transition and determination of its natural linewidth. *Physical Review Research*, 3(2):023152, 2021.

[96] A. V. Taichenachev, V. Yudin, C. Oates, C. Hoyt, Z. Barber, and L. Hollberg. Magnetic field-induced spectroscopy of forbidden optical transitions with application to lattice-based optical atomic clocks. *Physical Review Letters*, 96(8):083001, 2006.

[97] B. Lu, Y. Wang, J. Han, S. Zhang, J. Li, and H. Chang. Exploration of the magnetic-field-induced 5s5p $^3P_0 - 5s^2\ ^1S_0$ forbidden transition in bosonic Sr atom. *Journal of Physics Communications*, 1(5):055017, 2017.

[98] W. D. Phillips and H. Metcalf. Laser deceleration of an atomic beam. *Physical Review Letters*, 48(9):596, 1982.

[99] E. L. Raab, M. Prentiss, A. Cable, S. Chu, and D. E. Pritchard. Trapping of neutral sodium atoms with radiation pressure. *Physical Review Letters*, 59(23):2631, 1987.

[100] P. D. Lett, R. N. Watts, C. I. Westbrook, W. D. Phillips, P. L. Gould, and H. J. Metcalf. Observation of atoms laser cooled below the Doppler limit. *Physical Review Letters*, 61(2):169, 1988.

[101] I. Nosske, L. Couturier, F. Hu, C. Tan, C. Qiao, J. Blume, Y. Jiang, P. Chen, and M. Weidemüller. Two-dimensional magneto-optical trap as a source for cold strontium atoms. *Physical Review A*, 96(5):053415, 2017.

[102] J. L. Margrave and A. N. Nesmeianov. Vapor pressure of the chemical elements. *Journal of Chemical Education*, 41(8):A590, 1964.

[103] T. H. Loftus, T. Ido, M. M. Boyd, A. D. Ludlow, and J. Ye. Narrow line cooling and momentum-space crystals. *Physical Review A*, 70(6):063413, 2004.

[104] R. Grimm, M. Weidemüller, and Y. B. Ovchinnikov. Optical dipole traps for neutral atoms. In *Advances in atomic, molecular, and optical physics*, volume 42, pages 95–170. Elsevier, 2000.

[105] S. Stellmer, R. Grimm, and F. Schreck. Production of quantum-degenerate strontium gases. *Physical Review A*, 87(1):013611, 2013.

[106] D. A. Steck. Rubidium 87 D Line Data. 2021.

[107] B. Stray, O. Ennis, S. Hedges, S. Dey, M. Langlois, K. Bongs, S. Lellouch, M. Holynski, B. Bostwick, J. Chen, et al. Centralised Design and Production of the Ultra-High Vacuum and Laser-Stabilisation Systems for the AION Ultra-Cold Strontium Laboratories. *arXiv preprint arXiv:2305.20060*, 2023.

[108] D. Xu. *A new design of a compact strontium cold-atom source*. PhD thesis, University of Oxford, 2020.

[109] X. Chen, M. Zeuner, U. Schneider, C. Foot, T. Harte, and E. Bentine. AtomECS: Simulate laser cooling and magneto-optical traps. *arXiv preprint arXiv:2105.06447*, 2021.

[110] C. Feng, P. Robert, P. Bouyer, B. Canuel, J. Li, S. Das, C. Kwong, D. Wilkowski, M. Prevedelli, and A. Bertoldi. High flux strontium atom source. *Quantum Science and Technology*, 9(2):025017, 2024.

[111] R. Roy, A. Green, R. Bowler, and S. Gupta. Rapid cooling to quantum degeneracy in dynamically shaped atom traps. *Physical Review A*, 93(4): 043403, 2016.

[112] B. J. DeSalvo, M. Yan, P. G. Mickelson, Y. M. De Escobar, and T. C. Killian. Degenerate fermi gas of sr 87. *Physical Review Letters*, 105(3):030402, 2010.

[113] M. Ortner and L. G. C. Bandeira. Magpylib: A free Python package for magnetic field computation. *SoftwareX*, 11:100466, 2020.

[114] T. P. Dinneen, K. R. Vogel, E. Arimondo, J. L. Hall, and A. Gallagher. Cold collisions of Sr*- Sr in a magneto-optical trap. *Physical Review A*, 59 (2):1216, 1999.

[115] N. Poli, R. Drullinger, G. Ferrari, J. Léonard, F. Sorrentino, and G. Tino. Cooling and trapping of ultracold strontium isotopic mixtures. *Physical Review A*, 71(6):061403, 2005.

[116] S. Zhang, P. Ramchurn, M. Menchetti, Q. Ubaid, J. Jones, K. Bongs, and Y. Singh. Novel repumping on $^3P_0 - {}^3D_1$ for Sr magneto-optical trap and Lande g factor measurement of $^3D_1$. *Journal of Physics B: Atomic, Molecular and Optical Physics*, 53(23):235301, 2020.

[117] L. Ye, L. Yi-Ge, Z. Yang, W. Qiang, W. Shao-Kai, Y. Tao, C. Jian-Ping, L. Tian-Chu, F. Zhan-Jun, and Z. Er-Jun. Stable narrow linewidth 689 nm diode laser for the second stage cooling and trapping of strontium atoms. *Chinese Physics Letters*, 27(7):074208, 2010.

[118] E. D. Black. An introduction to Pound–Drever–Hall laser frequency stabilization. *American Journal of Physics*, 69(1):79–87, 2001.

[119] J. A. Boyd and T. Lahaye. A basic introduction to ultrastable optical cavities for laser stabilization. *arXiv preprint arXiv:2308.08015*, 2023.

[120] S. Webster, M. Oxborrow, and P. Gill. Vibration insensitive optical cavity. *Physical review A*, 75(1):011801, 2007.

[121] E. Rocco, R. Palmer, T. Valenzuela, V. Boyer, A. Freise, and K. Bongs. Fluorescence detection at the atom shot noise limit for atom interferometry. *New Journal of Physics*, 16(9):093046, 2014.

[122] A. Sugarbaker, S. M. Dickerson, J. M. Hogan, D. M. Johnson, and M. A. Kasevich. Enhanced atom interferometer readout through the application of phase shear. *Physical Review Letters*, 111(11):113002, 2013.

[123] D. S. Weiss, E. Riis, Y. Shevy, P. J. Ungar, and S. Chu. Optical molasses and multilevel atoms: experiment. *JOSA B*, 6(11):2072–2083, 1989.

[124] T. M. Brzozowski, M. Maczynska, M. Zawada, J. Zachorowski, and W. Gawlik. Time-of-flight measurement of the temperature of cold atoms for short trap-probe beam distances. *Journal of Optics B: Quantum and Semiclassical Optics*, 4(1):62, 2002.

[125] S. Snigirev, A. J. Park, A. Heinz, I. Bloch, and S. Blatt. Fast and dense magneto-optical traps for strontium. *Physical Review A*, 99(6):063421, 2019.

[126] A. E. Siegman. *Lasers*. University science books, 1986.

[127] G. Stern, B. Battelier, R. Geiger, G. Varoquaux, A. Villing, F. Moron, O. Carraz, N. Zahzam, Y. Bidel, W. Chaibi, et al. Light-pulse atom interferometry in microgravity. *The European Physical Journal D*, 53:353–357, 2009.

[128] D. L. Butts, J. M. Kinast, B. P. Timmons, and R. E. Stoner. Light pulse atom interferometry at short interrogation times. *JOSA B*, 28(3):416–421, 2011.

[129] J. Fleck Jr. Ultrashort-pulse generation by Q-switched lasers. *Physical Review B*, 1(1):84, 1970.

[130] A. Killi, J. Dörring, U. Morgner, M. J. Lederer, J. Frei, and D. Kopf. High speed electro-optical cavity dumping of mode-locked laser oscillators. *Optics Express*, 13(6):1916–1922, 2005.

[131] J. Vengelis, G. Sinkevičius, J. Banys, L. Masiulis, R. Grigonis, J. Domarkas, and V. Sirutkaitis. Investigation of piezoelectric ringing effects in Pockels cells based on beta barium borate crystals. *Applied Optics*, 58(33):9240–9250, 2019.

[132] C. Solaro, C. Debavelaere, P. Cladé, and S. Guellati-Khelifa. Atom interferometer driven by a picosecond frequency comb. *Physical Review Letters*, 129(17):173204, 2022.

[133] L. Stephenson, D. Nadlinger, B. Nichol, S. An, P. Drmota, T. Ballance, K. Thirumalai, J. Goodwin, D. Lucas, and C. Ballance. High-rate, high-fidelity entanglement of qubits across an elementary quantum network. *Physical Review Letters*, 124(11):110501, 2020.

[134] E. Hecht. *Optics*. Pearson Education, 2012.

[135] A. Jha, A. Singh, Y. Kale, J. Wayland, Y. Huyan, Q. Sun, J. Jones, M. Gellesch, K. Bongs, and Y. Singh. Towards the Development of an Optical Lattice Clock Testbed Setup for the iqClock Project. In *2023 Conference on Lasers and Electro-Optics Europe & European Quantum Electronics Conference (CLEO/Europe-EQEC)*, pages 1–1. IEEE, 2023.

[136] R. Nourshargh, S. Lellouch, S. Hedges, M. Langlois, K. Bongs, and M. Holynski. Circulating pulse cavity enhancement as a method for extreme momentum transfer atom interferometry. *Communications Physics*, 4(1):257, 2021.

[137] R. Nourshargh, S. Hedges, M. Langlois, K. Bongs, and M. Holynski. Doppler compensation for cavity-based atom interferometry. *Optics Express*, 30(17): 30001–30011, 2022.

[138] R. Nourshargh. *Cavity enhanced atom interferometry*. PhD thesis, University of Birmingham, 2021.

[139] M. Dovale-Álvarez, D. D. Brown, A. W. Jones, C. M. Mow-Lowry, H. Miao, and A. Freise. Fundamental limitations of cavity-assisted atom interferometry. *Physical Review A*, 96(5):053820, 2017.

[140] A. Bertoldi, C.-H. Feng, D. Naik, B. Canuel, P. Bouyer, and M. Prevedelli. Fast control of atom-light interaction in a narrow linewidth cavity. *Physical Review Letters*, 127(1):013202, 2021.

[141] J. Höschele, S. Buob, A. Rubio-Abadal, V. Makhalov, and L. Tarruell. Atom-number enhancement by shielding atoms from losses in strontium magneto-optical traps. *Physical Review Applied*, 19(6):064011, 2023.

[142] X. Xu, T. H. Loftus, J. L. Hall, A. Gallagher, and J. Ye. Cooling and trapping of atomic strontium. *JOSA B*, 20(5):968–976, 2003.

[143] S. B. Nagel, C. Simien, S. Laha, P. Gupta, V. Ashoka, and T. Killian. Magnetic trapping of metastable $^3P_2$ atomic strontium. *Physical Review A*, 67(1):011401, 2003.

[144] R. Takeuchi, H. Chiba, S. Okaba, M. Takamoto, S. Tsuji, and H. Katori. Continuous outcoupling of ultracold strontium atoms combining three different traps. *Applied Physics Express*, 16(4):042003, 2023.

[145] S. Stellmer and F. Schreck. Reservoir spectroscopy of 5s5p $^3P_2$ - 5snd $^3D_{1,2,3}$ transitions in strontium. *Physical Review A*, 90(2):022512, 2014.

Acronyms

ADC analog-to-digital converter.

AOM acousto-optic modulator.

BBO barium borate.

CMOS complementary metal oxide semiconductor.

DAC digital-to-analog converter.

DDS direct digital synthesiser.

ECDL external-cavity diode laser.

EMCCD electron-multiplying charge-coupled device.

EOM electro-optic modulator.

FPGA field-programmable gate array.

FPS frames per second.

GW gravitational wave.

ILA injection-locked amplifier.

LMT large momentum transfer.

LPAI light-pulse atom interferometry.

MOT magneto-optical trap.

MZ Mach-Zehnder.

PBS polarising beam splitter.

PDH Pound-Drever-Hall.

RF radio frequency.

TOF time-of-flight.

TTL transistor-transistor logic.

UHV ultra-high vacuum.

ULSDM ultra-light scalar dark matter.